

STUDY, SIMULATION, DESIGN AND MANUFACTURING OF ATTITUDE DETERMINATION AND CONTROL SYSTEM FOR MINI-SATELLITE SYSTEM IN LOW EARTH ORBIT

By
SOURADEEP HAZRA



**DEPARTMENT OF ASTRONOMY,
ASTROPHYSICS AND SPACE ENGINEERING
INDIAN INSTITUTE OF TECHNOLOGY
INDORE**

May, 2025

STUDY, SIMULATION, DESIGN AND MANUFACTURING OF ATTITUDE DETERMINATION AND CONTROL SYSTEM FOR MINI-SATELLITE SYSTEM IN LOW EARTH ORBIT

A THESIS

*Submitted in partial fulfilment of the
requirements for the award of the degree
of*
Master of Technology

by
SOURADEEP HAZRA



**DEPARTMENT OF ASTRONOMY,
ASTROPHYSICS AND SPACE ENGINEERING
INDIAN INSTITUTE OF TECHNOLOGY
INDORE**

May, 2025



INDIAN INSTITUTE OF TECHNOLOGY INDORE

CANDIDATE'S DECLARATION

I hereby certify that the work which is being presented in the thesis entitled **STUDY SIMULATION, DESIGN AND MANUFACTURING OF ATTITUDE DETERMINATION AND CONTROL SYSTEM FOR MINI-SATELLITE SYSTEM IN LOW EARTH ORBIT** in the partial fulfilment of the requirements for the award of the degree of **MASTER OF TECHNOLOGY** and submitted in the **DEPARTMENT OF ASTRONOMY, ASTROPHYSICS AND SPACE ENGINEERING, INDIAN INSTITUTE OF TECHNOLOGY**, is an authentic record of my own work carried out during the time period from July, 2023 to May, 2025 under the supervision of Prof. Abhirup Datta, Dean Research and Development, IIT Indore and Prof. Hari B Hablani, Professor, IIT Indore.

The matter presented in this thesis has not been submitted by me for the award of any other degree of this or any other institute.

Souradeep Hazra
16/05/2025

Signature of the student with date
SOURADEEP HAZRA

This is to certify that the above statement made by the candidate is correct to the best of my/our knowledge.

Abhirup Datta
15/5/25
Signature of the Supervisor
(with date)

Prof. Abhirup Datta

Hari Hablani
Signature of the Supervisor
(with date) May 15, 2025

Prof. Hari B Hablani

SOURADEEP HAZRA has successfully given his/her MTech. Oral Examination held on **7th June, 2025**.

Hari Hablani
Abhirup Datta
15/5/25
Signature(s) of Supervisor(s) of MTech. thesis
Date: May 15, 2025

Amresh
Signature of MTech Co-ordinator:
Date: 16-05-2025

Manoneta Chakraborty
Signature of Convener, DPGC
Date: 16/5/2025

S. Das
Signature of HoD, DAASE:
Date: 16/05/2025

ACKNOWLEDGEMENTS

I would like to express my heartfelt gratitude to all those who have supported and guided me throughout this project.

First and foremost, I am deeply thankful to all the professors for imparting their knowledge across various domains, which laid a strong foundation for this work. I extend my sincere thanks to the institute for providing a vibrant techno-academic platform along with excellent sports and music facilities that contributed to a well-rounded experience.

I am especially grateful to my project guides, Dr. Abhirup Datta and Dr. Hari Hablani, for granting me the opportunity to work on a topic that aligns with my interests and for their constant encouragement and insightful feedback throughout the journey.

Special thanks go to the workshop members, Mr. Pawan and Mr. Deepak, for their technical support and assistance during the machining processes.

I would also like to acknowledge the unwavering moral support of my lab-mates, whose presence made the long hours more bearable.

Lastly, I appreciate the efforts of Abhijeet Dutta and Harsha Tanti for their help in coordinating and managing the various arrangements of items that made this work possible.

This project would not have been successful without the support of all the aforementioned individuals, and I remain genuinely thankful.

~Souradeep Hazra

DEDICATION

*I dedicate this work to my beloved parents, whose
constant support and sacrifices have shaped my
journey;*

*To my mentors and teachers, whose guidance
illuminated the path of knowledge;*

*And to every individual who stood by me during the
challenges—your presence has made this journey
meaningful.*

*And most importantly, to all the students who are
ready to contribute to the betterment of humanity—
May your curiosity, dedication, and compassion
drive positive change in the world and make the
world a better place to live.*

Abstract

The objective of this thesis is to investigate the complete Study, simulation, design and fabricate of Attitude Determination and Control Systems (ADCS) in Earth-orbiting satellites specifically for the Low Earth Orbit(LEO). First part of the thesis focuses on the experimental determination of geomagnetic fields and methodologies, providing a solution to determine the orbit's magnetic field in reference to the subsatellite point of the earth giving a new dimension to the research. ADCS is critical for maintaining a satellite's orientation relative to reference points such as Earth, the Sun, or other celestial bodies, allowing critical operations such as high-resolution imaging, precise data collection, and stable communication links. The research highlights the importance of attitude control systems (ADCS) in modern space missions as well as the difficulties associated with achieving accuracy and reliability in attitude control.

Magnetometers, Helmholtz cages, and inertial measurement units (IMUs) are among the components and technologies examined in this study. The investigation focuses on counteracting external influences such as hard iron effects (permanent magnetic fields), soft iron effects (magnetic distortion from materials), and misalignment errors during data acquisition. The role that each element plays in detecting and analysing geomagnetic field parameters is also investigated. A number of controlled experiments were carried out with the assistance of sophisticated calibration methods and apparatuses that were designed to reduce the amount of interference from the outside world and carry out the research swiftly. The research included the utilization of a Helmholtz cage for the generation of a uniform magnetic field and the precise positioning of an IMU on a turntable along with the comparison of the practical and mathematical value.

The experimental results are compared to existing theoretical geomagnetic models, such as the World Magnetic Model (WMM) and the International Geomagnetic Reference Field (IGRF). Significant differences between the values that were measured and those that were theoretical were discovered,

which brought to light the requirement for error modelling that is robust. These findings contribute to a better understanding of the behaviour of ADCS sensors as well as the significance of compensatory mechanisms in order to improve the accuracy of geomagnetic field estimation.

The research also investigates the practical applications for ADCS for CubeSats, which are a growing advancement in satellites that are both cost-effective and compact. The research demonstrates that precise attitude control can be achieved despite the resource constraints that are inherent to smaller satellite platforms. This is accomplished through the integration of advanced algorithms and innovative sensor technologies. This is consistent with broader trends in satellite system miniaturization and an increasing demand for agile, cost-effective space mission solutions.

This thesis makes significant contributions to the field of ADCS by combining theoretical modelling and experimental verification. These contributions pave the way for advancements in satellite stability and orientation precision, which are both areas that are currently in need of improvement. In order to fulfil the requirements of increasingly complex space missions, such as those involving the observation of Earth and the exploration of deep space, these developments are essential.

The Complete design of the SHOURYA(Satellite **H**ardware **O**perational Unit for **R**ead-time **Y**ield and **A**nalysis) along with few testing phase is covered in the latter portion of the thesis. The 3-Axis system will be the future of satellite testing in the near future, and it is likely that an ADCS system of a cube sat will be implemented. The project's future goals include researching and developing the system's control component, which will advance the field of attitude dynamics research along with many more futuristic innovation and implementations.

Contents

TABLE OF FIGURE	x
LIST OF TABLE	xiv
ACRONYMS.....	xv
Chapter 1: Introduction.....	1
1.1 Background	1
1.2 Recent works.....	2
1.3. Role of the ADCS	3
1.4 Modes of operation of the ADCS	3
1.5 Ultimate Objectives.....	4
Chapter 2: Literature Review	6
2.1. Apparatus:	6
2.1.1. Helmholtz Cage:.....	6
2.1.2. Milli-Gauss Meter (GU-3001):	7
2.1.3. Tachometer (GU-3001):	8
2.1.4. IMU Sensor (HG1120):.....	9
2.1.5. Power Module (XL4016):	10
Chapter 3: Earth's Magnetism.....	11
3.1. Theory of Geomagnetism.....	11
3.2. Output Arguments:.....	15
3.3. Magnetic Models.....	16
3.3.1. World Magnetic Model (WMM).....	17
3.3.2. International Geomagnetic Reference Field (IGRF)	18
3.4. Magnetometer Error Models	18
3.4.1. Background:	18
Chapter 4: Experiments.....	22
4.1. Setup.....	22
4.2. Experiments	23
4.2.1. Experiment-1:	24
4.2.2. Experiment-2:	26
4.2.3.Experiment-3:	30
4.2.4 Experiment-4:	32
Chapter 5: Implementation	40
5.1 Basics	40
5 1.1. Orbital Parameter.....	40

5 1.2. Simulation work flow	41
Chapter 6: Gyro Rate Bias Estimation.....	48
Chapter 7: Basic Technical Integration	58
7.1. Basic Procedure:.....	58
7.2. CAD Design	59
7.3. Initial model testing in one Axis	60
7.4 Power System Circuit.....	61
7.5 Single Motor Testing:	62
7.6. Three Motor Testing Experiment :.....	65
Chapter 8: Design and Design Analysis of SHOURYA	67
8.1 SHOURYA's Design	67
8.2 Types of Air-Bearing	67
8.3 Designs	69
8.4 3D Design	71
8.5 Design Analysis	73
8.5.1 Structural Analysis	74
8.5.2 Acoustic analysis	77
8.5.3 Air flow analysis	80
Chapter 9: Air bearing with Process and integration	81
9.1 Working	81
9.2 Manufacturing Process.....	82
9.2.1 Electrical Integration	82
9.2.2 3D printing	83
9.2.3 Mechanical Manufacturing.....	84
9.2.4 Base Stand Design and Integration.....	86
9.3 Painting	87
9.4 Innovative Approach.....	87
9.5 Challenges	89
Chapter 10: Working Analysis.....	91
10.1 Complete Integration.....	91
10.2 Operational Guidelines and Control Setup	93
10.3 Working Analysis	94
10.3.1 IMU Showing changes in all the direction.....	94
10.3.2 Random Movement	96
10.3.3 Fast and Slow Manoeuvring.....	96
10.3.4 Limitations.....	98

Chapter 11: Conclusion and Future Scope 99

APPENDIX-A 102

APPENDIX-B 106

REFERENCES 109

TABLE OF FIGURE

Figure 1: Helmholtz Cage in the Laboratory	6
Figure 2: Schematic diagram of Helmholtz Cage	6
Figure 3: Tachometer	8
Figure 4: Milli-Gauss meter	8
Figure 5: Geodetic and Magnetic Pole	11
Figure 6: Components of earth's Magnetic Field.....	13
Figure 7: Geodetic and Magnetic pole Diagram	13
Figure 8: Magnetic field frame	14
Figure 9: 3D Notation of all the Arguments.....	15
Figure 10: Turntable with Connections	22
Figure 11: Position of IMU on the turntable (a) Front View (b) Isometric View (c) Top View.....	22
Figure 12: Plot of magnetic field in X-Axis over Time (a) Without Laptop (Left) (b) With Laptop (Right)	26
Figure 13: Plot of magnetic field in presence of laptop	26
Figure 14: Value Shown on the System Software.....	27
Figure 15: Plot of averaged out data collected from the magnetometer	28
Figure 16: Magnetic field after calibration after in X,Y,Z direction respectively.	29
Figure 17: Latitude and Longitude information of lab location from website (Left) and using mobile GPS (right)	31
Figure 18: Flowchart showing the steps taken for the experimentations.....	34
Figure 19: Plot of theoretical and experimental magnetic field value in X-Axis.....	35
Figure 20: Plot of theoretical and experimental magnetic field value in Y-Axis.....	36
Figure 21: Plot of theoretical and experimental magnetic field value in Z-Axis.....	37
Figure 22 : Plot of theoretical and experimental magnetic field value in all 3 -Axis	38
Figure 23: Error histograms	39
Figure 24: Six Orbital Parameter	40
Figure 25: Application Root Map with proper Steps	44
Figure 26: Input parameters of the Simulation	45
Figure 27: 3D Orbit that is generated from the data given Input parameter	45

Figure 28: Magnetic field form WMM model in X, Y and Z direction Vs Number of points taken.....	45
Figure 29: Magnetic field form IGRF model in X, Y and Z direction Vs Number of points taken.....	46
Figure 30: Magnetic field form both WMM and IGRF model in X, Y and Z direction Vs Number of points taken	46
Figure 31: Magnetic Field in X, Y and Z Axis Vs Height for WMM and combined model of IGRF Model.....	47
Figure 32: Magnetic Field in X, Y and Z Axis Vs Height for WMM Model.....	47
Figure 33: Magnetic Field in X, Y and Z Axis Vs Height for IGRF Model.....	47
Figure 34: Magnetic Field in X, Y and Z Axis Vs Height for WMM and IGRF Model.....	47
Figure 35: Flowchart Depicting the estimation by minimalizing error	48
Figure 36: Diagram showing Direction of Spacecraft with respect to Heading Angle and angle of ideclination	49
Figure 37: Reference Frame Transformation where, b- body frame, m- magnetometer reference frame.....	50
Figure 38: Figure Showing-	52
Figure 39: No magnetometer reading.....	52
Figure 40: Magnetometer aided Gyro heading at sampling frequency $f=10\text{Hz}$	53
Figure 41: Gyro rate bias is not estimated since the magnetometer is not used.....	53
Figure 42: Gyro rate bias estimation slow at 10 Hz.....	54
Figure 43: Magnetometer aided gyro heading error.....	54
Figure 44: Magnetometer aided gyro heading error.....	55
Figure 45: At 40 Hz, gyro rate bias estimation faster than at 10 Hz	55
Figure 46: Over a shorter ($t=0-50\text{s}$) duration	56
Figure 47: Gyro-rate noise with gyro rate bias.....	56
Figure 48: Magnetometer Aided-Gyro heading Error	57
Figure 49: 3D CAD Design of the momentum wheel.....	59
Figure 50: Images of the Experimental setup.....	61
Figure 51: Complete Circuit of Power System	62
Figure 52: DC-DC Bulk converter before and after Power.....	62
Figure 53: Complete experimental single motor setup.....	63

Figure 54:(a) PWM in Zero RPM (b)PWM in counter-clockwise full RPM	64
Figure 55: PWM in clockwise full in a digital oscilloscope.....	64
Figure 56: Experimental Setup with 3 motors.....	66
Figure 57: The SHOURYA	67
Figure 58: Left, we have side view to see the orifice and the two other hole for support screw. In the right we have top view to see the actual orifice.....	68
Figure 59:The Isometric View for proper view.	68
Figure 60:Top view of the Hemispherical bottom of the top section(unit in mm).....	69
Figure 61:Detail 2D drawing of the head of the lower section. Left side is the top view and right side is the side View(unit in mm).	70
Figure 62: Detail 2D drawing of the momentum wheel. Left side is the top view and right side is the side view(unit in mm).	70
Figure 63: Isometric view of the Hemispherical bottom	71
Figure 64:Isometric view of the momentum wheel	72
Figure 65: Isometric view of the top side of the head of the lower base.....	72
Figure 66: Isometric view of the bottom side of the head of the lower base.	73
Figure 67:Cost reduction due to Analysis and innovation.....	74
Figure 68: Previously made structure where the red stripes shows the indication of the possible failure.	75
Figure 69:top-Bottom side of the final design, Bottom image: top side of the final Design of lower base head.	76
Figure 70: Buckling is shown on a particular load distribution due to rotation, so the material selection is done accordingly.	77
Figure 71: Acoustic Analysis of a previously made structure and the area of failure can be identified.	78
Figure 72: The gradual fading of vibration of the Upper Head.....	79
Figure 73:Shows the complete vibration distribution radially.	79
Figure 74:Air flow analysis.....	80
Figure 75:Image of proposed design and Actual model.....	81
Figure 76: Complete Manufacturing Process	82
Figure 77:Complete electrical integration with proper connections	82
Figure 78: Lower hemispherical part being printed in 3D printing Machine.....	83

Figure 79: Complete task of (1) Lower hemispherical Part and (2) Head of the lower base.	84
Figure 80: Complete Machined Momentum Wheel.....	84
Figure 81:Complete line of production of the momentum wheel.	85
Figure 82: Complete line of action of Machining	86
Figure 83: On left: L-bracket are placed, equally spaced. on right side: The cylindrical hollow section is placed and fixed with the L-bracket.	86
Figure 84: Stand being printed in blue and black	87
Figure 85:Octopus connector for connection ESC.....	88
Figure 86: Air delivery channel.....	88
Figure 87: Air delivery channel being connected to the air pipe channel.	89
Figure 88: Exactly at the centre of Helmholtz Cage.....	91
Figure 89:Top view and Side view of the upper part of the system.....	92
Figure 90: Complete Structure inside the Helmholtz Cage.	92
Figure 91:Direct computer feed from the sensor.....	93
Figure 92: IMU mount above the testing bed.	93
Figure 93: Visualization along the X-Axis.....	94
Figure 94:Visualization along the Y-Axis.....	95
Figure 95:Visualization along the Z-Axis	95
Figure 96: The acceleration in all 3 direction.	96
Figure 97: The delta velocity value in all the direction with x axis as the time step.	96
Figure 98:Delta velocity in slow manoeuvring in all three axis with x axis as the time step.....	97
Figure 99:Acceleration in slow manoeuvring in all three axis with x axis as the time step.....	97
Figure 100:Acceleration in fast manoeuvring at all three axis with x axis as the time step.....	97
Figure 101:Delta velocity in fast manoeuvring at all three axis with x axis as the time step.....	97
Figure 102:Delta angle in automated algorithm	98
Figure 103:Angular rate in automated algorithm.....	98

LIST OF TABLE

Table 1: Modes of Operation of the ADCS	4
Table 2: Helmholtz Cage specification.....	7
Table 3: Milli-Gauss Meter Specifications.....	7
Table 4: Tachometer Specifications	8
Table 5: Typical key Characteristics of HG1120	9
Table 6: Typical performance in stable room temperature.....	9
Table 7: Detail of all the Parameters	16
Table 8: To show the average value from the data	25
Table 9: Value of current for Calibration	27
Table 10: IMU Calibrated data for two Same Experiments	28
Table 11: Comparing the two Models (IGRF-13 AND WMM2020).....	32
Table 12: Detailed comparison of geomagnetic field with results	32
Table 13: Theoretical and Experimental Values with Error and error percentage for X-Axis.....	35
Table 14: Theoretical and Experimental Values with Error and error percentage for Y-Axis.....	36
Table 15: Theoretical and Experimental Values with Error and error percentage for Z-Axis.....	37
Table 16: Table of theoretical and experimental magnetic field value in all 3 -Axis.....	38
Table 17: Summery of all 6 Orbital Parameters	41
Table 18: RPM Variation with Voltage.....	63
Table 19: Table to Study the RPM difference with the voltage variation.....	65
Table 20: Table for future aspect of my project.	101

ACRONYMS

Acronym	Full Form	Description
ADCS	Attitude Determination and Control System	System used to determine and control a spacecraft's orientation.
ADS	Attitude Determination Subsystem	Subsystem responsible for sensing and calculating orientation.
ACS	Attitude Control Subsystem	Subsystem that applies corrective actions to change or maintain orientation.
IMU	Inertial Measurement Unit	Sensor module combining gyroscopes, accelerometers, and sometimes magnetometers.
RW	Reaction Wheel	A momentum exchange device used to control spacecraft attitude.
MTQ	Magnetorquer	Device that uses magnetic fields to generate torque for satellite control.
CMG	Control Moment Gyroscope	Advanced actuator for high-torque attitude control.
CoG	Centre of Gravity	The point at which the mass of the system is balanced.
CoP	Centre of Pressure	The point where aerodynamic pressure forces are centred.
TRIAD	Tri-Axis Attitude Determination	An algorithm using two non-collinear vectors to determine attitude.
KF	Kalman Filter	Statistical algorithm used for sensor fusion and bias correction (e.g., gyro bias).
Gyro Bias	Gyroscope Bias	A slowly varying offset in gyroscope readings that affects long-term accuracy.
DAQ	Data Acquisition System	System used to collect sensor and telemetry data.
LVDT	Linear Variable Differential Transformer	Precision sensor used in air bearing setups for displacement measurement.
PCB	Printed Circuit Board	Used for mounting and interconnecting electronics.
CFD	Computational Fluid Dynamics	Used in air flow analysis and air bearing design.
PLA	Polylactic Acid	A 3D printing material often used in rapid prototyping.
CF	Carbon Fiber	High-strength, lightweight material used in structural components.
CAD	Computer-Aided Design	Software used for designing 3D models.
FEM	Finite Element Method	Numerical method used for structural and acoustic analysis.

Chapter 1: Introduction

1.1 Background

Earth-orbiting satellites are essential for providing extensive coverage, meteorological research, and global access to various services. These include telecommunications, climate monitoring, scientific investigations, positioning systems, and information gathering. The satellites delivering these services rely on highly accurate systems to maintain their spatial orientation, known as attitude. This refers to the spacecraft's alignment relative to specific reference points such as Earth, the Sun, or distant celestial bodies. While some fundamental scientific missions or less complex satellites may not require precise attitude control, the majority of satellites necessitate accurate pointing to ensure stable antenna communication links or proper tracking of Earth locations by onboard imaging equipment[1].

Earth-orbiting satellites are vital for services such as telecommunications, climate monitoring, navigation, and scientific research. To perform these functions effectively, satellites must maintain precise orientation in space, known as attitude. The Attitude Determination and Control System (ADCS) is responsible for measuring and adjusting this orientation.

The ADCS comprises two main components:

- Attitude Determination Subsystem (ADS): Utilizes sensors like sun sensors, star trackers, gyroscopes, and magnetometers to ascertain the spacecraft's current orientation.
- Attitude Control Subsystem (ACS): Employs actuators such as reaction wheels, control moment gyroscopes, magnetorquers, and thrusters to adjust the spacecraft's orientation as needed.

These components work in tandem, with control algorithms processing sensor data to determine necessary adjustments, ensuring the satellite maintains or achieves the desired orientation.

In recent years, CubeSats—small, cost-effective satellites—have become popular for testing new space technologies, including ADCS components. Their compact size and lower development costs make them ideal for educational purposes and technology demonstrations, despite some limitations in capabilities compared to larger satellites.

Overall, the ADCS is essential for satellite operations, enabling accurate positioning for communication, imaging, and other mission-critical tasks. While offering similar fundamental components and subsystems as larger satellites, CubeSats do so at reduced costs and with quicker development cycles. However, their diminutive size and limited resources result in some trade-offs in capabilities and performance. CubeSats often serve as demonstrator missions to validate novel technologies before their implementation in more substantial, costly satellite systems. Additionally, they provide valuable practical experience to students and researchers in space system design, development, and testing, nurturing the future generation of aerospace experts.

1.2 Recent works

Attitude Dynamics and Control (ADC) is a pivotal area in spacecraft engineering, enabling satellites to maintain or adjust orientation for mission-critical operations. Leading institutions worldwide contribute to this evolving field:

- Stanford University (SSDL) and MIT explore advanced control systems using reaction wheels, magnetorquers, and autonomous algorithms.
- University of Colorado Boulder (LASP) develops new sensors and actuators for diverse space environments.
- Caltech (JPL) focuses on attitude stabilization for deep-space missions.
- Other major contributors include University of Cambridge, Georgia Tech, University of Michigan, University of Texas at Austin, and EPFL and Imperial College London, which apply machine learning and sensor fusion.
- Institutions like Tsinghua University, Aalto University, and University of Toronto are innovating low-cost ADCS solutions for CubeSats and small satellites.

To test sun sensors and magnetometers, basic tools like flashlights and Helmholtz coils are used. For three-axis control, a Helmholtz cage—comprising three perpendicular coil pairs—provides a controlled magnetic environment.

ADCS is vital across all mission scales: enabling Earth-observation satellites to maintain camera orientation, communication satellites to ensure link stability, and scientific missions like Hubble or JWST to achieve precise celestial tracking.

1.3. Role of the ADCS

Satellites have a subsystem known as the Attitude Determination and Control System (ADCS), which is a vital part that ensures accurate orientation in order to successfully accomplish mission objectives. Ensuring consistent pointing for communication, aligning antennas with ground stations or other satellites, and supporting Earth observation and imaging by focusing sensors for high-resolution data gathering are all functions that it does. When it comes to orbital corrections, docking, and rendezvous operations, the ADCS is responsible for optimizing the alignment of solar panels to ensure maximum power generation, stabilizing scientific instruments to ensure precise data collecting, and easing these activities. In addition to this, it plays a significant part in avoiding the growth of space debris, the stabilization of the satellite once it has been deployed, and the handling of thermal control by modifying the orientation in order to achieve a balance in heat distribution or to prevent the satellite from overheating. Individually and collectively, these qualities enable it practicable for the satellite to function effectively, carry out difficult tasks, and adjust to the ever-changing conditions of orbits.

1.4 Modes of operation of the ADCS

To meet the demands of the operation and the various stages of a mission, a satellite's Attitude Determination and Control System (ADCS) can operate in a variety of modes. Through the use of various modes, the spacecraft may perform specific tasks, from initial deployment to precise orientation maintenance during crucial activities. Numerous factors, such as the mission's goals, the satellite's configuration, and the surrounding conditions, influence the mode that is chosen. There are several ways that the ADCS operates, some of which are listed below:

	Mode	Purpose	Functionality	Sensors Used	End Condition
1	Detumbling Mode	Stabilize the satellite after deployment to reduce unwanted spinning or tumbling.	Uses actuators (magnetorquers, thrusters) to reduce rotational rates.	Magnetometers, gyroscopes	When angular velocity is reduced to acceptable levels.
2	Sun Acquisition Mode	Align solar panels with the Sun for maximum power generation.	Orients the satellite to face solar panels toward the Sun.	Sun sensors, gyroscopes	Once solar panels are aligned with the Sun.
3	Earth Pointing Mode	Keep the satellite's payload, sensors, or antennas pointing toward Earth.	Maintains a fixed orientation relative to Earth for communication or imaging purposes.	Earth horizon sensors, star trackers, gyros	Continuously maintained as required by mission.
4	Inertial Pointing Mode	Point satellite toward a fixed target in inertial space (e.g., stars, celestial bodies).	Holds the spacecraft in a fixed orientation relative to the inertial frame.	Star trackers, gyroscopes, Sun sensors	Operated during observation or communication with specific targets.
5	Target Tracking Mode	Track a moving target, such as a location on Earth or another satellite.	Continuously adjusts satellite's orientation to follow the target.	Optical sensors, star trackers, gyroscopes	Maintained until target is no longer needed.
6	Spin Stabilization Mode	Use angular momentum to passively stabilize the satellite.	Satellite spins around one axis to maintain stability.	Gyroscopes, magnetometers	Operated during low-power or simple mission phases.
7	Safe Mode	Protect satellite during anomalies or failures.	Conserves power and keeps basic functionality; aligns solar panels with the Sun.	Sun sensors, magnetometers	Remains until problem is rectified and ground control commands return to normal mode.
8	Orbit Control Mode	Execute orbital manoeuvres and station-keeping operations.	Provides orientation for orbital adjustments using thrusters.	Gyroscopes, star trackers	Once the orbital adjustment is complete.
9	Magnetorquer Control Mode	Control attitude using Earth's magnetic field (mainly for small satellites or CubeSats).	Manages magnetorquers to control the satellite's orientation.	Magnetometers	Used for extended periods or until more precise control is required using reaction wheels or thrusters.

Table 1: Modes of Operation of the ADCS

1.5 Ultimate Objectives

Main objective is to Study, Simulate and design Attitude determination and control System (ADCS). The following are the basic objective planned for this project:

- **Objective 1:** Simulation of magnetic field in a defined trajectory of a Spacecraft using a Helmholtz Cage Setup

- **Objective 2:** Develop a Single Axis Bi-Directional Momentum Control Wheel System
- **Objective 3:** Gyro rate bias Estimation using Heading Estimation.
- **Objective 3:** Design the Complete 3D Structure and do detail analysis.
- **Objective 4:** Make the Electrical Integration with microcontroller and start the 3D print with the momentum wheel production by manual machining.
- **Objective 5:** Completely integrate the structure and validate results.

Chapter 2: Literature Review

This chapter deals with the various components and equipment that are being used in this project. The laboratory equipment and instruments used in the process of the research is included in this chapter.

2.1. Apparatus:

2.1.1. Helmholtz Cage:

Schematic representation of the Helmholtz cage in the laboratory is shown here. A device that is designed to generate a magnetic field that is uniform along their common axis is referred to as a Helmholtz cage. The structure is made up of two circular or square coils that are identical to one another and are arranged in a parallel fashion. These coils are separated by a distance that is equal to their radius or side length. In order to generate consistent fields in each direction at its centre, a Helmholtz Cage is created by three Helmholtz Coils that are arranged in an orthogonal fashion.

The motion of charge, sometimes referred to as current, results in the existence of magnetic field B. I proceed in the other direction through the coil pair using the right-hand rule. The magnetic field at the location roughly in the centre of the two coils can be found and is computed using:

$$B = \frac{32\pi NI}{5\sqrt{5}a} \times 10^{-7}$$

where I is the current flowing through the coils, N is the number of turns per coil, a is the coils' radius, and B represents Tesla units [5][24][39].



Figure 2: Helmholtz Cage in the Laboratory

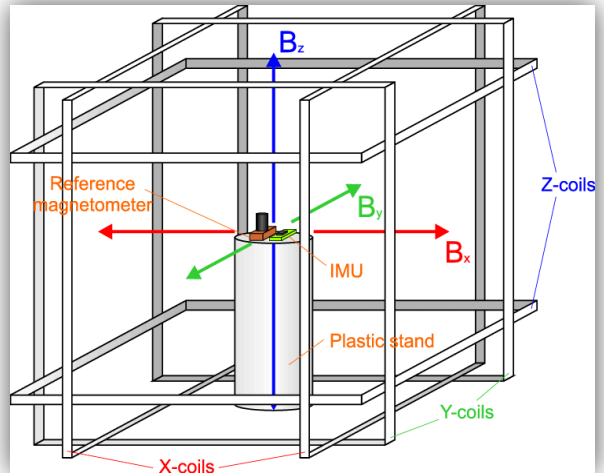


Figure 1: Schematic diagram of Helmholtz Cage

Parameters	Specification
Total number of coils	6
Max field generation capacity	160 T =1600 milli-gauss
Maximum current per axis	5A
Nominal voltage per axis	22V
Control volume	300x300x300 mm
Deviation of magnetic field	<1%
Deviation of the field vector	$\pm 0.1^\circ$
Power Supply	30 V DC, 5A per axis

Table 2: Helmholtz Cage specification

2.1.2. Milli-Gauss Meter (GU-3001):

The device is a DC/AC milli-Gauss magnetometer designed to measure both direct current (DC) and alternating current (AC) magnetic fields. It features a wide measurement range, capable of detecting magnetic field strengths up to 3,000 milli-Gauss, and includes a sensitivity level that can detect magnetic fields as small as 0.1 milli-Gauss. The instrument is equipped with an indicator to differentiate between the north (N) and south (S) magnetic poles[24][26].

This instrument is used to measure the magnetic field in each axis. I have used it in the measurement of the uniaxial System.

Specifications:

Parameters	Specification
Display Size	52mm X 38mm
Measuring Unit	Milli-Gauss(mG), Micro-Tesla(uT)
Maximum current per axis	5A
Measuring Range	-3000 mG to 3000 mG
	-300uT to 300uT
Accuracy	$\pm (2\% + 2 \text{ mG})$
Resolution	0.1mG (-199.9 to 199.9mG)
Field Direction	Uni-Axial
Power Supply	9 V DC, 2.5 mA
Operating Humidity	< 85% RH

Table 3: Milli-Gauss Meter Specifications

2.1.3. Tachometer (GU-3001):

This digital tachometer is intended to measure rotational speed (RPM) and surface speed of rotating objects in a quick and exact manner without contact. It combines modern CPU technology, photoelectric techniques, and junction laser technology in one instrument to improve performance. The gadget has two testing modes: rotation speed, which is measured in RPM (revolutions per minute), and count, which is measured in REV. It has a broad measuring range and great resolution, ensuring accuracy across a variety of applications.

Specifications:

Parameters	Specification
Detecting Distance	50 mm to 500 mm
Accuracy	$\pm (0.5\% + 1 \text{ Digit})$
RPM test Range (RPM)	2 to 99,999
Count Range (REV)	1 to 99,999 Revolution
Sampling Time	0.5 Sec (Over 120RPM)
Power Consumption	Approx 45 mA
Operating Temperature	0°C to 50°C

Table 4: Tachometer Specifications



Figure 3: Tachometer



Figure 4: Milli-Gauss meter

2.1.4. IMU Sensor (HG1120):

The high-performance micro-electro-mechanical system (MEMS) inertial measurement unit (IMU) HG1120 was created to satisfy the demands of applications in a number of industries, such as robotics, survey/mapping, agriculture, AUVs, industrial equipment, transportation, stabilized platforms, UAVs, and UGVs [1]. The HG1120's broad input voltage range and industry-standard communication interfaces make it simple to include into a variety of systems. The HG1120 is perfect for the majority of applications due to its small size, low power consumption, and light weight. The HG1120 is a 9 degrees of freedom (DOF) IMU that has MEMS gyroscopes, accelerometers, and magnetometers. The HG1120 also uses an internal environmental isolation system to reduce undesired inputs that are frequently present in practical applications. The HG1120 is sufficiently robust to satisfy the demands of the most exacting customers thanks to internal isolation and other exclusive design elements. The HG1120 has nine degrees of freedom, meaning it can detect motion in nine different ways: three axes (X, Y, Z) for acceleration, three axes (X, Y, Z) for rotation, and three axes (X, Y, Z) for magnetic field.

HG1120 IMU TYPICAL KEY CHARACTERISTICS	
Gyroscope Operating Range	-500°/sec to +500°/sec
Accelerometer Operating Range	-16g to +16g
Magnetometer Operating Range	-16 gauss to +16 gauss
Supply Voltage	+3.0 to +5.5 VDC
Power Consumption	< 0.4 Watts
Operating Temperature Range	-40°C to 85°C
Volume / Size	29 cm ³ (1.7 in ³), 4.70 cm x 4.39 cm x 1.41 cm
Weight	54 grams (0.12 lbs) Typical
Selectable Data Rates	Incremental/Control Data Rates of 100 Hz/600 Hz or 300 Hz/1800 Hz
Baud Rate	1MBit CAN/RS422, 2-9 MBit SPI
Dual Navigation/ Control Serial Outputs	Fully Compensated Incremental/Delta Outputs are Ready for Integration into Position/Attitude Control Message Optimizes Latency & Bandwidth Without Sacrificing Accuracy

Table 5: Typical key Characteristics of HG1120

HG1120 IMU STANDARD MODELS TYPICAL PERFORMANCE- STABLE ROOM TEMPERATURE						
Variant	Gyro Bias Repeatability (°/hr 1σ)	Gyro Bias In-run Stability (°/hr 1σ)	ARW (°/√hr)	Accel Bias Repeatability (mg 1σ)	Accel Bias In-run Stability ¹ (mg 1σ)	VRW (m/s/√hr)
HG1120CA50	260	10	0.3	5	0.03	0.050
HG1120BA50	520	24	0.4	10	0.05	0.015
HG1120AA50	780	48	0.5	15	0.08	0.025

Table 6: Typical performance in stable room temperature.

2.1.5. Power Module (XL4016):

The module has a maximum output power of 300W and a conversion efficiency of up to 95%. Its input voltage range is 7V to 30V DC, and its output voltage may be adjusted between 0.8V and 28V DC and 0-10A. It protects against short circuits, overheating, and dynamic reaction speed. It is designed to be versatile, since it can power laptop computers from automobile batteries, run communication equipment, drive low-voltage DC motors, and act as a step-down or solar battery charger. Its adjustable constant current (CC) and constant voltage (CV) features make it perfect for lab power supplies and LED illumination. To avoid damage, fire, or personal harm, certain precautions must be taken, such as avoiding continuous maximum-rated loads, employing circuit protection, and providing cooling over 65°C. To ensure safe operation, the output voltage must always be lower than the input.

Chapter 3: Earth's Magnetism

This chapter gives an overview of the earth's geomagnetic field, study of which enhances the understanding of the subsequent chapters.

3.1. Theory of Geomagnetism

The Earth's poles are positioned around its axis of rotation, and its magnetic field is similar to that of a bar magnet. This suggests that true north and magnetic north are nearly in line with the orientation of the horizontal component of the Earth's magnetic field. A functional reference could be a compass or magnetic field sensor.

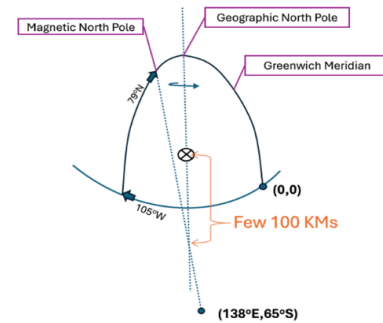


Figure 5: Geodetic and Magnetic Pole

There is variation in the angle between magnetic and true north. Time and the observation's location on Earth affect it, but both can be compensated for. The Earth's magnetic field orientation at each point is defined by its angle with respect to true north, called the angle of magnetic declination (or magnetic variation), and its angle with respect to the horizontal, called the angle of dip. Vehicle orientation can be deduced from the magnetometer's data by using the angle of dip and the difference between true and magnetic north. Position fixes might theoretically be achieved by matching magnetic anomalies or by comparing field measurements inside the local geographic frame with recorded maps of magnetic variation and dip angle. To get accurate fixes, the prior approach required precise knowledge of both the local vertical and true north. The latter plan, which is similar to the terrain matching method that compares in-flight measurements from an on-board radar altimeter with a contour map of the terrain, would obviously rely on the stability of these anomalies and the availability of adequately comprehensive magnetic anomaly maps. High positional fix accuracy could be achieved with this method in regions having a large number of consistent and significant anomalies.

From the magnetic north pole to the magnetic south pole, the Earth's geomagnetic field moves through the planet before reentering the upper atmosphere. Consequently, the magnetic field is vertical at the poles and horizontal at the equator. The magnetic poles' positions shift with time. On January 1, 2010, the North Pole was located at latitude

80.08° and longitude -72.21°, while the South Pole was located at latitude -80.08° and longitude 107.79°. In this configuration, the field's angle with respect to the Earth's rotational axis is 9.92°. The force per unit length resulting from magnetic induction is the vector product of the current and flux density vectors, which is represented by the magnetic flux density vector. The SI unit of magnetic flux density is the Tesla (T), whose formula is $1 \text{ T} = 1 \text{ N/Am}$. It is commonly represented by the notation B . According to the nomenclature used here, this would be a matrix; however, b is incompatible with the instrument biases, so m has been chosen in its stead. The flux density of the Earth's geomagnetic field, represented by the subscript E , can be expressed as follows when resolved about the axes of a local navigation frame:

$$m_E^n(p_b, t) = \begin{pmatrix} \cos \alpha_{nE}(p_b, t) \cos \gamma_{nE}(p_b, t) \\ \sin \alpha_{nE}(p_b, t) \cos \gamma_{nE}(p_b, t) \\ \sin \gamma_{nE}(p_b, t) \end{pmatrix} B_E(p_b, t)$$

where B_E is the magnitude of the flux density, α_{nE} is the declination angle or magnetic variation, and γ_{nE} is the inclination or dip angle of the Earth's magnetic field. *All three parameters vary as functions of position and time.*

Note: In some countries, national models with higher resolution are available. Every day (day-night), the geomagnetic field varies by about 50 nT. Furthermore, magnetic storms brought on by solar activity can cause transient alterations in the Earth's magnetic field. At latitudes above 80°, the effect on the declination angle varies from roughly 0.03° at the equator to more than 1°. The subscript m stands for total magnetic flux density, which is measured by magnetometers along the axes of their body frame[33][34][35]. The body frame is represented by b , assuming that the axes of any inertial sensors are in line with those of the magnetometer. Thus, the magnetometers take measurements.

$$m_m^b = C_n^b \begin{pmatrix} \cos \alpha_{nm} \cos \gamma_{nm} \\ \sin \alpha_{nm} \cos \gamma_{nm} \\ \sin \gamma_{nm} \end{pmatrix} B_m$$

Where B_m is magnitude, α_{nm} is declination, and γ_{nm} is dip of the total magnetic flux density.

$$m_m^b = \begin{pmatrix} \cos \theta_{nb} & 0 & -\sin \theta_{nb} \\ \sin \theta_{nb} & -\cos \phi_{nb} & \sin \phi_{nb} \cos \theta_{nb} \\ \cos \phi_{nb} \sin \theta_{nb} & \sin \phi_{nb} & \cos \phi_{nb} \cos \theta_{nb} \end{pmatrix} \begin{pmatrix} \cos \psi_{mb} \cos \gamma_{nm} \\ \sin \psi_{mb} \cos \gamma_{nm} \\ \sin \gamma_{nm} \end{pmatrix} B_m$$

ϕ_{nb} is roll, θ_{nb} is pitch, ψ_{mb} is magnetic heading Given by: -

$$\psi_{mb} = \psi_{nb} - \alpha_{nm}$$

*When the roll and pitch are Zero, a magnetic heading can be obtained from magnetometer measurement using:

$$\bar{\psi}_{mb} = \arctan_2(-\tilde{m}_{m,y}^b, \tilde{m}_{m,x}^b)$$

The Earth's geomagnetic field is represented by three main Earth magnetic models. The most popular is the World Magnetic

Model (WMM), which serves as a global standard reference for geomagnetic data.

For purposes like satellite operations and navigation, it is updated often to

guarantee accuracy. A more thorough and

scientifically accurate depiction of the

Earth's magnetic field, including the

secular variation over time, is provided

by the International Geomagnetic Reference Field (IGRF) model, which is updated every five years.

Prioritizing research, the Enhanced Magnetic Model (EMM) combined data from satellite, marine, aeromagnetic, and ground magnetic

surveys. It is now outdated and was in use until 2019. Its goal was to provide a more accurate

field representation for cutting-edge scientific study by capturing subtler crustal fluctuations in

the magnetic field that were not taken into

consideration by the WMM. However, more precise models and methods have replaced the EMM, therefore it is no longer in use[5].

Magnetic fields B are measured in gauss (volt-sec/m= weber/cm²) and 1tesla=10⁴ gauss). In geomagnetism, units of "gamma" (10⁻⁵ gauss) are used.

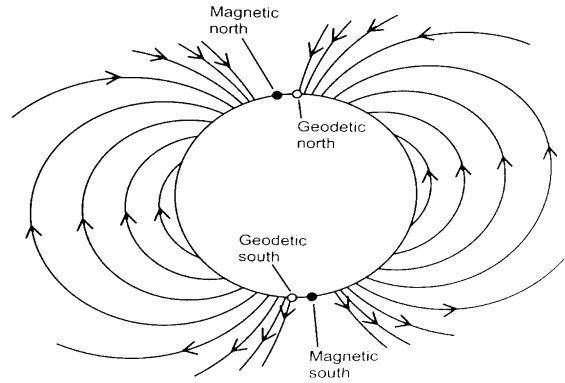


Figure 7: Geodetic and Magnetic pole Diagram

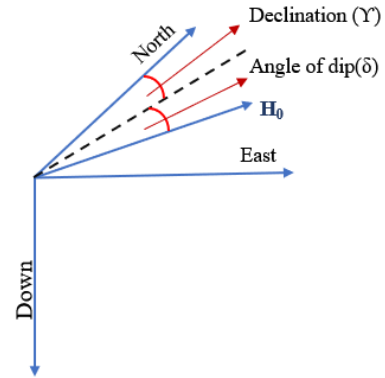


Figure 6: Components of earth's Magnetic Field

A bar magnet (dipole) positioned 11 degrees from the spin axis and passing within a few hundred kilometres of the Earth's center generates the magnetic field to the first order. At the start of 1996, the north magnetic pole in the Northern Hemisphere was located at 79° N latitude and 105° W longitude, while the south magnetic pole was located at 65° S and 138° E [7]. Near the equator, the field strength is 0.3 gauss, while near the poles, it is 0.6 gauss. The dip angle is the depression of B from the horizontal at

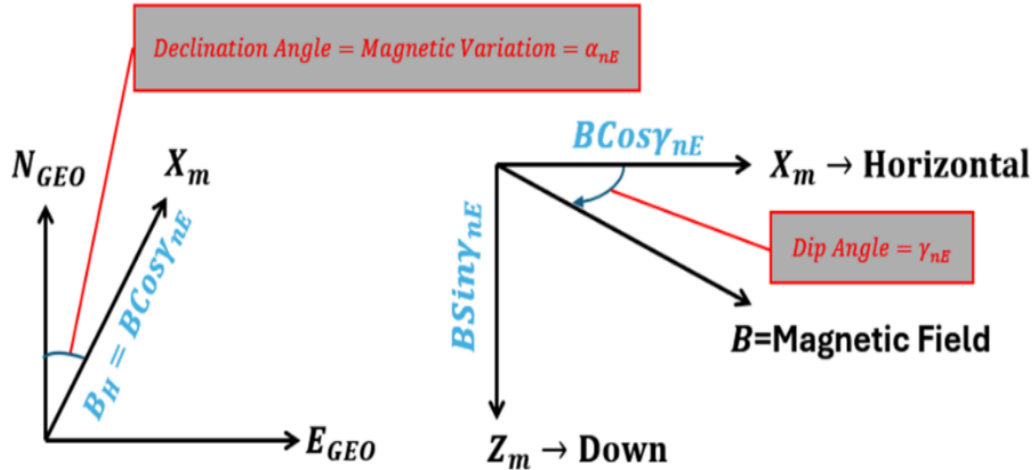


Figure 8: Magnetic field frame

any given point; it is 90 degrees at the poles and zero at the magnetic equator. The angle between the horizontal component of B and true north is known as the magnetic declination, magnetic variation, or magvar. The term "magvar" is used by navigators to distinguish between magnetic and astronomical declination. On the East Coast of the contiguous United States, magnetic north is 10 degrees west of true north, while on the West Coast, it is 20 degrees east.

More specifically, a spherical harmonic series describes the Earth's magnetic potential function [5].

The main concern of navigators is magvar, which can be added to magnetic heading by an aircraft computer to determine true north. In the 1950s and 1960s, when airborne digital computers were less capable of navigation, Magvar cams were integrated into analog and airborne computers to process this harmonic equation of the WWM or IGRF on the ground. to determine the magnetic variation in tables ranging from one to two degrees. [7]

3.2. Output Arguments:

1. XYZ: Vector of magnetic field: A vector or matrix of the same size as the input matrix plus one extra dimension, the last dimension, representing the magnetic field in nanotesla (nT). The X, Y, and Z components of the magnetic field are specified by the third and final dimension of the matrix, which has a size of 3. Vertically, Z represents the "Positive down" component. All of this vector's components are located in the NED reference frame.

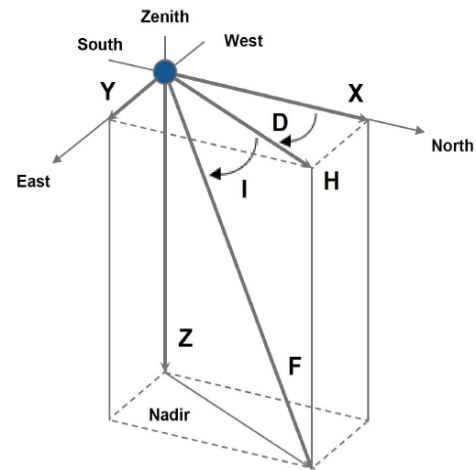


Figure 9: 3D Notation of all the Arguments

Second, H stands for "horizontal intensity," which can be either a scalar, a vector, or a matrix with dimensions equal to those of the input matrix in nanotesla (nT).

3. D: Declination: The input matrix's size is equal to the declination, which is returned as a scalar in degrees (Positive east).

4. I: Inclination: The output is a scalar with the same dimensions as the input matrix, representing the inclination in degrees (Positive down).

5. F: Total intensity: The input matrix's size has the same unit of measurement as the total intensity, which is returned as a scalar in nanotesla (nT).

6. DXDYDZ, represents the secular variation in the magnetic field vector. This variation is returned as a matrix or vector with dimensions of the same size as the input matrix plus one more dimension, the last dimension, and is measured in nT/year. The X, Y, and Z components of the magnetic field are specified by the third and final dimension of the matrix, which has a size of 3. Vertically, Z represents the "Positive down" component.

7. DH: Secular variation in horizontal intensity: In nT/year, the scalar value that is

returned is the secular variation in horizontal intensity; it is the same size as the input matrix.

Element	Name	Alternative Name	Range at Earth's Surface			
X	North component	Northerly intensity	-17000	43000	nT	North
Y	East component	Easterly intensity	-18000	17000	nT	East
Z	Down component	Vertical intensity	-67000	62000	nT	Down
H	Horizontal intensity		0	43000	nT	
F	Total intensity	Total field	23000	67000	nT	
I	Inclination	Dip	-90	90	Degree	Down
D	Declination	Magnetic variation	-180	180	Degree	East / Clockwise
GV	Grid variation	Grivation	-180	180	Degree	East / Clockwise

Table 7: Detail of all the Parameters

3.3. Magnetic Models

Any point on Earth can have its magnetic declination determined by the World Magnetic Model (WMM).

From 1 km below the World Geodetic System (WGS 84) ellipsoid surface to 850 km above it, the World Magnetic Model (WMM) gives magnetic declination and magnetic field geometry. Extremes of the magnetic field, which extend far into space and Earth, are not covered by the WMM.

A magnetic dipole is produced by a uniformly magnetized spherical Earth. While the opposing pole just outside the Antarctic Circle shifts 10–15 km annually, the dipole's "south" in the northern hemisphere migrates westward roughly 55–60 km annually. Earth's magnetism comes from the magnetic field of the liquid-iron outer core, or the "core field." Locally significant contributions can be made by magnetic materials found in the upper mantle and crust. All internal fields and their intricate constituents are included in the WMM.

Time-varying external magnetic fields from electric currents in the upper atmosphere and near-Earth space, which are primarily caused by the solar wind, are not included in

the WMM.

It is estimated that local magnetic dipoles are produced by secondary thermal convection currents close to Earth's core-mantle. To mimic the multipole nature of the magnetic field, these dipoles are stacked. Magnetic drift may result from the formation and breakdown of internal convection currents. The potential gradient, V , can be used to represent the magnetic flux density (magnetic field), B :

$$B = -\nabla V$$

This has a convenient solution expressed in spherical harmonics of n degrees:

$$V(r, \theta, \phi, t) = a \sum_{n=1}^N \sum_{m=0}^n \left(\frac{a}{r}\right)^{n+1} (g_n^m(t) \cos(m\phi) + h_n^m(t) \sin(m\phi)) P_n^m(\cos\theta)$$

where a is Earth's mean radius; g_n^m and h_n^m are *Gaussian coefficients* of degree n and order m ; r , θ , and ϕ are the *geocentric radius, elevation, co-elevation and longitude in spherical polar coordinates*; and $P_n^m(\theta)$ are the associated Legendre functions. With a degree, $n=1$ only dipoles are considered. For $n=2$ the quadrupoles, $n=3$ the octupoles, and so on. This WMM's methodology extends to degree and order 12. The WMM also uses a linear model to account for the secular variation (SV), which is the core field's annual change. The WMM coefficient values are updated every five years (a lustrum) due to erratic changes in the core field. From 2020 to 2024, the most recent version is in effect.

3.3.1. World Magnetic Model (WMM)

Limitations: -

Five years after the model's epoch, which begins on January 1 of the selected model year, the WMM specification generates reliable data. Only the long-wavelength spatial magnetic variations coming from the Earth's core are defined by the WMM standard. Short and intermediate wavelength fluctuations that come from the crustal field (the crust and mantle) are not included. The substantial geomagnetic field volatility, which occurs constantly during magnetic storms and almost constantly in the disturbance field (auroral zones), is not taken into consideration. The World Magnetic Model places

restrictions on this function (WMM). According to the World Magnetic Model 2020 Technical Report, WMM2020 can be used in the altitude range of -1 km to 850 km.

3.3.2. International Geomagnetic Reference Field (IGRF)

Limitations: -

The following year ranges are covered by this function: 1900 and 2025 for the IGRF-13 model; 1900 and 2020 for the IGRF-12 model; and 1900 and 2015 for the IGRF-11 model. This function works between -1000 meters and 5.6 Earth radii (35,717,567.2 meters). The arguments for height, latitude, longitude, and decimal year (matrix, scalar, etc.) must all have the same size[7][8].

3.4. Magnetometer Error Models

The angle created between a spacecraft's longitudinal axis and the north pole is known as heading. It was also mentioned that a magnetometer serves as the main sensor used in this thesis to determine heading. The output of the magnetometer pair would be the horizontal components of the Earth's magnetic field vector, close to the spacecraft, if the traditional two magnetometer installation is being used and the spacecraft containing the magnetometers is level. The three components of the Earth's magnetic field near the spacecraft would be the output of the magnetometer triad if the three-magnetometer configuration was being used. The output from the sensors is tainted by error because of sensor flaws, improper installation, and undesired magnetic fields near the magnetometers.

3.4.1. Background:

The navigation frame is a local coordinate system with axes aligned to the North, East, and Down directions, commonly referred to as the North-East-Down (NED) coordinate system. Vector quantities in this frame are denoted with the superscript “n.” The body frame aligns with the NED frame when an airplane is level and oriented northward, and vector quantities in this frame are indicated by the superscript “b.” The wander-azimuth frame is a locally level, right-handed coordinate system with its x-axis aligned with the projection of the airplane's longitudinal axis, the z-axis aligned with the vertical, and the y-axis orthogonal to both. The angle between its x-axis and the x-axis of the NED frame is the wander angle, and quantities in this frame carry the superscript “w.” Lastly, the

platform frame corresponds to the right-handed coordinate system defined by the sensitive axes of the magnetometer, with vector quantities in this frame denoted by the superscript “p.”

Because the magnetometers only detect a portion of the vertical component of the Earth's magnetic field vector, heading calculations will be inaccurate. Given that the vertical component of the Earth's magnetic vector is frequently larger than the horizontal component, these errors can have serious consequences. Prior to applying Equation 3.1, the vector measurements generated by magnetometers attached to the ship's body axis must be converted to the local level navigation frame if the spacecraft is not operating at a zero-flight path angle. Pitch and roll attitude data generated by an Attitude Heading Reference System (AHRS) are used to make the transition[9]. Heading calculations are performed using Earth's magnetic field vector as expressed in **wander-azimuth coordinates**. In a level spacecraft, Earth's magnetic field vector expressed in wander-azimuth coordinates(\vec{B}^w) is equal to the Earth's magnetic field vector expressed in body coordinates(\vec{B}^b), however, \vec{B}^b has to be transformed into \vec{B}^w before using:

$$\psi = -\tan^{-1} \frac{B_y^b}{B_x^b} \quad (3.1)$$

When the spacecraft is flying straight and level (zero pitch and roll angles), this information about Earth's magnetic field is used to determine aircraft heading with respect to magnetic north pole using the above Equation.

This transformation is accomplished by using a direction cosine matrix in the following manner:

$$\vec{B}^w = C_{b \rightarrow w} \vec{B}^b \quad (3.2)$$

Where, $C_{b \rightarrow w}$ is the body-to-wander-azimuth frame direction cosine matrix and is computed using pitch and roll information only. This pitch and roll information come from an AHRS.

The mathematical model for the output error of a strapdown magnetometer triad is:

$$\vec{B}^n = C_{b \rightarrow w} [C_m C_{sf} C_{si} (\vec{B}^b + \delta \vec{B}^b)] \quad (3.3)$$

Where, $\delta\vec{B}^b$ in Equation 3.3 represents the hard iron biases. The matrix C_{si} accounts for the soft iron errors. C_{sf} is a matrix that takes into account scale factor errors. Finally, the matrix C_m represents misalignment errors. Each one of these error terms is discussed in detail below.

3.4.1 Hard Iron Errors: $\delta\vec{B}^b$

Measure and orient yourself using the Earth's magnetic field. In many real-world applications, the magnetometer trio is close to extraneous magnetic fields. These fields are produced next to the magnetometer by ferromagnetic materials with permanent magnetic properties (referred to as "hard irons"), such as current-conducting wires. The current flowing through these wires will fluctuate over time, influencing magnetometer bias and making calibration more difficult. Magnetometer readings are distorted by the interaction of external magnetic fields with the Earth's magnetic field. Hard iron errors are constant external fields that can be represented as $\delta\vec{B}^b$. By determining the magnitude and direction of these unwanted fields, their effects can be lessened and the magnetometer's readings can be corrected. Although they are typically transient, magnetic fields from outside the spacecraft or experimental equipment may cause disruptions.

3.4.2. Soft Iron Errors: C_{si}

In certain materials, external fields can produce magnetic fields. Depending on the strength and direction of the external magnetic field, these materials produce a broad variety of fields. These irons are soft. When such materials are placed close to a magnetometer, a magnetic field is created that overlays the output. The Earth's magnetic field causes these soft iron materials to produce their own magnetic field. Magnetometer output biases vary because of the aircraft attitude, which affects its orientation with respect to the soft iron. The magnetometer's output is biased by the magnetic field produced by soft iron. A soft iron material produces a magnetic field proportional to an external magnetic field, according to a straightforward one-dimensional model. The proportionality constant of soft iron is its magnetic susceptibility.[9]

3.4.3. Scale Factor Errors: C_{sf}

The magnetometer triad consists of three magnetometers, which should ideally be identical sensors. In practice, the sensitivity of each magnetometer will vary. In other words, an identical magnetic field applied to all three magnetometers will result in different observed outputs. A scale factor error is the cause of this.

3.4.4. Misalignment Errors: C_m

The magnetometer triad should align with the aircraft body axis in ideal installation. Perfect alignment isn't always possible in practice. The magnetometer mismeasures Earth's magnetic field due to this misalignment. To understand this error, visualize a level aircraft with zero roll and pitch angles and the vectors \vec{B}^p and \vec{B}^b . The vector \vec{B}^p is Thus, \vec{B}^p is the error-free output of the magnetometer triad. The vector \vec{B}^b is the magnetometer output expressed in the “b” coordinate frame which is fixed to and aligned with the aircraft’s body axes. If there are no installation errors such that the platform coordinate frame “p” is aligned with the body frame “b,” then the vectors \vec{B}^p and \vec{B}^b would be identical. In this case, the small misalignment can be represented by the perturbation direction cosine matrix, $(\delta C)_{p \rightarrow b}$. In this instance, heading calculations are performed on a modified form of Equation 2.1 which is given as follows:

$$\vec{B}^w = C_{b \rightarrow w}(\delta C)_{p \rightarrow b} \vec{B}^p \quad (3.4)$$

Those mathematical expression are used to correct the real magnetic field and eliminate the unnecessary biases.

Chapter 4: Experiments

4.1. Setup

The following setup are used in the experiment, where the magnetometer is kept over the turntable and the subsequent experiments are performed. The following arrangement are made.

The experimental setup, as s

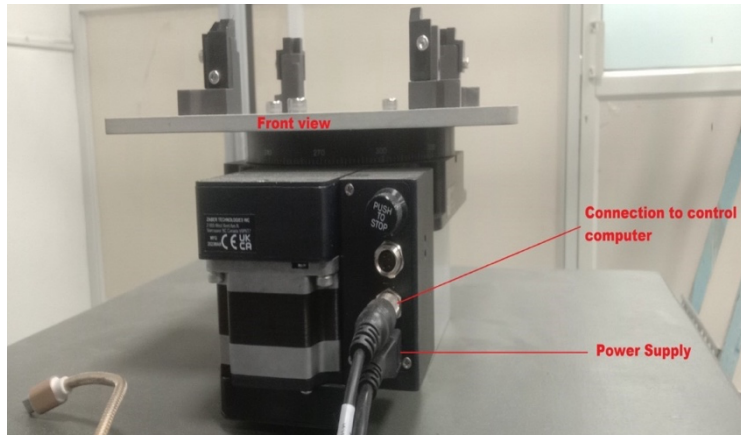


Figure 10: Turntable with Connections



Figure 11: Position of IMU on the turntable (a) Front View (b) Isometric View (c) Top View

system to study the behaviour of a magnetometer placed on a turntable. The following detailed arrangements and considerations are made to ensure the accuracy and reliability of the experimental results:

The magnetometer experiment is exactly designed to ensure accurate and reliable data collection on magnetic field variations. The magnetometer is centrally placed on the turntable to maintain rotational symmetry, securely mounted with non-magnetic fixtures, and levelled to prevent alteration in readings. The turntable, equipped with a motorized system, provides precise rotational control with adjustable speed and high angular resolution through encoders or markings. To minimize external interference, the setup is located in a low-stray-field environment, with optional magnetic shielding and temperature control to maintain instrument sensitivity. All components are constructed from non-magnetic materials[10].

A data acquisition system ensures real-time logging and synchronization of magnetic field readings with angular positions, operating at a high sampling rate for detailed analysis. Calibration steps include baseline measurements, zero-field tests, and validation with reference standards to correct biases or offsets. Position tracking is

achieved using angular scales and digital encoders for precise correlation between rotation and magnetic field data.

Safety and redundancy are emphasized through stable power supplies, backup data storage, and continuous monitoring of equipment. The experiment systematically rotates the magnetometer, recording field variations at different orientations, focusing on patterns and anomalies.

4.2. Experiments

The experiment is designed to achieve two main objectives:

1. **Measure the Geomagnetic Field:** The magnetometer is used to record the Earth's natural magnetic field.
2. **Identify and Quantify External Magnetic Fields:** Determine the influence of nearby devices or objects that generate further magnetic fields.

Approach to Achieving the Objectives

1. Measuring the Geomagnetic Field

To accurately measure the Earth's magnetic field, the following steps are implemented:

- **Zero Measurement:** The magnetometer is calibrated in an environment free of significant external magnetic influences. The initial reading serves as the baseline measurement of the geomagnetic field.
- **Coordinate System Reference:** Data is mapped to geographic coordinates (latitude and longitude) for comparison with known geomagnetic models (e.g., World Magnetic Model).
- **Filtering Noise:** Data processing techniques such as averaging or applying a low-pass filter are used to remove high-frequency noise or transient disturbances.

2. Determining External Magnetic Fields from Nearby Devices

To isolate and measure magnetic fields generated by nearby devices, the experiment involves:

- **Controlled Environment:**
 - The setup is initially performed in a low-noise area to measure the baseline geomagnetic field.
 - External devices (e.g., electrical appliances or electronic equipment) are then introduced one at a time into the vicinity of the magnetometer.
- **Measuring Field Variations:**

- As each device is brought closer to the magnetometer, the changes in the magnetic field are recorded.
- **Field Mapping:**
 - If required, a spatial map of the magnetic field around the device is generated by moving the magnetometer to different positions.

Data Interpretation:

The data collected is analysed to:

- **Visualize the Geomagnetic Field:**
 - Plot the magnetic field components or total intensity as a function of orientation.
 - Compare the results to theoretical or model predictions of the Earth's magnetic field.
- **Identify Sources of Interference:**
 - Determine which devices produce the strongest magnetic interference.
 - Characterize their magnetic behaviour (e.g., field strength, distance dependence, and anisotropy).

Applications and Significance

This experiment has several practical implications:

- **Geomagnetic Studies:** Accurate measurements of the Earth's magnetic field are crucial for navigation, geophysics, and space weather monitoring.
- **Electromagnetic Compatibility (EMC):** Understanding the magnetic interference from devices is essential for designing systems with minimal electromagnetic noise.
- **Device Safety:** Ensures that nearby equipment does not interfere with sensitive magnetic instruments or systems (e.g., MRI machines, compasses, or navigation systems).
 - Multiple readings are taken with the device in different positions and orientations relative to the magnetometer.

4.2.1. Experiment-1:

To get the magnetic field value of the geomagnetic field from Magnetometer and determine the external magnetic field due to nearby device.

Here are the steps followed for the experiment: -

1. **Setup of Equipment:** A laptop running the H-Guide Software (the user interface for the HG-1020 IMU Sensor) was used. The IMU sensor was placed at the centre of a turntable inside a Helmholtz Cage to ensure controlled magnetic field conditions.
2. **Live Data Collection:** The laptop was initially placed directly on the turntable to receive a live feed of data from the IMU sensor.
3. **Measurement with Laptop on Turntable:** The magnetic field was measured using the IMU sensor while the laptop was kept on the turntable.
4. **Measurement without Laptop on Turntable:** The laptop was then moved away from the turntable to a sufficient distance to minimize its magnetic influence. The magnetic field was measured again under the same conditions.
5. **Calculating the Magnetic Field Difference:** The difference between the two magnetic field measurements (with and without the laptop) was calculated. This difference represents the magnetic influence of the laptop.

The total magnetic field: $B_{\text{Total}} = B_{\text{Measured}} - B_{\text{Laptop}}$

6. **Determining the Actual Magnetic Field:** The actual magnetic field at the central position of the turntable was obtained by subtracting the laptop's influence from the measurement taken with the laptop present.

This systematic approach ensures an accurate determination of the magnetic field at the turntable's central position while accounting for the influence of external devices like the laptop. The below table (table 8) shows **the average value from the data.**

Magnetic Field in X (milli-gauss)	Magnetic Field in Y (milli-gauss)	Magnetic Field in Z (milli-gauss)
With Laptop's magnetic field:		
58.02496366	687.5292328	103.2839577
Without Laptop's magnetic field:		
661.2469361	595.5102235	-258.9312184
Laptop's magnetic field:		
603.22197244	-92.0190093	362.2151761

Table 8: To show the average value from the data

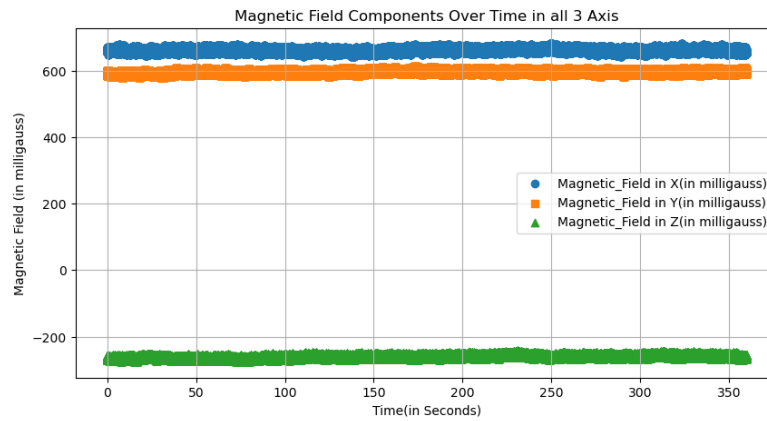


Figure 13: Plot of magnetic field in presence of laptop

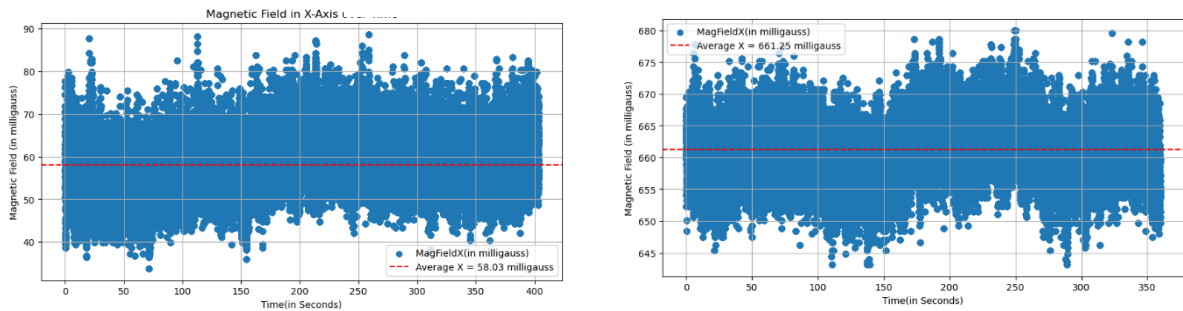


Figure 12: Plot of magnetic field in X-Axis over Time (a) Without Laptop (Left) (b) With Laptop (Right)

Results: - The magnetic field of was found to be **603.22197244**, **-92.0190093**, **362.2151761** in X, Y, Z axis respectively.

4.2.2. Experiment-2:

Experiment to determine the Current (In Amperes) value at which the IMU Value is zero to have a zero magnetic field environment.

Steps for the Experiment:

1. Setup of Helmholtz Cage:

- Place the IMU sensor (HG-1020) at the centre of the Helmholtz Cage, where the field is expected to be most uniform.
- Connect the Helmholtz Cage coils to a power supply with adjustable current control.

2. Initialization of Equipment:

- Ensure the IMU sensor is powered and connected to the laptop running the H-Guide software to monitor magnetic field values in real time.
- Calibrate the IMU sensor to ensure accurate readings by placing it in a zero-field environment (if available).

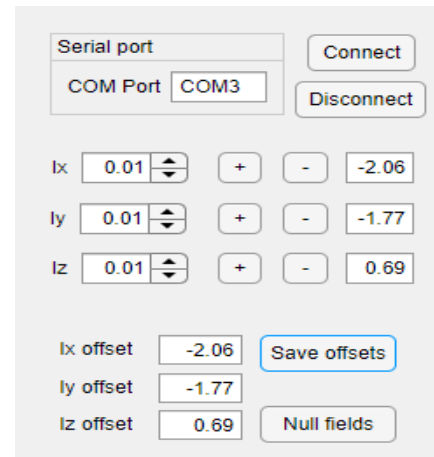


Figure 14: Value Shown on the System Software

3. Baseline Magnetic Field Measurement:

- Measure the ambient magnetic field without any current passing through the Helmholtz Cage.
- Record the magnetic field value components (B_x , B_y , B_z) and the total field magnitude ($|B|$)

4. Gradual Adjustment of Current:

- Begin with a small current (I) through the Helmholtz Cage coils.
- Gradually increase the current in small increments (e.g., 0.1 A or less), and observe the live feed of magnetic field readings from the IMU sensor.
- Note that the field generated by the Helmholtz Cage will oppose the ambient field, reducing the net field at the IMU sensor's location.

<i>Current</i>	<i>Value (in A)</i>
I_x	-2.06
I_y	-1.77
I_z	0.69

Table 9: Value of current for Calibration

5. Zero Magnetic Field Detection:

- Continue adjusting the current until the magnetic field readings from the IMU sensor approach zero (i.e., (B_x , B_y , $B_z \approx 0$ or $|B| \approx 0$)).
- Record the current value (I_0) at which the field nulls out completely or is minimized to the closest detectable level.

6. Verification:

- To confirm the result, slightly increase and decrease the current around I_{zero} to ensure the reading remains consistent and that the field nulls at this specific current value.

7. Repeat for Different Orientations (Optional):

- If necessary, rotate the IMU sensor or adjust the Helmholtz Cage to align with different axes (e.g., x-axis, y-axis, z-axis).
- Repeat the procedure for each orientation to determine if the current varies along different axes due to non-uniform ambient fields.

8. Documentation of Results:

- Document the current value I_{zero} and the corresponding conditions for each axis.
- Note any residual field or variations that may arise due to external influences or experimental limitations.

Outcome: The experiment determines the precise current I_{zero} required to create a zero magnetic field environment at the IMU sensor's location. This value can be used for future experiments that require a null magnetic field setup.

Experiment-2.1	Magnetic Field in X (milli-gauss)	Magnetic Field in Y (milli-gauss)	Magnetic Field in Z (milli-gauss)
	-4.74589	-3.94514	0.739678
Experiment-2.2	Magnetic Field in X (milli-gauss)	Magnetic Field in Y (milli-gauss)	Magnetic Field in Z (milli-gauss)
	3.535257	1.291627	0.855156

Table 10: IMU Calibrated data for two Same Experiments

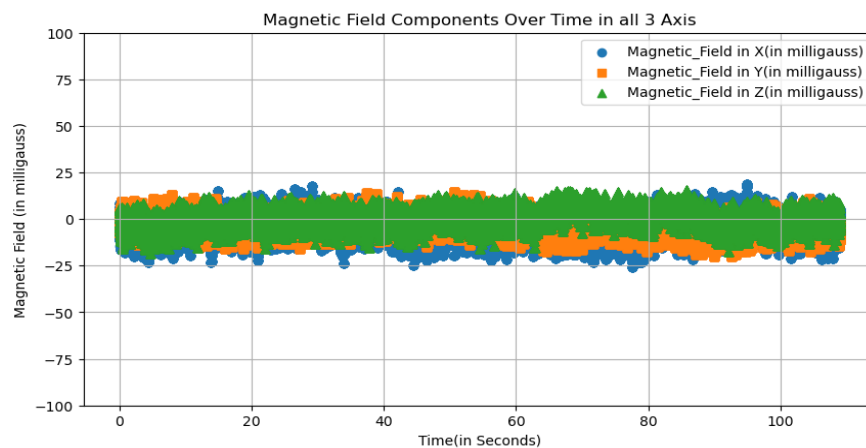


Figure 15: Plot of averaged out data collected from the magnetometer

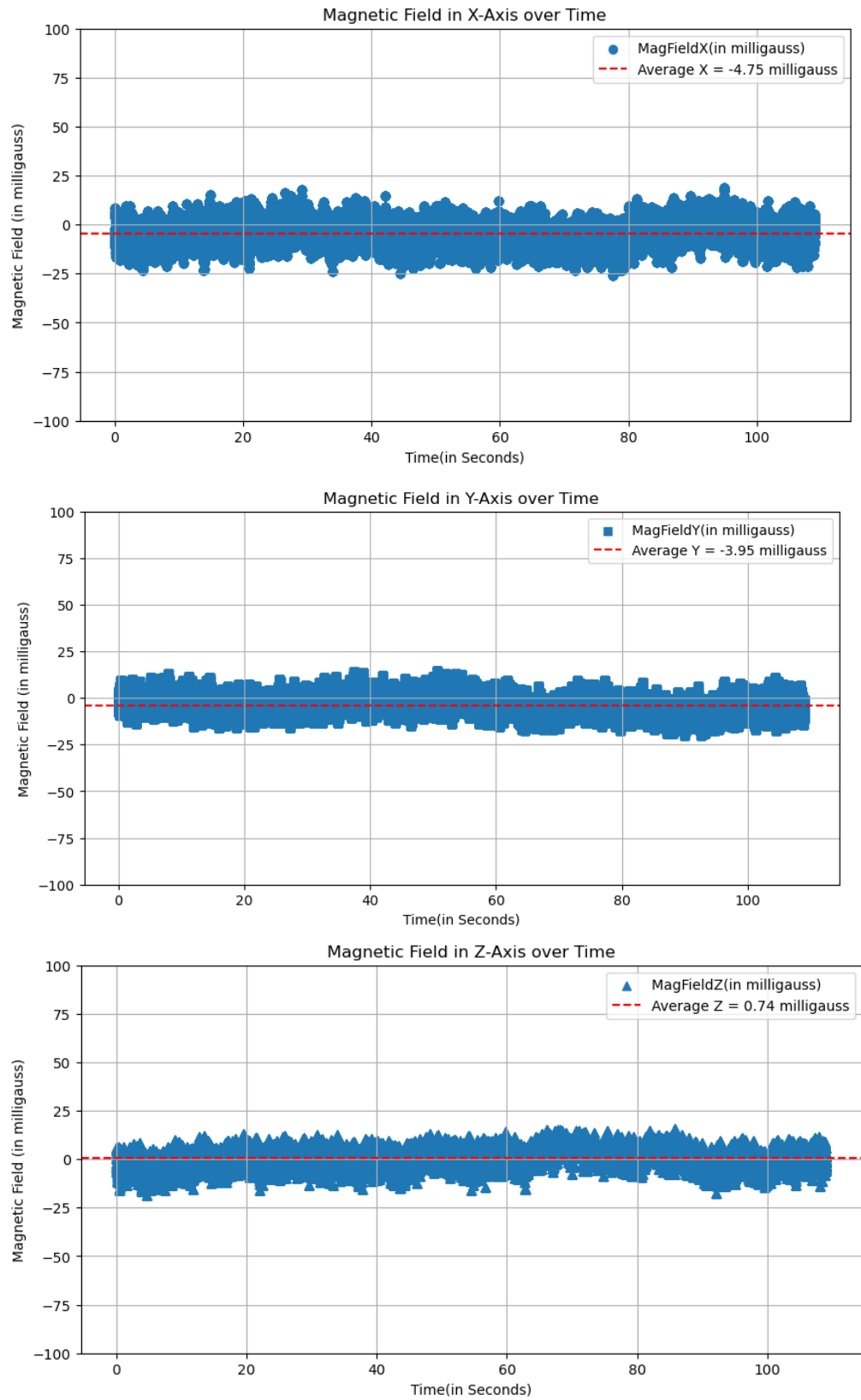


Figure 16: Magnetic field after calibration after in X,Y,Z direction respectively.

4.2.3.Experiment-3:

Experiment to determine the geomagnetic field of the location in the lab and estimate the error due to hard iron effect, soft iron effect and misalignment.

Steps of the Experiment

1. Theoretical Geomagnetic Field Estimation

- **Use of Models:**
 - Calculate the theoretical geomagnetic field at the lab location using established geomagnetic field models: World Magnetic Model (WMM2020), International Geomagnetic Reference Field (IGRF-13)
 - Input the geographic coordinates (latitude, longitude, altitude) of the lab into the models.
 - Obtain the geomagnetic field components B_x , B_y , B_z
- **MATLAB Implementation:**
 - Use MATLAB to implement the mathematical equations of WMM2020 and IGRF-13.
 - Plot the geomagnetic field components to visualize variations at the lab's location.

2. Experimental Geomagnetic Field Measurement

- **Setup the Sensor:**
 - Place the IMU sensor (HG-1020) at a stable and interference-free location in the lab.
 - Ensure the sensor is calibrated to remove initial biases.
- **Data Collection:**
 - Measure the magnetic field (B_x , B_y , B_z) and the total field magnitude ($|B|$) using the IMU sensor.
 - Collect multiple readings to average out transient noise or fluctuations.

3. Comparison of Theoretical and Experimental Values

- Compare the measured experimental values of B with the theoretical values obtained from WMM2020 and IGRF-13.
- Calculate the difference between the theoretical and experimental values for each component and the total magnitude.

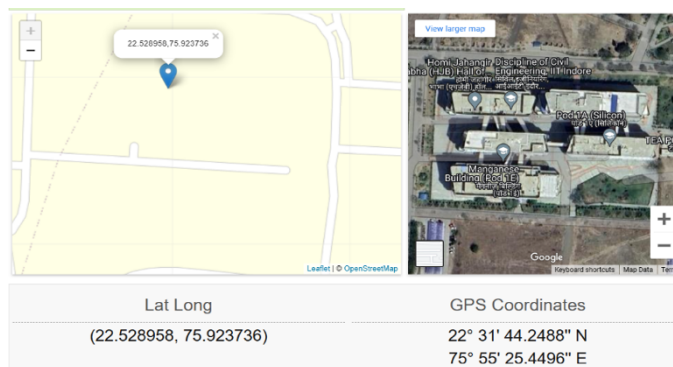
4. Calculate the percentage error for each component and the total field:

- **Hard Iron Effect:**
 - Characterized by a constant offset in the magnetic field readings.
 - Identified by analysing shifts in the field across all orientations.
- **Soft Iron Effect:**
 - Characterized by changes in the measured magnetic field due to surrounding materials.
 - Detected through deviations in field magnitude when the sensor orientation changes.
- **Misalignment:**
 - Errors due to incorrect alignment of the IMU with the coordinate axes.
 - Detected by analysing discrepancies in angular measurements of the field.

5. Documentation and Results

- Tabulate the theoretical and experimental values of B_x , B_y , B_z .
- Report the differences and percentage errors.
- Estimate the relative contribution of hard iron, soft iron, and misalignment effects based on field patterns and deviations.

Outcome: This experiment identifies the combined error in the geomagnetic field measurements due to hard iron, soft iron, and misalignment.



22°31'44" N 75°55'25" E
Simrol, MP
590m Elevation

Figure 17: Latitude and Longitude information of lab location from website (Left) and using mobile GPS (right)

	International Geomagnetic Reference Field (IGRF) in mG	World Magnetic Model (WMM) in mG
X	371.99	371.9
Y	2.1787	2.124
Z	262.86	263.13

Table 11: Comparing the two Models (IGRF-13 AND WMM2020)

4.2.4 Experiment-4:

Experiment to compare the B Vs I plot for both experimental and theoretical value.

Steps for the Experiment

1. Data Collection:

For each current value from $I = 0.1$ A to $I = 2.0$ A (step size = 0.1 A), collect 5000 readings of the magnetic field B using the magnetometer.

Average out the 5000 readings for each current value to reduce noise.

	IGRF (in mG)	(WMM) (in mG)	Laboratory Result (in mG)	Error
X	371.99	371.9	661.247	289.347
Y	2.177	2.124	595.510	593.396
Z	262.86	263.13	-258.931	521.791

Table 12: Detailed comparison of geomagnetic field with results

2. Data Processing:

- Subtract the B value $I = 0$ A from the B value corresponding to $I = 0.1$ A to remove any offset or baseline magnetic field.
- Repeat this process for subsequent current values:
 - For $I = 0.2$ A subtract the B value for $I = 0.1$ A, and so on.
- Add the reading from the current step to the adjacent reading to ensure a smooth transition in the data.

3. Theoretical Data:

- Measure the physical parameters of the Helmholtz coil system:

$$B_{value} = 7.792 \frac{14 \mu_0 N I_{Each\ axis}}{(1 + \gamma) \pi \sqrt{2 + \gamma} \cdot a}$$

- b: Distance between the coils.
- a: Half-length of one side of the coil (radius for circular Helmholtz coils).
- N: Number of turns in each coil.
- Calculate the parameter, which is given as

$$\gamma = \frac{b}{a}$$

- Use this parameter in the Helmholtz coil equation to compute the theoretical magnetic field for each current step.

4. Comparison:

- Compare the processed experimental values with the theoretical values for all current steps $I = 0.1 \text{ A}$ to $I = 2.0 \text{ A}$
- Plot the B Vs I graph for both theoretical and experimental data.
- Analyse the differences and quantify errors.

5. Analysis of Deviations

- **Potential Causes of Deviations:**
 - **Hard Iron and Soft Iron Effects:** Magnetic distortions caused by surrounding materials.
 - **Coil Imperfections:** Deviations due to irregularities in the winding or non-ideal coil geometry.
 - **Alignment Errors:** Misalignment of the magnetometer with the coil axis.
 - **Environmental Noise:** External magnetic fields affecting the experimental readings.
- **Interpret Results:**
 - Identify regions where experimental data deviates significantly from theoretical predictions.

- Attribute deviations to specific sources based on trends (e.g., linear vs. nonlinear errors).

Outcomes

The experiment produces:

1. A B vs I plot comparing experimental and theoretical magnetic field values.
2. A quantitative error analysis highlighting the discrepancies between theory and experiment.
3. Insights into potential improvements for reducing measurement errors in future experiments.

Experimental and Theoretical Validation

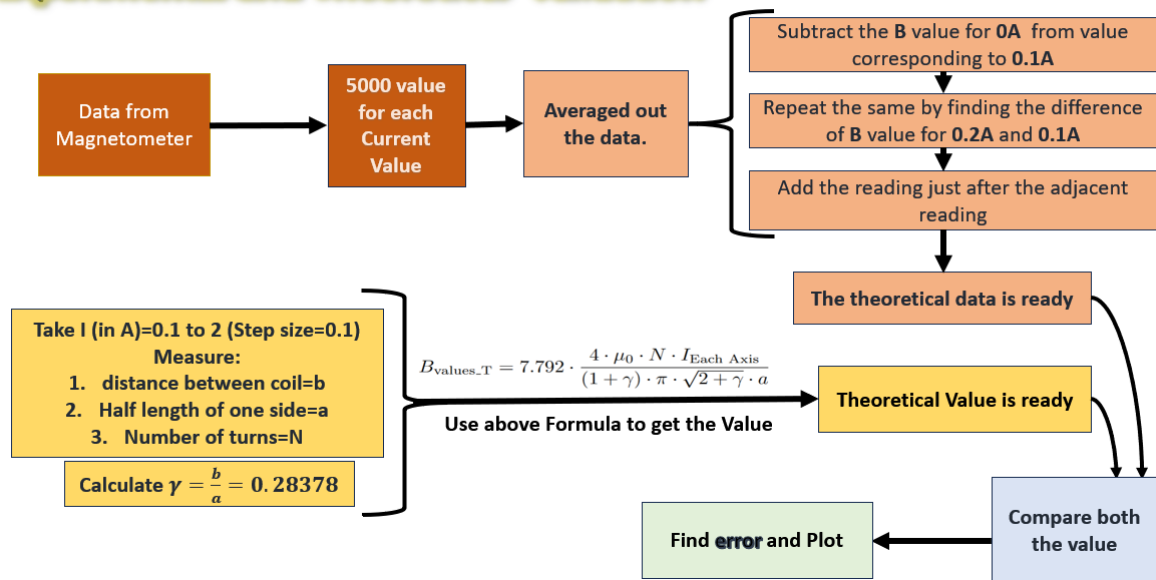


Figure 18: Flowchart showing the steps taken for the experimentations

	Current (in A)	Theoretical B _x (in mG)	Experimental B _x (in mG)	Error (in mG)	Error (%)
1	0.1000	32.5078	32.1280	-0.3798	-1.1820
2	0.2000	65.0155	64.1340	-0.8815	-1.3745
3	0.3000	97.5233	95.8240	-1.6993	-1.7733
4	0.4000	130.0310	124.7590	-5.2720	-4.2258
5	0.5000	162.5388	154.9620	-7.5768	-4.8894
6	0.6000	195.0465	190.0270	-5.0195	-2.6415
7	0.7000	227.5543	221.6950	-5.8593	-2.6429
8	0.8000	260.0620	252.8970	-7.1650	-2.8332
9	0.9000	292.5698	287.9870	-4.5828	-1.5913
10	1	325.0775	329.8460	4.7685	1.4457
11	1.1000	357.5853	353.7280	-3.8573	-1.0905
12	1.2000	390.0931	389.9280	-0.1651	-0.0423
13	1.3000	422.6008	423.6450	1.0442	0.2465
14	1.4000	455.1086	449.4220	-5.6866	-1.2653
15	1.5000	487.6163	479.4510	-8.1653	-1.7031
16	1.6000	520.1241	508.8740	-11.2501	-2.2108
17	1.7000	552.6318	540.0940	-12.5378	-2.3214
18	1.8000	585.1396	566.8670	-18.2726	-3.2234
19	1.9000	617.6473	595.2120	-22.4353	-3.7693
20	2	650.1551	625.3230	-24.8321	-3.9711

Table 13: Theoretical and Experimental Values with Error and error percentage for X-Axis

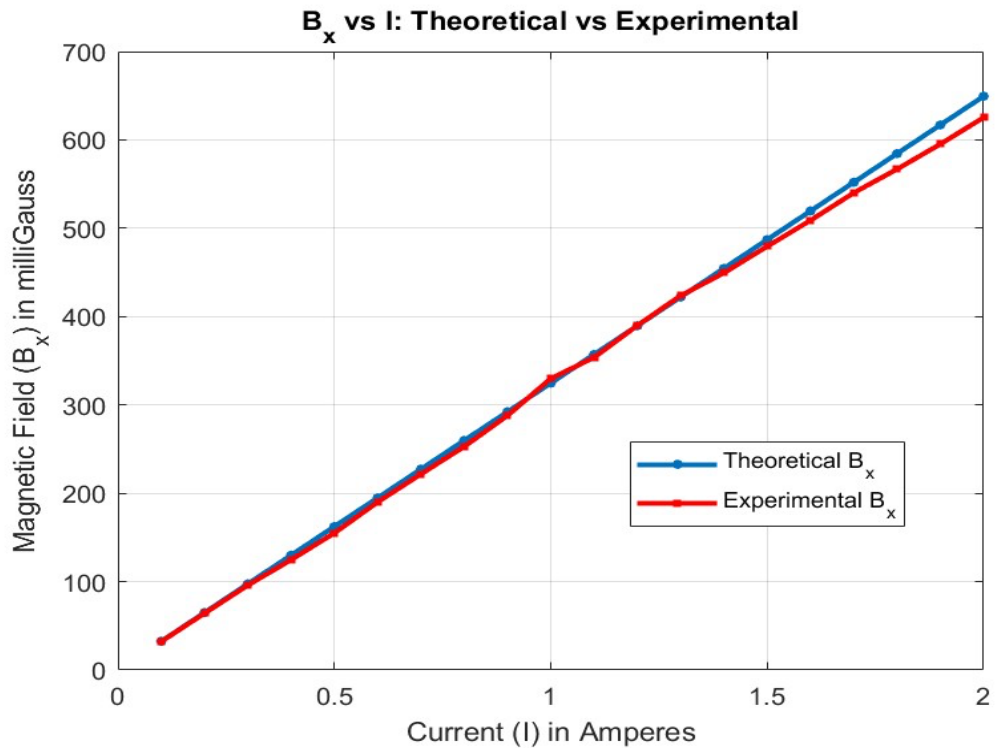


Figure 19: Plot of theoretical and experimental magnetic field value in X-Axis

	Current (in A)	Theoretical B_y (in mG)	Experimental B_y (in mG)	Error (in mG)	Error (%)
1	0.1000	32.5078	30.9430	-1.5648	-5.0569
2	0.2000	65.0155	62.0330	-2.9825	-4.8079
3	0.3000	97.5233	97.3360	-0.1873	-0.1924
4	0.4000	130.0310	129.2780	-0.7530	-0.5825
5	0.5000	162.5388	163.1580	0.6192	0.3795
6	0.6000	195.0465	196.7440	1.6975	0.8628
7	0.7000	227.5543	227.9720	0.4177	0.1832
8	0.8000	260.0620	261.7410	1.6790	0.6415
9	0.9000	292.5698	296.9780	4.4082	1.4844
10	1	325.0775	333.3780	8.3005	2.4898
11	1.1000	357.5853	365.8340	8.2487	2.2548
12	1.2000	390.0931	396.6990	6.6059	1.6652
13	1.3000	422.6008	429.6020	7.0012	1.6297
14	1.4000	455.1086	462.8410	7.7324	1.6706
15	1.5000	487.6163	494.6420	7.0257	1.4204
16	1.6000	520.1241	526.9050	6.7809	1.2869
17	1.7000	552.6318	560.5070	7.8752	1.4050
18	1.8000	585.1396	593.7630	8.6234	1.4523
19	1.9000	617.6473	632.6880	15.0407	2.3773
20	2	650.1551	667.3470	17.1919	2.5762

Table 14: Theoretical and Experimental Values with Error and error percentage for Y-Axis

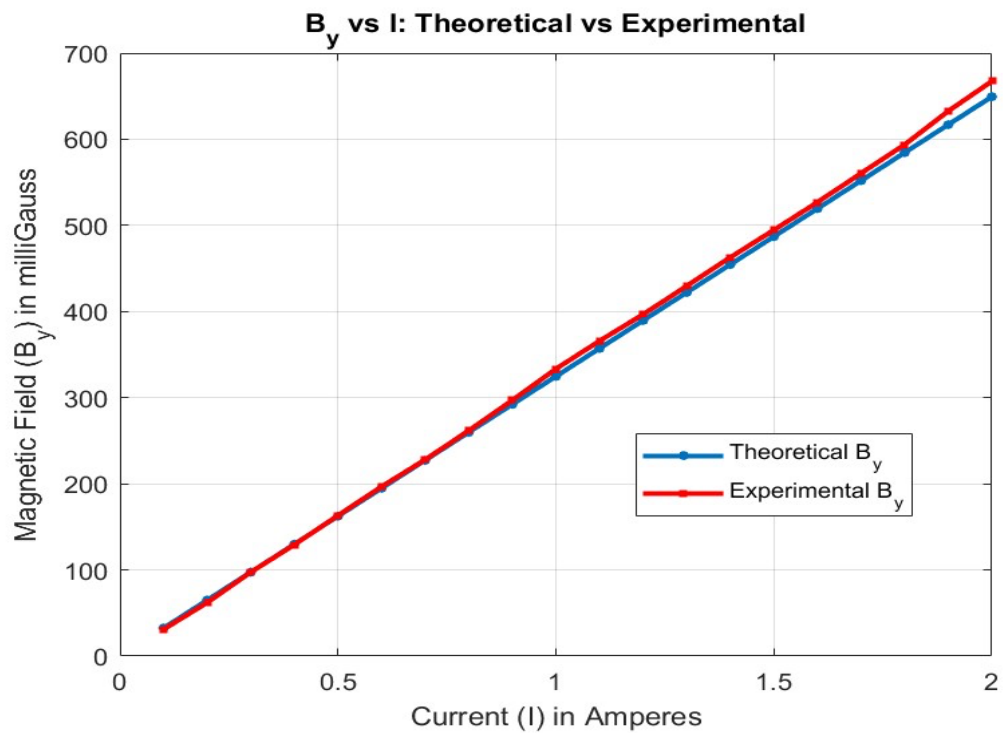


Figure 20: Plot of theoretical and experimental magnetic field value in Y-Axis

	Current (in A)	Theoretical B _z (in mG)	Experimental B _z (in mG)	Error (in mG)	Error (%)
1	0.1000	32.5078	37.7330	5.2252	13.8479
2	0.2000	65.0155	67.5130	2.4975	3.6993
3	0.3000	97.5233	105.6830	8.1597	7.7210
4	0.4000	130.0310	139.9650	9.9340	7.0975
5	0.5000	162.5388	173.3070	10.7682	6.2134
6	0.6000	195.0465	207.1580	12.1115	5.8465
7	0.7000	227.5543	237.8490	10.2947	4.3283
8	0.8000	260.0620	270.1360	10.0740	3.7292
9	0.9000	292.5698	305.6680	13.0982	4.2851
10	1	325.0775	335.9680	10.8905	3.2415
11	1.1000	357.5853	359.7170	2.1317	0.5926
12	1.2000	390.0931	382.1340	-7.9591	-2.0828
13	1.3000	422.6008	417.2170	-5.3838	-1.2904
14	1.4000	455.1086	452.6040	-2.5046	-0.5534
15	1.5000	487.6163	487.3140	-0.3023	-0.0620
16	1.6000	520.1241	519.2460	-0.8781	-0.1691
17	1.7000	552.6318	552.5440	-0.0878	-0.0159
18	1.8000	585.1396	588.2520	3.1124	0.5291
19	1.9000	617.6473	618.5150	0.8677	0.1403
20	2	650.1551	648.5720	-1.5831	-0.2441

Table 15: Theoretical and Experimental Values with Error and error percentage for Z-Axis

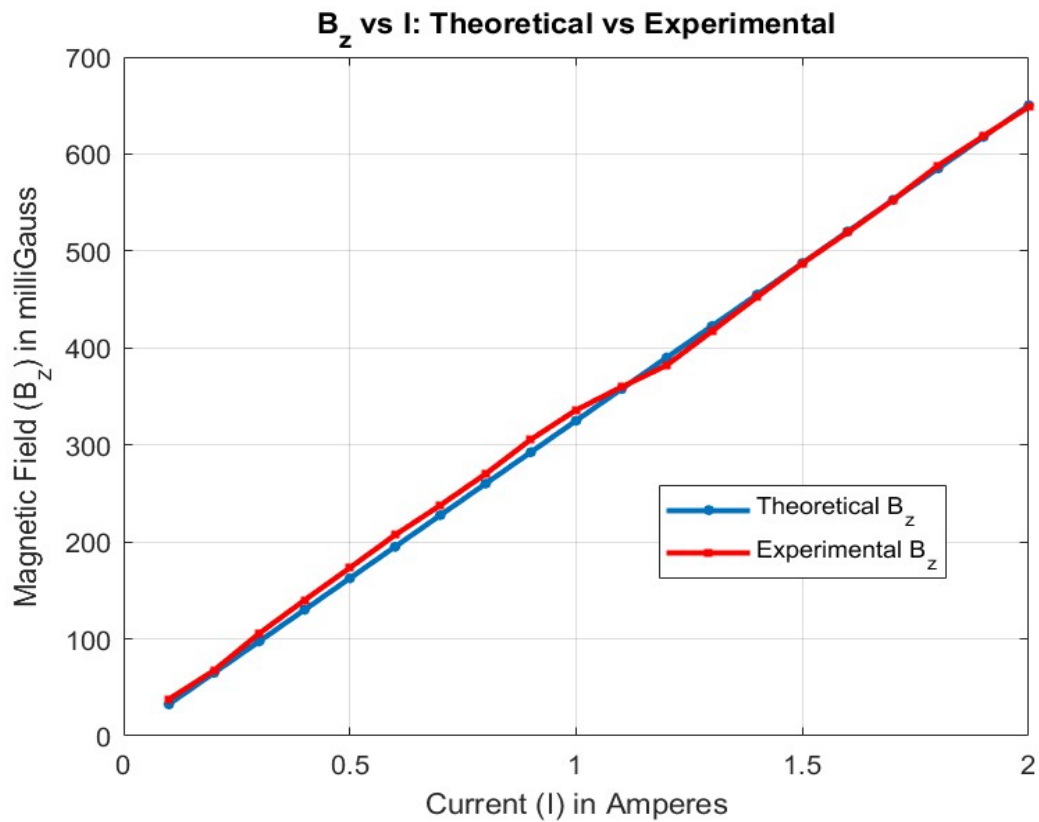


Figure 21: Plot of theoretical and experimental magnetic field value in Z-Axis

I (in A)	Experimental Bx(in mG)	Experimental By (in mG)	Experimental Bz (in mG)
0.1	32.128	30.943	37.733
0.2	64.134	62.033	67.513
0.3	95.824	97.336	105.68
0.4	124.76	129.28	139.97
0.5	154.96	163.16	173.31
0.6	190.03	196.74	207.16
0.7	221.69	227.97	237.85
0.8	252.9	261.74	270.14
0.9	287.99	296.98	305.67
1	329.85	333.38	335.97
1.1	353.73	365.83	359.72
1.2	389.93	396.7	382.13
1.3	423.64	429.6	417.22
1.4	449.42	462.84	452.6
1.5	479.45	494.64	487.31
1.6	508.87	526.9	519.25
1.7	540.09	560.51	552.54
1.8	566.87	593.76	588.25
1.9	595.21	632.69	618.51
2	625.32	667.35	648.57

Table 16: Table of theoretical and experimental magnetic field value in all 3 -Axis

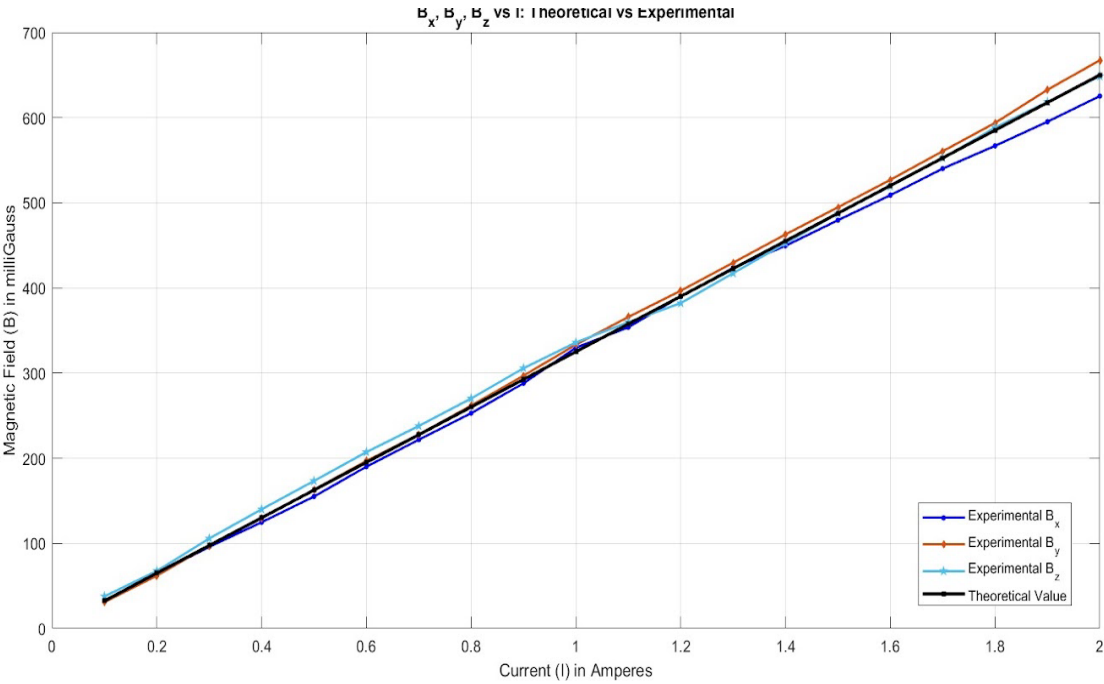


Figure 22 : Plot of theoretical and experimental magnetic field value in all 3 -Axis

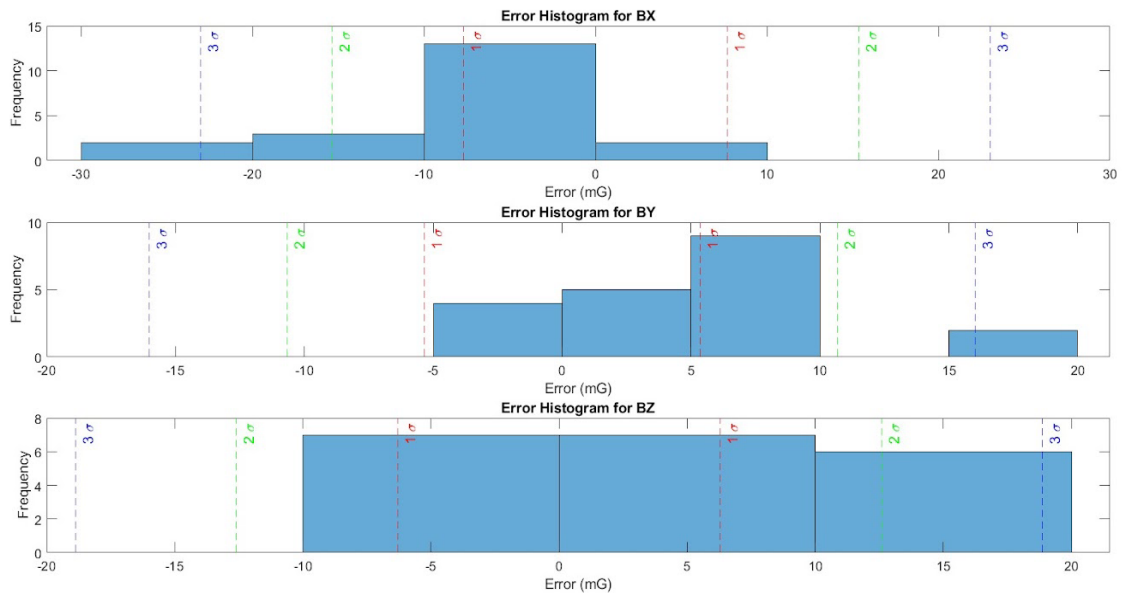


Figure 23: Error histograms

Chapter 5: Implementation

5.1 Basics

5.1.1. Orbital Parameter

1. Semi-Major Axis (a)

Definition: The average distance between the orbiting object and the central body.

Significance: Defines the size of the orbit. For elliptical orbits, it is the longest axis of the ellipse.

2. Eccentricity (e)

Definition: A measure of the orbit's deviation from a perfect circle.

Range:

Elliptical orbit: $0 < e < 1$:

Circular orbit: $e = 0$:

Parabolic trajectory: $e = 1$

Hyperbolic trajectory: $e > 1$

Significance: Determines the shape of the orbit.

3. Inclination (i)

Definition: The tilt of the orbital plane relative to a reference plane (usually the equatorial plane or ecliptic plane).

Range: 0° to 180°

Classification type:

Prograde orbit in the reference plane: $i = 0^\circ$

Polar orbit $i = 90^\circ$

Retrograde orbit $i > 90^\circ$

4. Longitude of the Ascending Node (Ω)

Definition: The angle measured in the reference plane from a fixed direction (such as the vernal equinox) to the ascending node (where the orbit crosses the reference plane from South to North).

Range:

Significance: Specifies the orientation of the orbital plane in space.

5. Argument of Periapsis (ω)

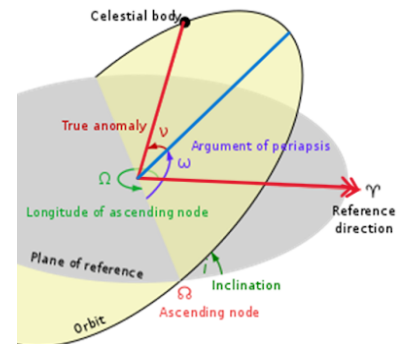


Figure 24: Six Orbital Parameter

Definition: The angle within the orbital plane from the ascending node to the periapsis (the closest point to the central body).

Range: 0^0 to 360^0

Significance: Defines the orientation of the orbit within its plane.

6. True Anomaly (ν)

Definition: The angle between the periapsis and the current position of the orbiting object, measured at the central body.

Range: 0^0 to 360^0

Significance: Specifies the position of the orbiting object along its orbit at a specific time.

Orbital Element	Description
a Semi-Major Axis	Defines the size of the orbit.
e Eccentricity	Defines the shape of the orbit.
i Inclination	Defines the tilt of the orbital plane.
Ω Longitude of Ascending Node	Orientation of the orbital plane in space.
ω Argument of Periapsis	Orientation of the orbit within its plane.
ν True Anomaly	Current position of the object along its orbit.

Table 17: Summery of all 6 Orbital Parameters

5 1.2. Simulation work flow

Here's a step-by-step breakdown in the requested style:

1. User Input for Orbit Selection

- First, the user was prompted to select the type of orbit (circular or elliptical).
- For a circular orbit, the user provided the orbit radius and inclination angle.
- For an elliptical orbit, the apogee, perigee, and inclination angle were entered.
- Based on the inputs, the type of orbit was decided.

2. Constants Initialization

- The radius of Earth ($R_e = 6371 \text{ km}$) was set as a constant, along with the number of points to be generated ($\text{numPoints} = 1000$).
- These constants were used to calculate the orbital trajectory later.

3. Generate Points Along the Orbit

Next, points along the orbit were generated:

- For the circular orbit, 1000 equally spaced angles (‘theta’) were generated. Using these angles, the ‘(x, y, z)’ coordinates for the circular orbit were calculated in 3D space.
- For the elliptical orbit, the semi-major axis (‘a’) and eccentricity (‘e’) were calculated. Using the orbital equation, the points were computed in polar form and then converted to Cartesian (x, y, z).

This gave us the 3D Cartesian coordinates of the orbit.

4. Apply Inclination

- The inclination of the orbit was applied by rotating the orbit’s coordinates about the x-axis using a rotation matrix.
- After this step, the orbit was tilted by the given inclination angle, and the 3D trajectory now matched the desired orientation in space.

5. Rotations

i. Rotation about the Z-axis by Longitude of the Ascending Node (Ω):

$$R_{\Omega} = \begin{pmatrix} \cos \Omega & -\sin \Omega & 0 \\ \sin \Omega & \cos \Omega & 0 \\ 0 & 0 & 1 \end{pmatrix}$$

- **Purpose:** This rotation aligns the ascending node of the orbit with the reference direction (typically the vernal equinox).

ii. Rotation about the X-axis by Inclination (i):

$$R_i = \begin{pmatrix} 1 & 0 & 0 \\ 0 & \cos i & -\sin i \\ 0 & \sin i & \cos i \end{pmatrix}$$

- **Purpose:** *This rotation tilts the orbital plane by the inclination angle i relative to the equatorial plane.*

iii. Rotation about the Z-axis by Argument of Periapsis (ω):

$$R_{\omega} = \begin{pmatrix} \cos \omega & -\sin \omega & 0 \\ \sin \omega & \cos \omega & 0 \\ 0 & 0 & 1 \end{pmatrix}$$

Purpose: This rotation positions the periapsis within the orbital plane.

Combined Transformation:

To transform the orbital coordinates [x, y, z] in the orbital plane to the inertial frame, the three matrices are multiplied in sequence:

$$R_{total} = R_{\Omega} \cdot R_i \cdot R_{\omega}$$

6. Calculate Distance and Height

- The distance of each point from the center of the Earth was calculated using the formula for Euclidean distance.
- The height of the satellite above Earth's surface was then obtained by subtracting the Earth's radius (R_e) from these distances.
- This gave us the height of the satellite at all 1000 points along the orbit.

7. Convert Cartesian to Geodetic Coordinates

- The Cartesian coordinates (x, y, z) were converted to geodetic coordinates (latitude, longitude, and height) using the ``ecef2lla`` function.
- This step provided the subsatellite points in terms of geodetic latitude, longitude, and altitude.

8. Create Tabular Data for Subsattellite Points

- A table was created to display the subsatellite points, showing:
- Point number, latitude, longitude, and height above Earth's surface.
- This gave a clear overview of the ground track of the orbit.

9. Magnetic Field Calculation (IGRF and WMM Models)

- For each point along the orbit, the magnetic field components (B_X , B_Y , B_Z) were calculated using both the IGRF and WMM models.
- The magnetic field values, originally in nanotesla (nT), were converted to milligauss (mG).
- These values were stored in a new table for comparison between the two models.

10. Plot Magnetic Field Components

- The magnetic field components (B_X , B_Y , B_Z) were plotted against the height of the satellite.
- Separate plots for the IGRF and WMM models were created, showing how the magnetic field varied with altitude.
- This gave a detailed visualization of the magnetic field along the orbit.

2. 3D Plot of the Orbit Trajectory

- A 3D plot was created to visualize the orbit trajectory.
- The Earth was represented as a sphere using the ``surf`` function.
- The orbit trajectory was overlaid using ``plot3``.
- The view was enhanced with appropriate axis labels, grid lines, and lighting for better clarity.

- This provided a clear depiction of the satellite's motion around Earth in 3D space.

3. Combine Magnetic Field Components

- Combined plots were created to compare the magnetic field components ('BX', 'BY', 'BZ') for both the IGRF and WMM models.
- This allowed a side-by-side analysis of the two models, highlighting any differences in their results.

4. Highlight Maximum and Minimum Values

- The maximum and minimum values of each magnetic field component were calculated and displayed in a summary table.
- This provided a concise view of the extreme values of the magnetic field along the orbit.

Results and Final Output

At the end of the script, the tables and plots showing subsatellite points and magnetic field values were displayed. Plots of magnetic field components versus height and orbit trajectory in 3D space were presented.

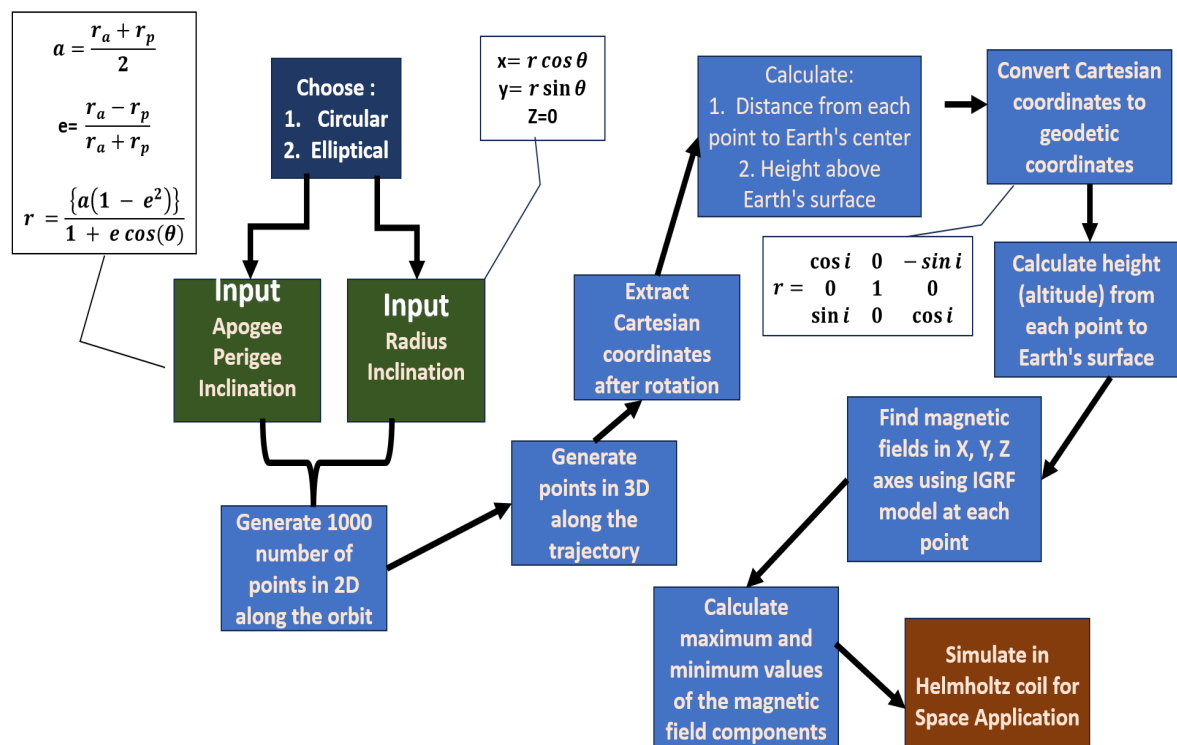


Figure 25: Application Root Map with proper Steps

```

Enter 1 for circular orbit, 2 for elliptical orbit: 2
Enter the apogee of the elliptical orbit (km): 10978
Enter the perigee of the elliptical orbit (km): 6960
Enter the inclination of the elliptical orbit (degrees): 30
Enter the Longitude of the Ascending Node ( $\Omega$ ) (degrees): 11
Enter the Argument of Periapsis ( $\omega$ ) (degrees): 9
Enter the True Anomaly ( $v$ ) (degrees): 12.5

```

Figure 26: Input parameters of the Simulation

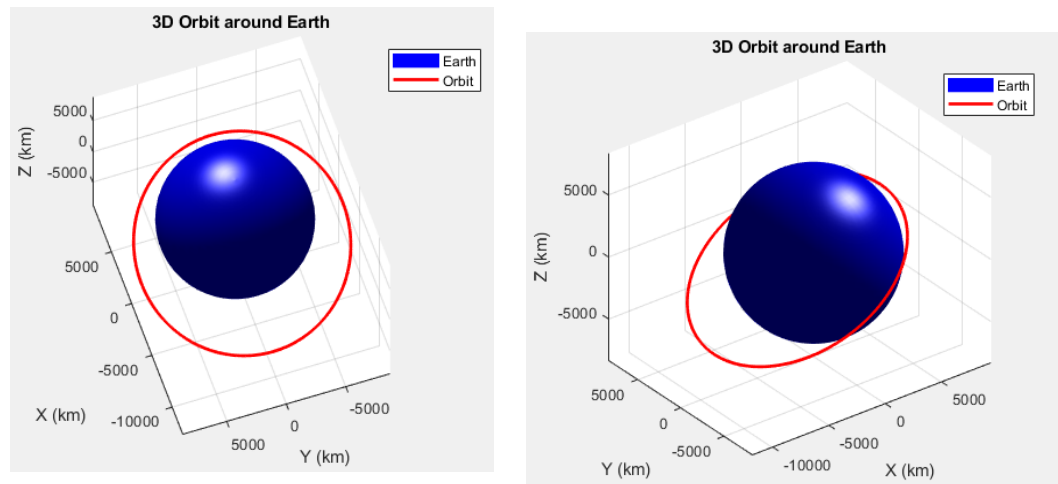


Figure 27: 3D Orbit that is generated from the data given Input parameter

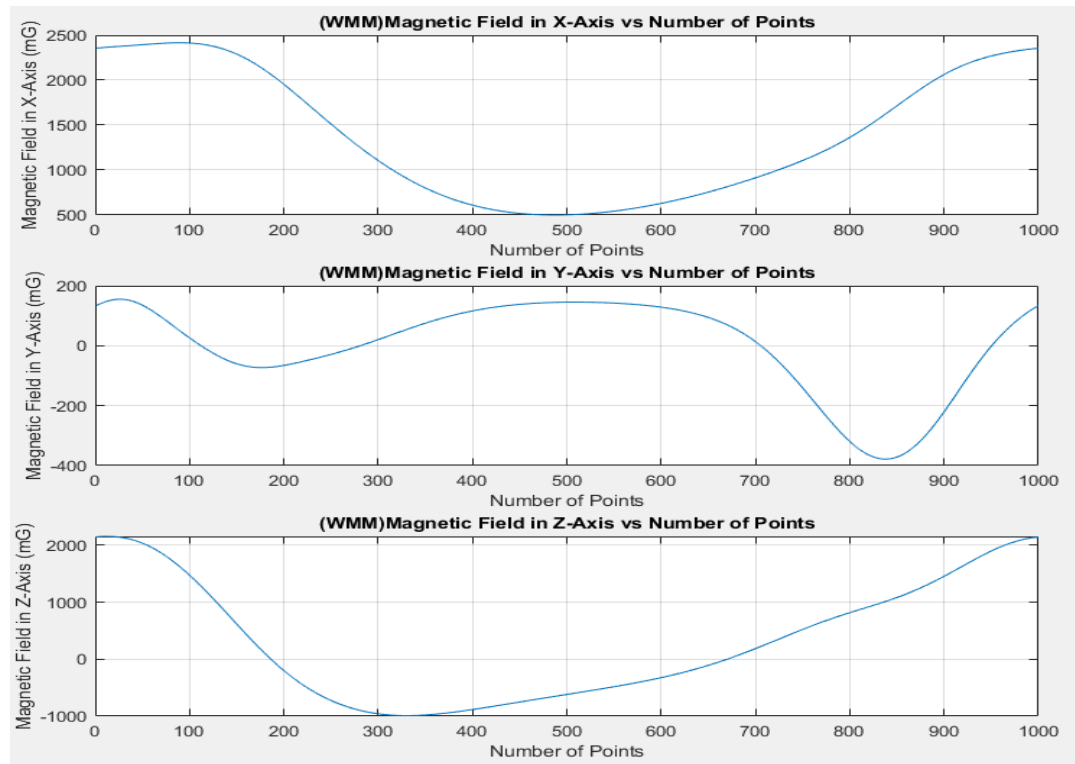


Figure 28: Magnetic field form WMM model in X, Y and Z direction Vs Number of points taken

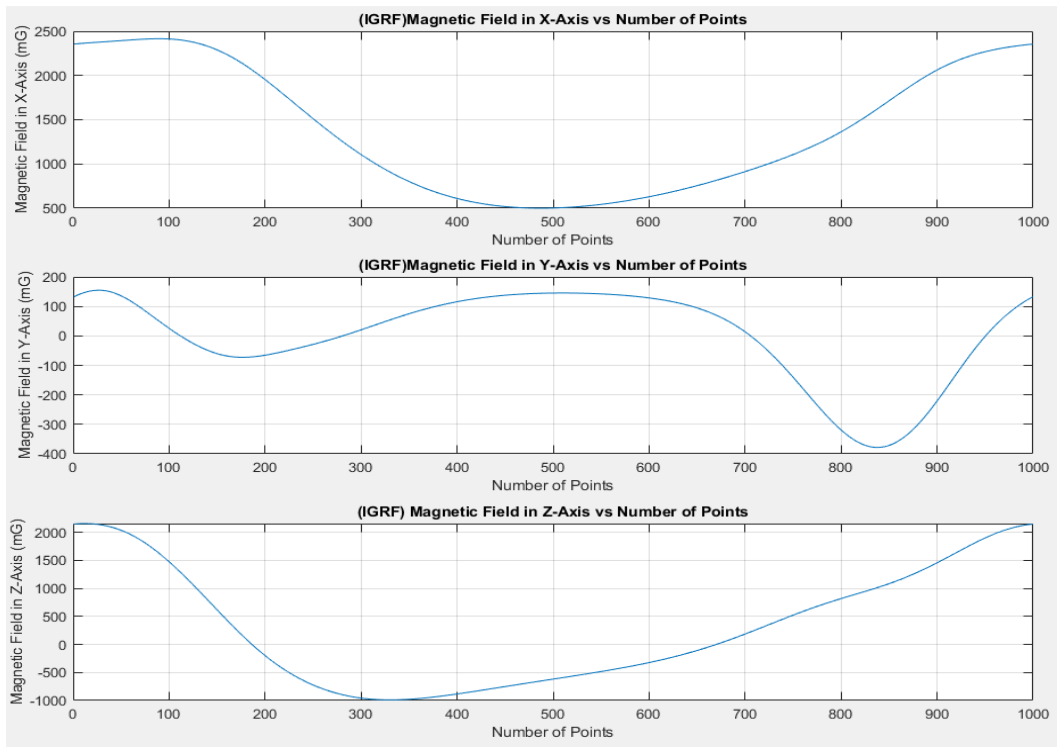


Figure 29: Magnetic field form IGRF model in X, Y and Z direction Vs Number of points taken

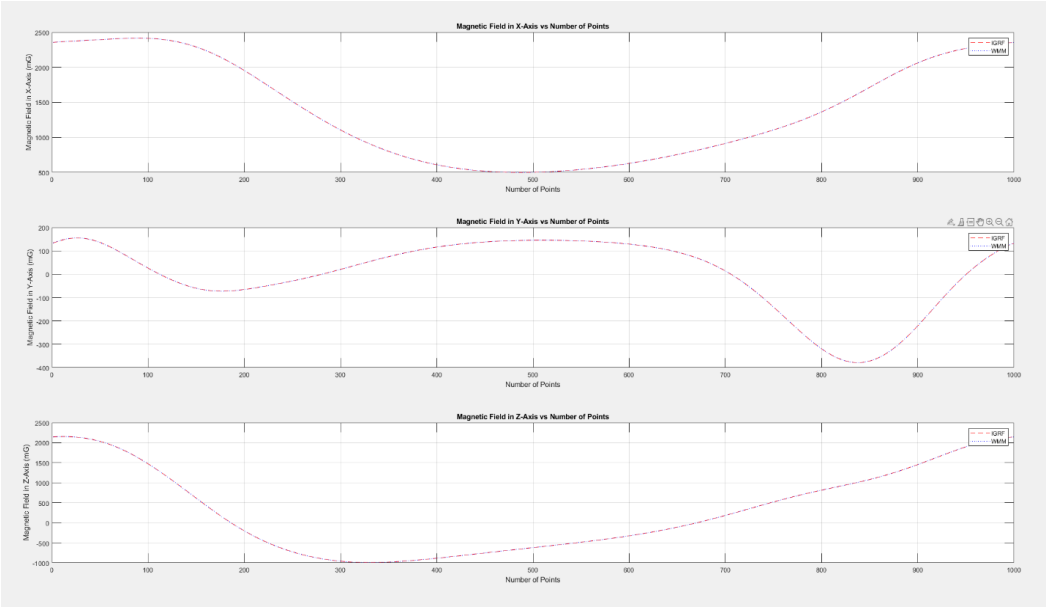


Figure 30: Magnetic field form both WMM and IGRF model in X, Y and Z direction Vs Number of points taken

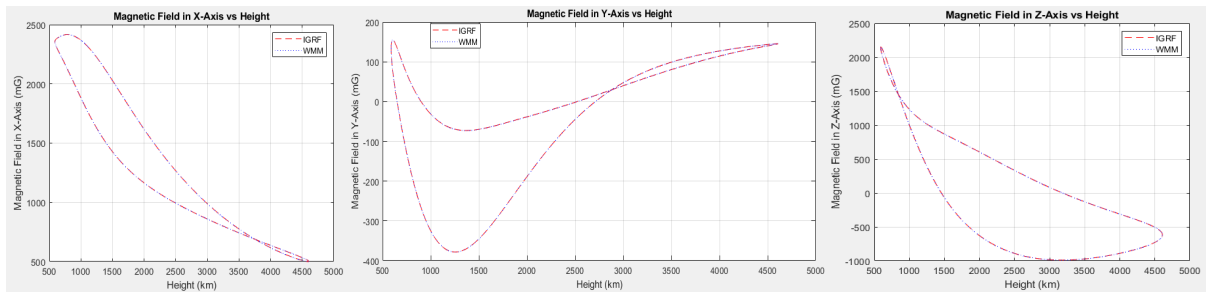


Figure 34: Magnetic Field in X, Y and Z Axis Vs Height for WMM and IGRF Model

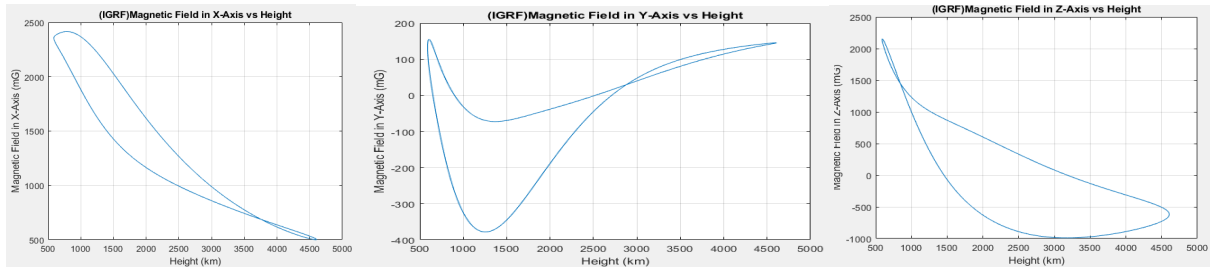


Figure 33: Magnetic Field in X, Y and Z Axis Vs Height for IGRF Model

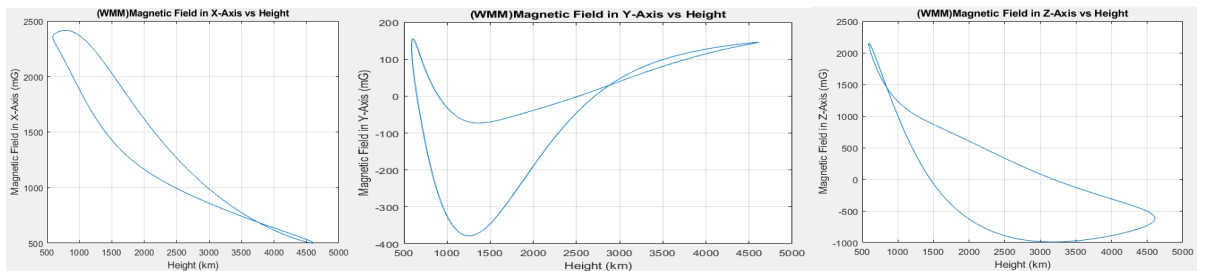


Figure 32: Magnetic Field in X, Y and Z Axis Vs Height for WMM Model

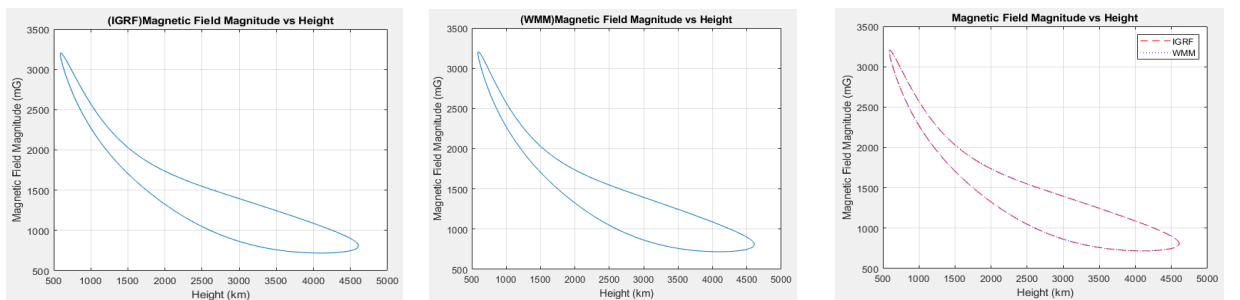


Figure 31: Magnetic Field in X, Y and Z Axis Vs Height for WMM and combined model of IGRF Model

Chapter 6: Gyro Rate Bias Estimation

Magnetic heading refers to the direction an object points relative to Earth's magnetic north, determined by magnetometer measurements of the Earth's magnetic field at specific altitudes, latitudes, and longitudes. This magnetic heading, or yaw angle, is derived from the horizontal components (H_0) of the magnetic field. Concurrently, gyroscopes measure the rate of rotation (angular velocity) around an axis but often exhibit bias, a constant error that must be estimated and corrected for precise measurements. Gyro rate bias estimation utilizes a Measurement Model and Bias Estimation through the Kalman Filter. The process involves calculating the magnetic field vector, computing the heading from magnetic field components, and estimating gyro bias using Kalman filtering. By integrating these steps, reliable and accurate heading estimation is achieved while compensating for biases in gyroscope readings, enhancing the performance of navigation and orientation systems. This combined approach is essential for applications such as navigation and orientation tracking in mobile devices, drones, and other systems requiring accurate heading and rotation information.

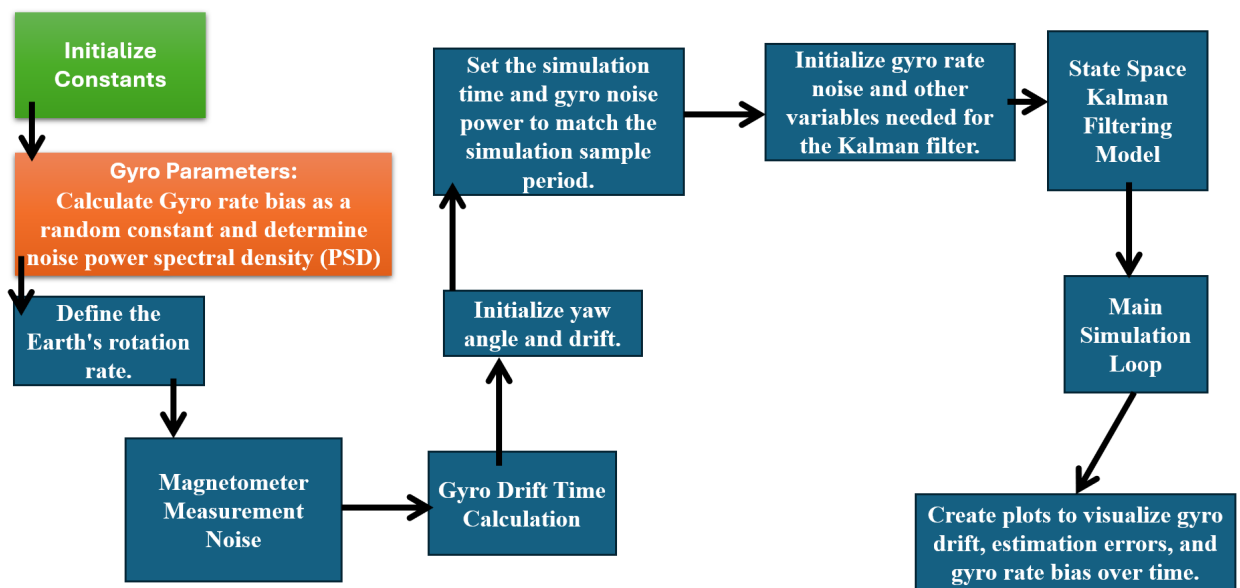


Figure 35: Flowchart Depicting the estimation by minimizing error

Magnetometer Measurement Noise

Magnetometer measurement is (Strapdown), in the body frame:

$$\tilde{m}_m^b = b_m + (I_3 + M_m)C_n^b(m_E^n + m_A^n) + w_m$$

Measured Value
Bias
Scale Factor
Geomagnetic
Surrounding Anomaly
Noise

$C_n^b \rightarrow$ From navigation frame to Body frame

Magnetic Heading from Magnetic field:

From the figure:

$$\tilde{\psi}_{mb} = \tan^{-1} \frac{\tilde{m}_{my}^b}{\tilde{m}_{mx}^b}$$

$$B_H \cos \psi_{mb} = B_x^b$$

$$B_H \cos \psi_{mb} = -B_y^b$$

Calibration Determines b_m , M_m , m_A^n to be rejected through abnormal residual screening.

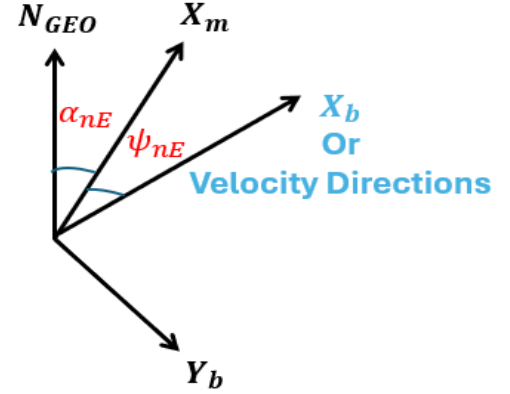


Figure 36: Diagram showing Direction of Spacecraft with respect to Heading Angle and angle of ideclination

Yaw Heading measurement from Magnetic Heading:

We assume that the magnetometer is calibrated and the measurements are with the calibrated magnetometer.

Assume that there is no local surrounding mag. Field, and if they suddenly appear in the measurement they will be rejected as bad measurement.

$$\tilde{\psi}_{nb} = \tilde{\psi}_{mb} + \alpha_{nE} = \psi_{nb} + W_\psi$$

$$\text{Measurement Residue} = \tilde{\psi}_{nb} - \hat{\psi}_{nb}$$

ψ_{nb} is the true heading angle

$\hat{\psi}_{nb}$ is the estimate of True heading angle

Magnetometer Heading Measurement Model:

$$\text{Magnetic Heading} = \tilde{\psi}_{mb} + \alpha_{nE} = \psi_{nb} + W_\psi$$

$$\tilde{m}_{xb} = m_{xb} + w_m = m_H C \psi_{mb} + w_m$$

$$\tilde{m}_{yb} = m_H S \psi_{mb} + w_m$$

$$\psi_{mb} = \tan^{-1} \frac{-m_{yb}}{m_{xb}}$$

$$\tilde{\psi}_{mb} = \tan^{-1} \frac{\tilde{m}_{my}^b}{\tilde{m}_{mx}^b} = \psi_{mb} + W_{\psi_m}$$

Where,

m=magnetometer

n=navigation frame

W=white noise

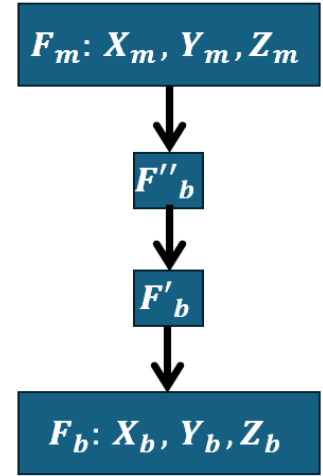


Figure 37: Reference Frame Transformation where, b- body frame, m- magnetometer reference frame

True Yaw rate and its estimate:

$$\omega_{ib,z}^b = -\omega_{ie}\sin\phi + \omega_{ie}\sin\phi + \dot{\psi}_{nb}$$

$$\omega_{nb,true}^b = \dot{\psi}_{nb}$$

Gyro measurements act as a process:

$$\tilde{\omega}_{ib,zg}^b = -\omega_{ie}\sin\phi + \omega_{nb} + b_g + \vartheta_g$$

To get the platform rotation angle in the lab from gyro, we should integrate:

$$\tilde{\omega}_{nb,g}^b = -\omega_{ie}\sin\phi + \tilde{\omega}_{ib,zg}^b - b_g - \vartheta_g$$

So, its estimate is:

$$\hat{\omega}_{nb,g}^b = \omega_{ie}\sin\phi + \hat{\omega}_{ib,zg}^b - b_g = \dot{\hat{\psi}}_{nb,g}$$

Yaw rate Estimation:

$$\hat{\omega}_{ib}^b = \hat{\omega}_{ib}^b - b_g$$

$\hat{\omega}_{ib}^b$ estimated rate.

Rate relative to the navigation frame (tangential, NED frame)

$$\hat{\omega}_{bn}^b = \hat{\omega}_{ib}^b - \omega_{ni}^b$$

$$\omega_{ni}^b = C_{bn}\psi_{nb}\omega_{ni}^n = \omega_{ie} \begin{bmatrix} \cos\psi_{nb} & \sin\psi_{nb} & 0 \\ -\sin\psi_{nb} & \cos\psi_{nb} & 0 \\ 0 & 0 & 1 \end{bmatrix} \begin{bmatrix} \cos\phi \\ 0 \\ \sin\phi \end{bmatrix} = \omega_{ie} \begin{bmatrix} \cos\psi_{nb}\cos\phi \\ -\sin\psi_{nb}\cos\phi \\ -\sin\phi \end{bmatrix}$$

$$\hat{\omega}_{bn}^b = \omega_{ie} \sin \phi + \hat{\omega}_{ib}^b = \hat{\psi}_{nb}$$

Gyro measurement of yaw rate:

$$\text{True Rate: } \omega_{ib,z}^b = (\omega_{ni} + \omega_{bn})_z$$

Where,

n represents navigation Frame

i represent inertial Frame

$$\dot{b}_{gd} = \frac{b_{gd}}{\tau_{bgd}}$$

Where ,

b=bias: s=static: d=dynamic

$$\omega_{bn}^b = (\omega_{ib} + \omega_{ni})$$

$$b_g = b_{gs} + b_{gd}$$

Earth rotation rate in the tangential or navigation frame:

$$\omega_{ni}^{Fb} = \omega_{ie} \begin{bmatrix} \cos \phi \\ 0 \\ -\sin \phi \end{bmatrix}$$

$$\omega_{ni}^b = C_{bn}(\psi) \omega_{ni}^n$$

Rate measured by the gyro:

M_b is Mis-alignment I_3 is Scale factor

$$\tilde{\omega}_{ib}^b = (I_3 + M_b) \omega_{ib}^b + b_g + \omega_g = \omega_{ib}^b + b_g + \omega_g$$

Note: Our objective is to estimate b_g and the yaw heading angle.

Kalman Filter Stability in the Discrete Domain (Discrete Process Model):

Combining the time-propagation of the state estimate and its measurement update, and taking its Z-transform,

$$[\zeta I - (\phi_{k-1} - K_k H_k \phi_{k-1})] \hat{X}(\zeta) = \zeta K_k Z_k(\zeta)$$

$$\text{Chracteristic polynomial} = |\zeta I - (\phi_{k-1} - K_k H_k \phi_{k-1})|$$

The Eigenvalue inside the unit circle denotes the Stability.

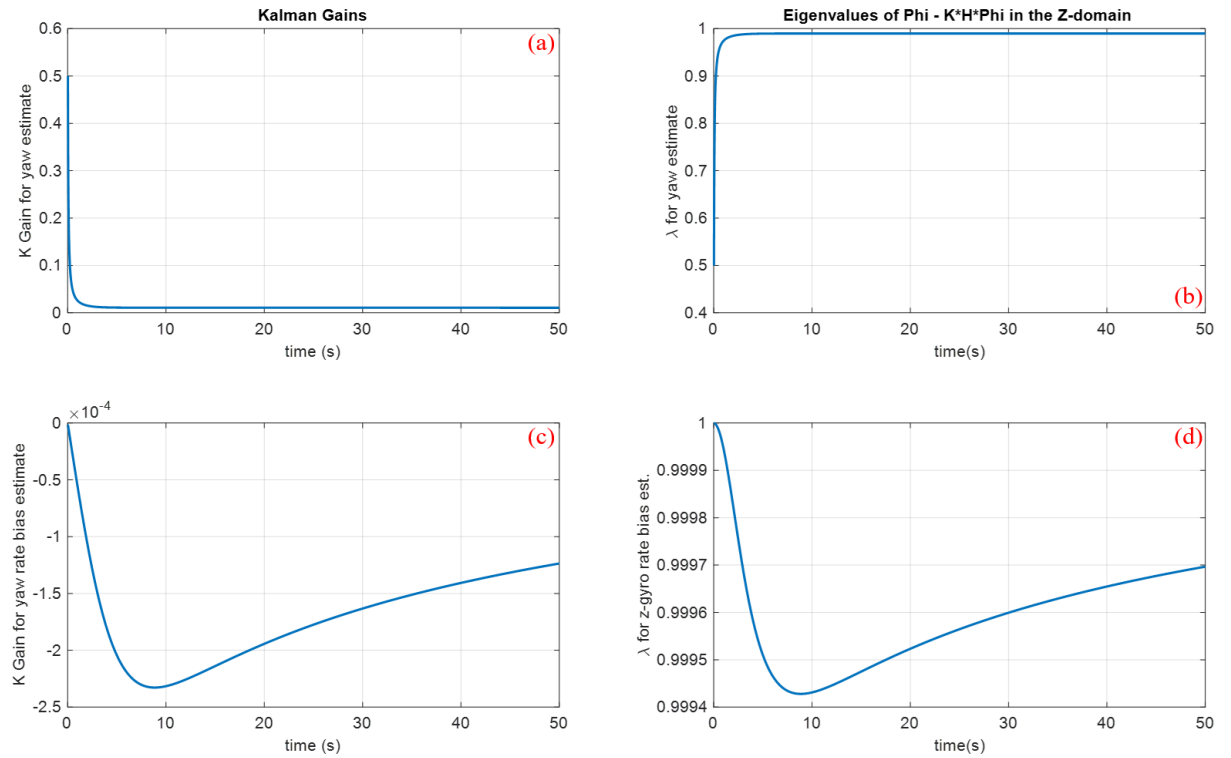


Figure 38: Figure Showing-
(a) Kalman Gain for the Yaw estimation (b) Eigenvalues of $\phi-K^*H^*\Phi$ in Z-Domain
(c) Kalman gain for yaw bias (d) Eigen value for gyro rate bias

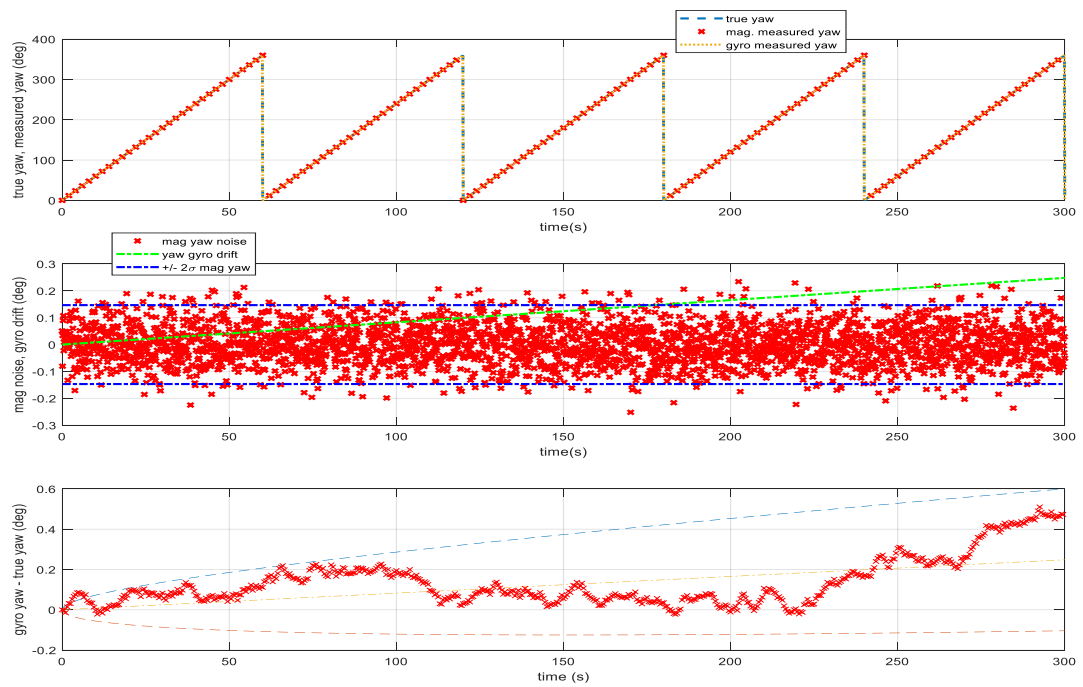


Figure 39: No magnetometer reading

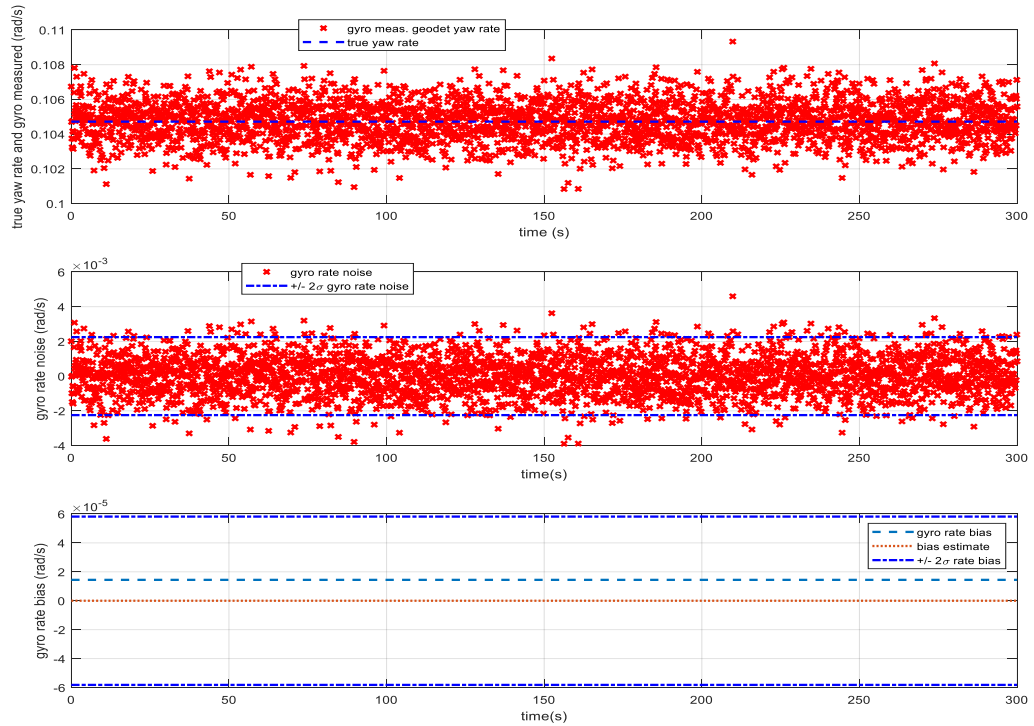


Figure 41: Gyro rate bias is not estimated since the magnetometer is not used.

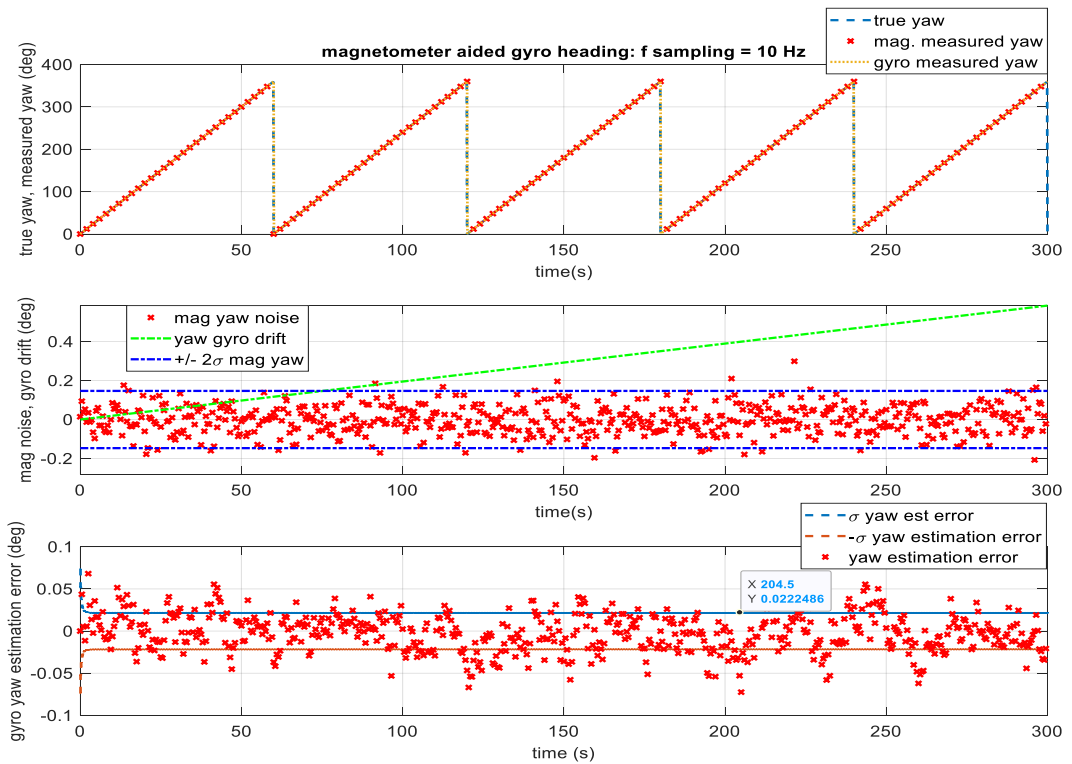


Figure 40: Magnetometer aided Gyro heading at sampling frequency $f=10\text{Hz}$

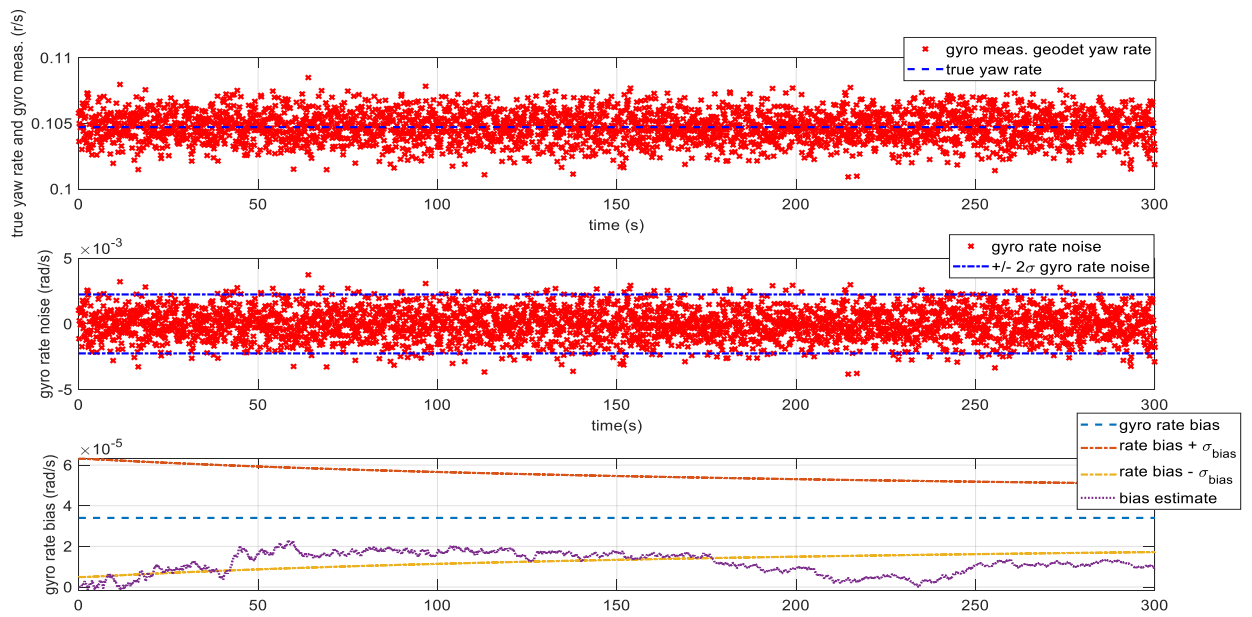


Figure 42: Gyro rate bias estimation slow at 10 Hz

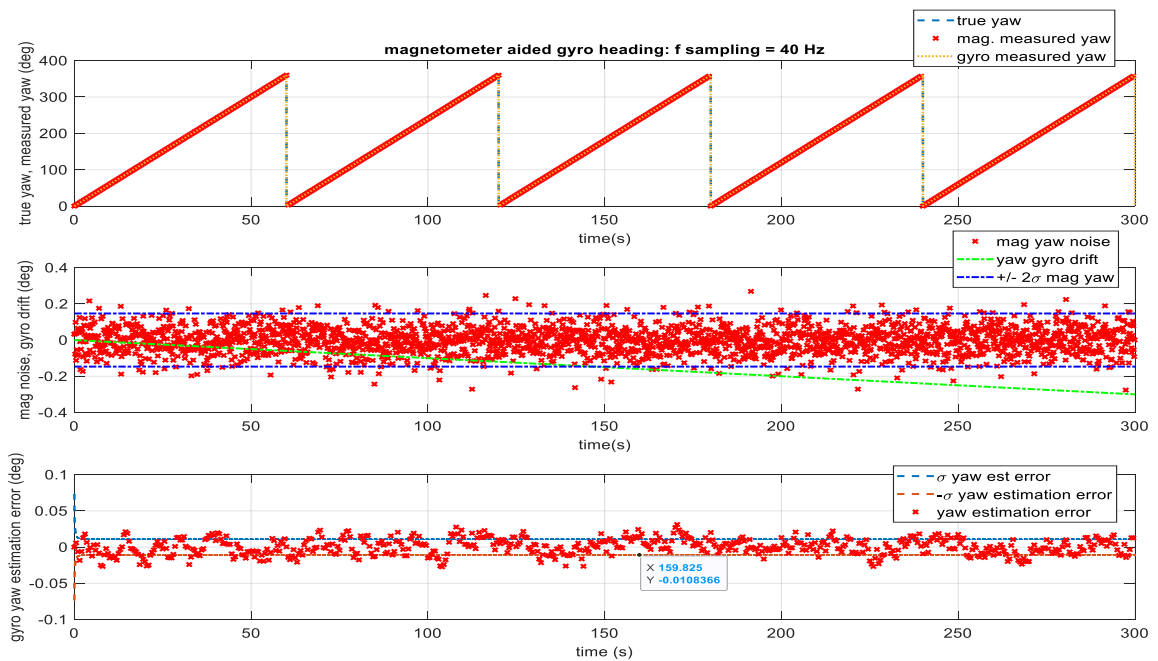


Figure 43: Magnetometer aided gyro heading error

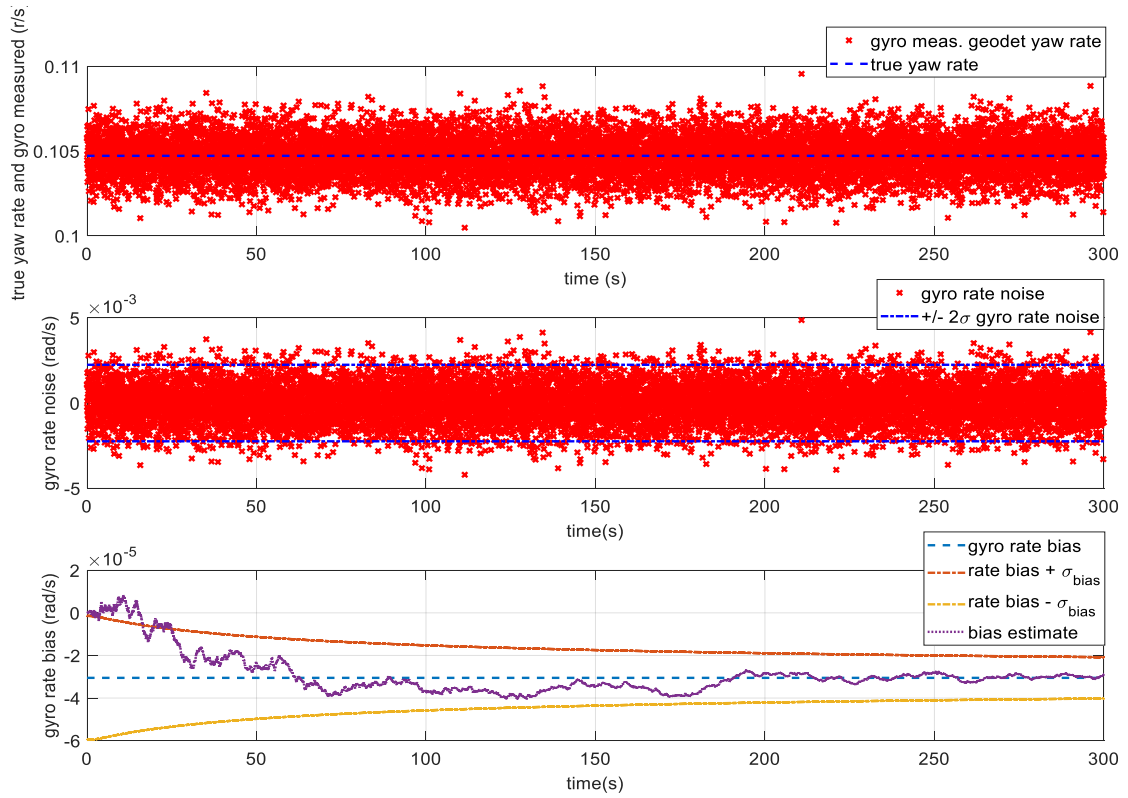


Figure 45: At 40 Hz, gyro rate bias estimation faster than at 10 Hz

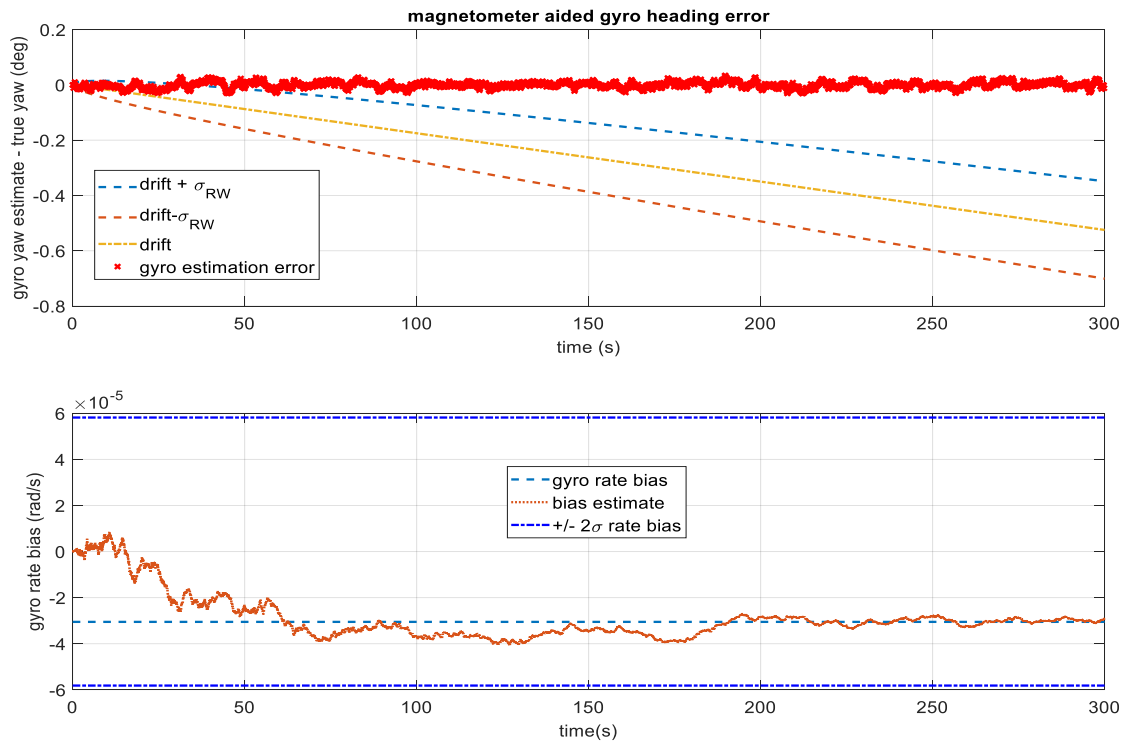


Figure 44: Magnetometer aided gyro heading error

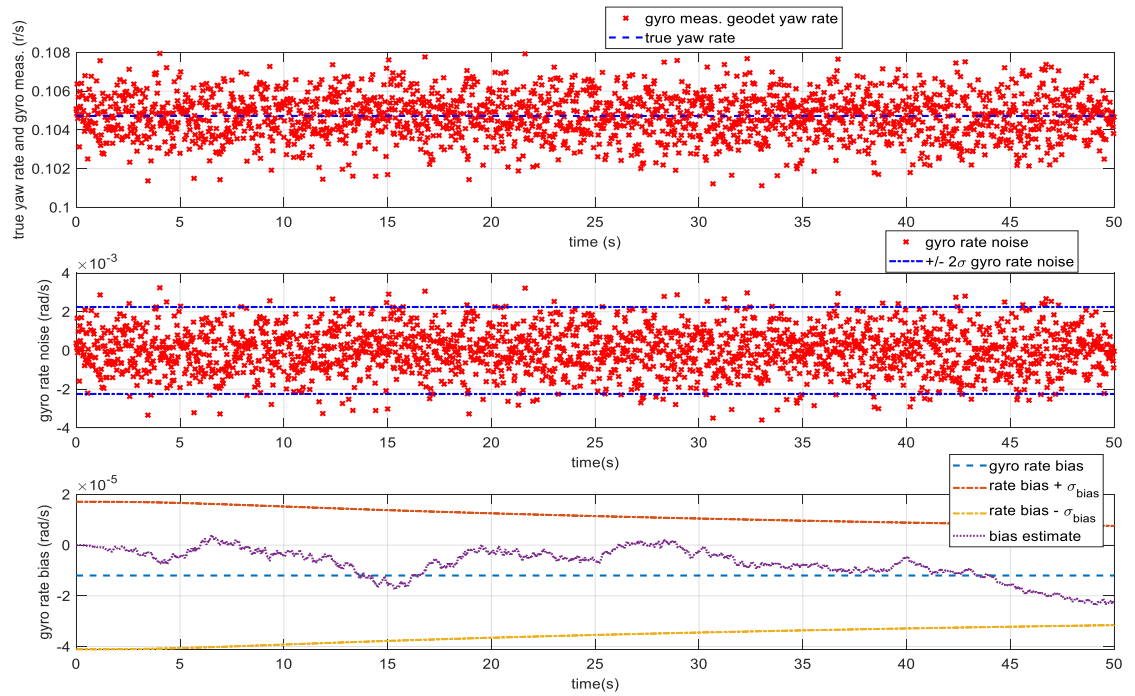


Figure 46: Over a shorter ($t=0-50s$) duration

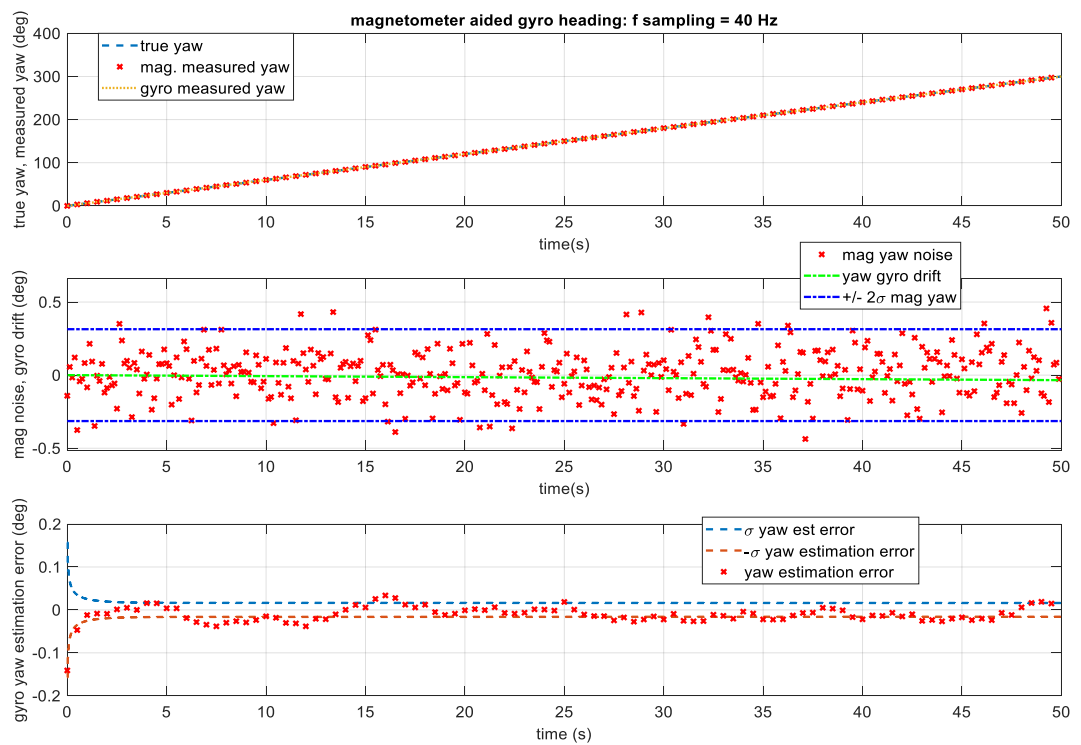


Figure 47: Gyro-rate noise with gyro rate bias

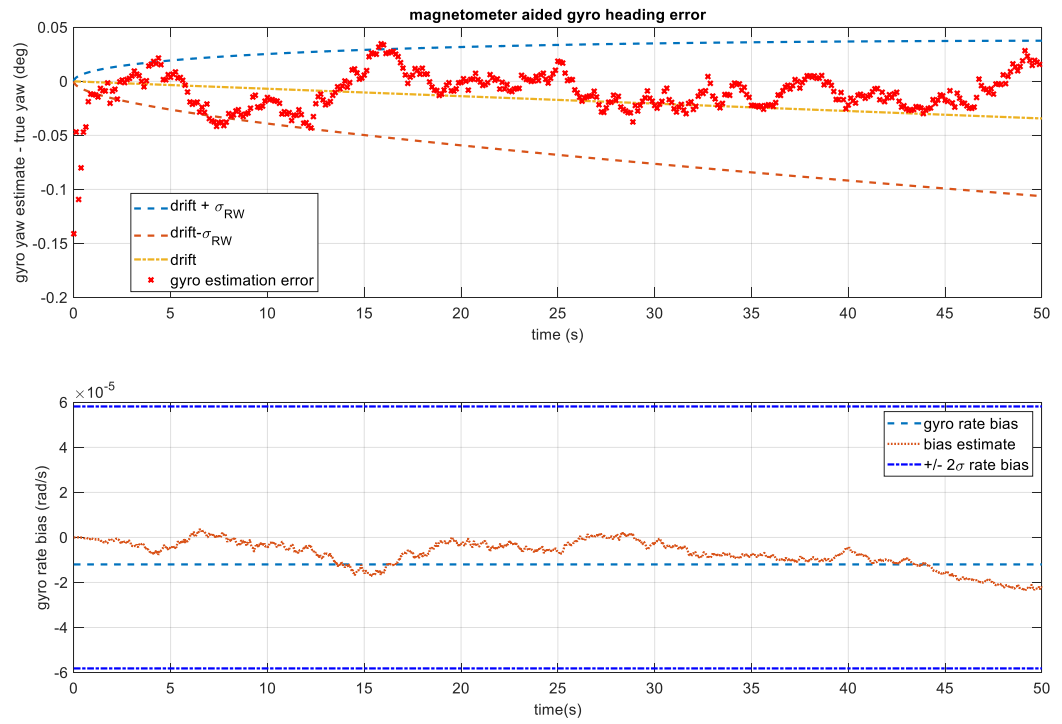


Figure 48: Magnetometer Aided-Gyro heading Error

Chapter 7: Basic Technical Integration

7.1. Basic Procedure:

My initial goal was to design and construct a bidirectional BLDC motor speed control system. Unidirectional speed control—the motor would revolve in one direction but allow variable speed adjustment—was my initial goal. The control system was based on an Arduino board, a versatile and popular microcontroller.

I added a potentiometer for manual speed adjustments and user engagement.

Potentiometers were analogue input devices that let users set speed by varying resistance. Arduino read and processed this input signal to generate PWM signals. PWM signals were sent to the motor controller, which controlled motor speed by regulating power.

After installing unidirectional speed control, project requirements changed, requiring bidirectional motor operation. The motor had to rotate clockwise and counterclockwise with accurate speed control. I updated the motor controller with a bi-directional ESC to solve this problem. A bi-directional ESC lets the motor change direction by changing control signals, unlike ordinary ESCs. This added capabilities greatly increased system adaptability.

I powered the system with an 11.1V DC power supply that met the BLDC motor and ESC's voltage and current needs. This power supply provided stable operation and enough torque during testing.

The circuit was built using a breadboard, a prototyping tool that allows quick and flexible wiring of electronic components without soldering. This design enabled iterative testing and debugging, making connection and control logic issues easier to find and fix. The breadboard made it easy to test alternative configurations before finalizing the design.

I designed a method to manage BLDC motor speed and direction using the Arduino's computational capabilities, the potentiometer's user interface, and the bi-directional ESC's sophisticated functionality. This project improved my circuit design, microcontroller programming, and component integration skills while demonstrating my motor control system knowledge.

7.2. CAD Design

To fabricate the reaction wheel for the system, a **CAD design** was created using **Autodesk Fusion 360**, a versatile and powerful tool for parametric 3D modelling. The design process involved carefully considering the dimensions, weight distribution, and structural integrity of the reaction wheel to ensure optimal performance.

1. Initial Design Parameters:

- The reaction wheel's primary function was to provide controlled angular momentum for attitude adjustments.

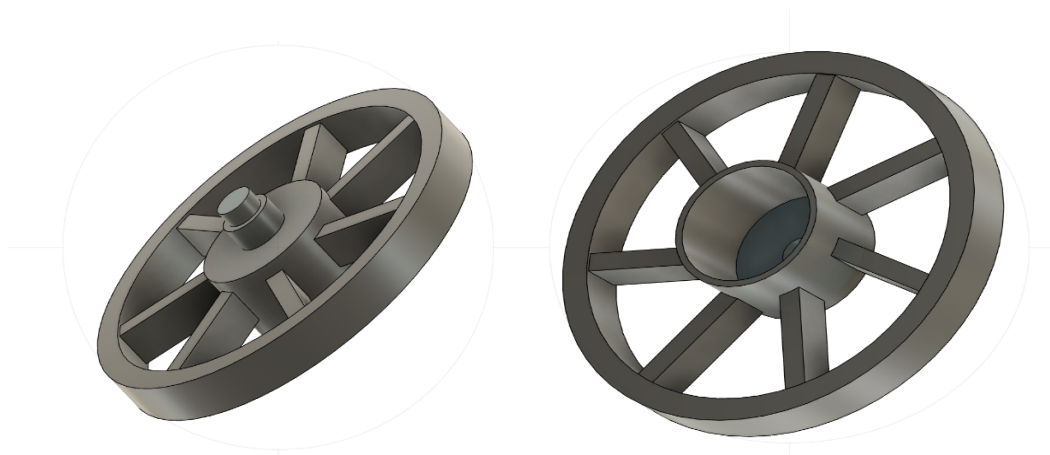


Figure 49: 3D CAD Design of the momentum wheel

- Dimensions and mass properties were calculated based on the system's torque and rotational inertia requirements.
 - The geometry was optimized for efficient rotation and minimal air resistance, ensuring smooth and stable operation.
- ### 2. Material Selection:
- A lightweight yet durable material was chosen for 3D printing i.e., PLA (Polylactic Acid) for their strength and ease of printing.
- ### 3. Modelling in Fusion 360:
- The reaction wheel was designed with precise measurements, incorporating a symmetrical structure to avoid imbalance during rotation.
 - The design included features such as a central hub for secure mounting to the motor shaft and radial spokes or a solid disc, depending on the weight constraints.
 - Simulations were conducted in Fusion 360 to validate the design against expected stress and strain under operational loads.

4. Manufacturing Process/ 3D Printing Setup:

- The finalized CAD model was exported in STL format and imported into a slicing software to generate the G-code for the 3D printer.
- Parameters such as layer height, infill density, and printing speed were optimized to ensure a high-quality print.

5. Printing the Reaction Wheel:

- A 3D printer was used to fabricate the design. The process involved extruding the chosen material layer by layer to create the final shape.
- Post-printing, the wheel was carefully inspected for defects and excess material was trimmed if necessary.

The resultant reaction wheel demonstrated exceptional dimensional precision and structural integrity. The lightweight design reduced the burden on the motor while ensuring adequate angular momentum for accurate control. The excellent amalgamation of CAD design and 3D printing processes exemplified the efficacy of fast prototyping in aerospace applications.

7.3. Initial model testing in one Axis

Upon assembling and validating the system's operation, the subsequent phase involved testing the configuration in real-world conditions. To achieve this objective, the motor and its control circuits were firmly affixed to a stable support structure. This arrangement guaranteed stability during testing, enabling the system to function without external vibrations or unintentional movements influencing the results.

The sturdy support served as a stable reference frame, allowing for precise observation and assessment of the motor's performance. The motor's rotation, velocity, and directional control were assessed under multiple circumstances to verify the system's operation. Suspending the configuration in this manner facilitated:

1. Load-Free Testing: By suspending the entire system freely, it was feasible to evaluate its operational behaviour devoid of supplementary mechanical stresses. This offered clear insight into how it reacts to velocity and rotational commands.
2. Safety and Stability: The sturdy support eliminated the possibility of components detaching or shifting during operation, assuring safe testing conditions.

3. **Functionality Monitoring:** By analysing the motor's operation, I was able to adjust the system's characteristics, including the PWM signal range and ESC configurations, to attain ideal performance.

This stage of the project served as a crucial milestone, as it confirmed the integration and synchronization of all components in the system. Additionally, this testing method facilitated the identification of future enhancements, including the augmentation of structural support and the optimization of control algorithms to achieve superior precision in dynamic situations. The successful test proved the system's reliability and preparedness for prospective applications necessitating precision motor control.

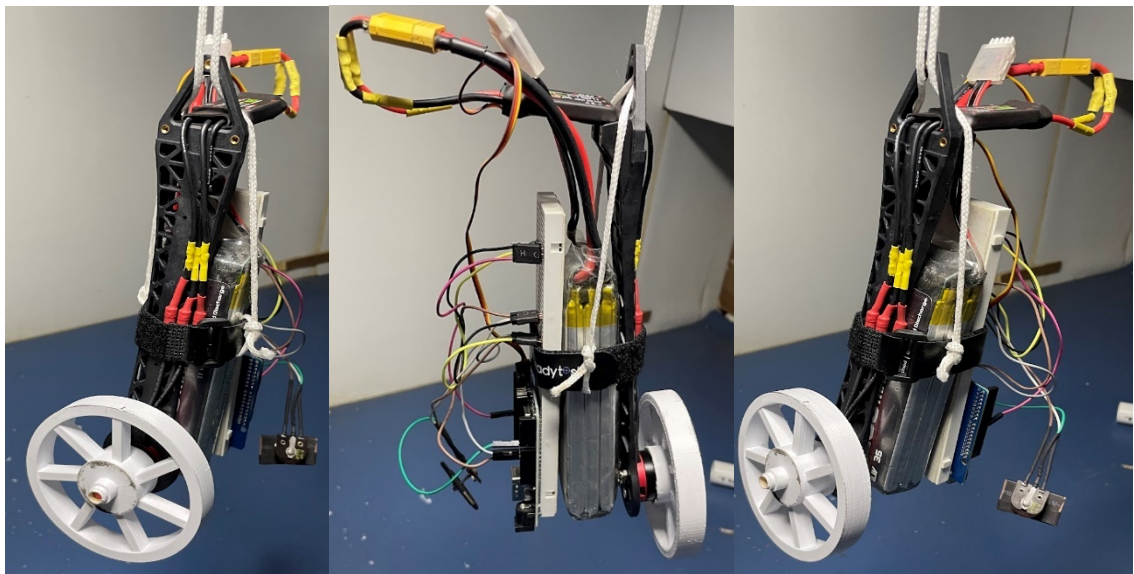


Figure 50: Images of the Experimental setup

7.4 Power System Circuit

The system utilized an XL4016 module, a DC-DC buck converter, to manage the battery's input voltage and deliver a uniform result for powering the Arduino board and additional components. The XL4016 was linked to an 11.1V battery (presumably Li-ion or LiPo), with its input terminals receiving the battery supply and its output terminals providing a controlled voltage of 4.5V. The module's integrated potentiometer was employed to precisely adjust the output voltage, assuring compliance with the system's specifications. The output was calibrated to 4.5V, appropriate for the operation of the Arduino board. The Arduino board was linked to the XL4016's output through the

power connector, guaranteeing a clean and reliable power supply to avert voltage fluctuations or surges. Upon establishing the connections and configuring the voltage, the system was energized by activating the battery supply. This setup ensured a dependable power supply, facilitating the seamless operation of the Arduino and its connected components, while shielding delicate electronics from power fluctuations.

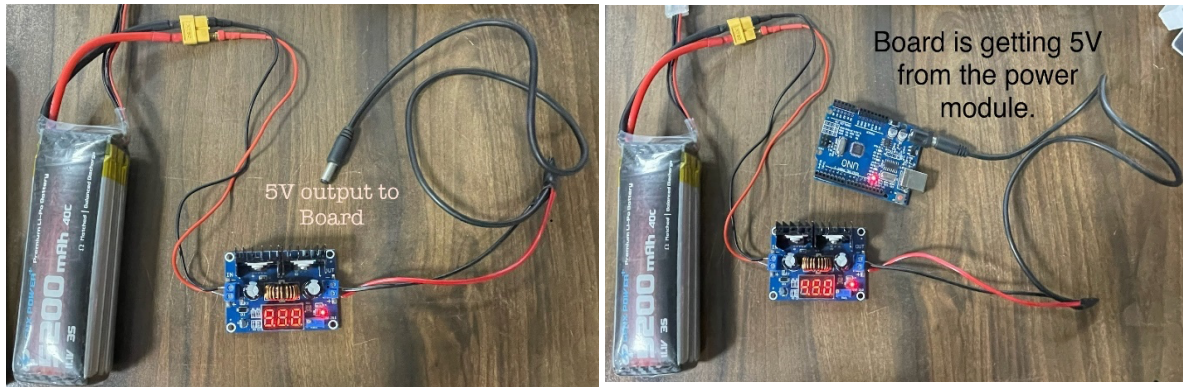


Figure 52: DC-DC Bulk converter before and after Power

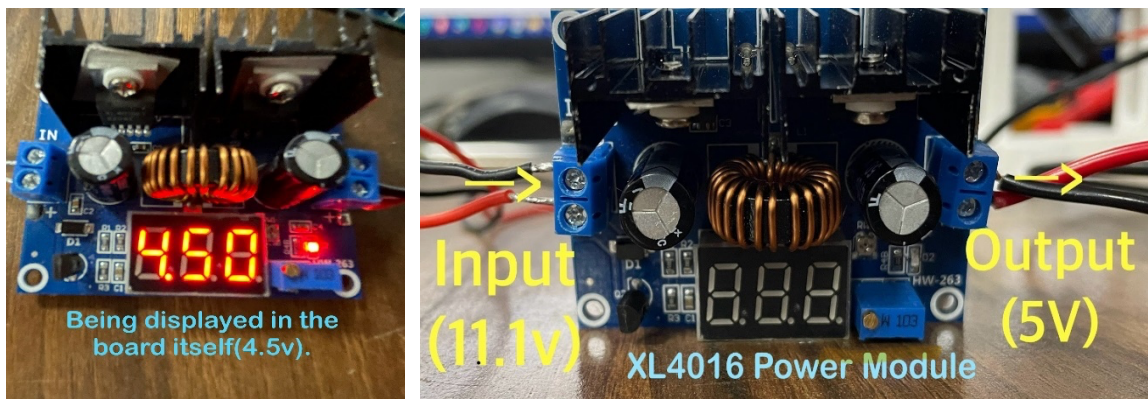


Figure 51: Complete Circuit of Power System

7.5 Single Motor Testing:

7.5.1 Experimental Setup:

To enable precise control of motor operation, an Electronic Speed Controller (ESC) is interfaced with a Brushless DC (BLDC) motor in the experimental setup used for this study. A buck converter powers the ESC by stepping down the voltage from a regulated power source. This ensures that the voltage levels supplied to the ESC and then to the motor are within safe and ideal operating ranges. The Pulse Width Modulation (PWM) signals used in the control process are observed and examined using a digital

oscilloscope. These PWM signals can be seen at the output stages that drive the motor phases or at the ESC input, which receives control signals from a microcontroller or signal generator. The configuration is designed to enable detailed evaluation of motor control dynamics, signal integrity, and power delivery characteristics, which are essential for validating system performance and optimizing control strategies in BLDC motor applications.

Maximum RPM	Given Voltage(V)
9700	15
7800	12
5800	9
3300	6

Table 18: RPM Variation with Voltage

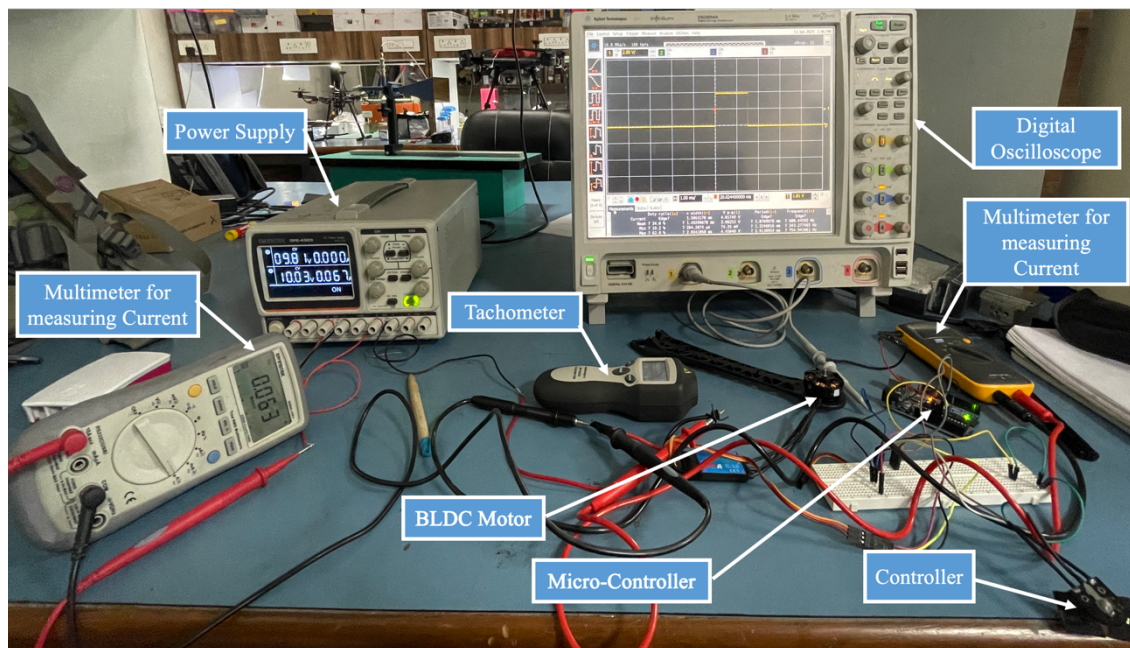


Figure 53: Complete experimental single motor setup

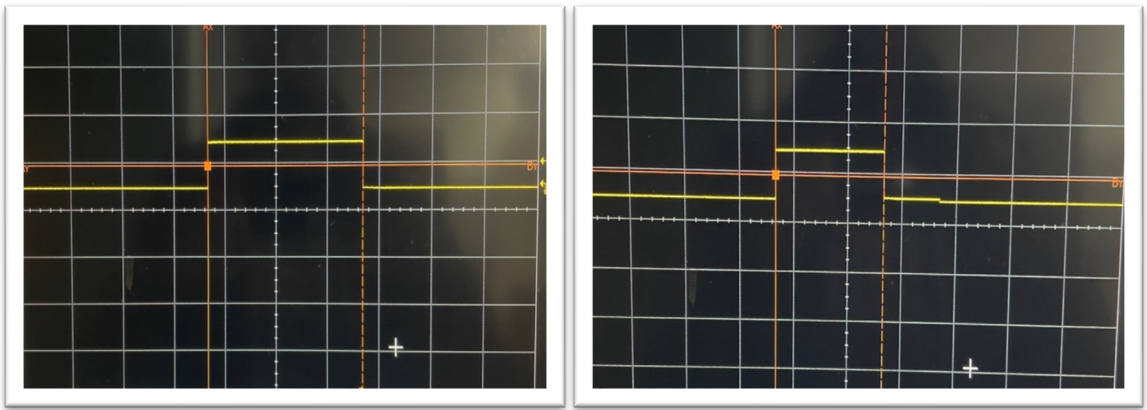


Figure 54:(a) PWM in Zero RPM (b)PWM in counter-clockwise full RPM

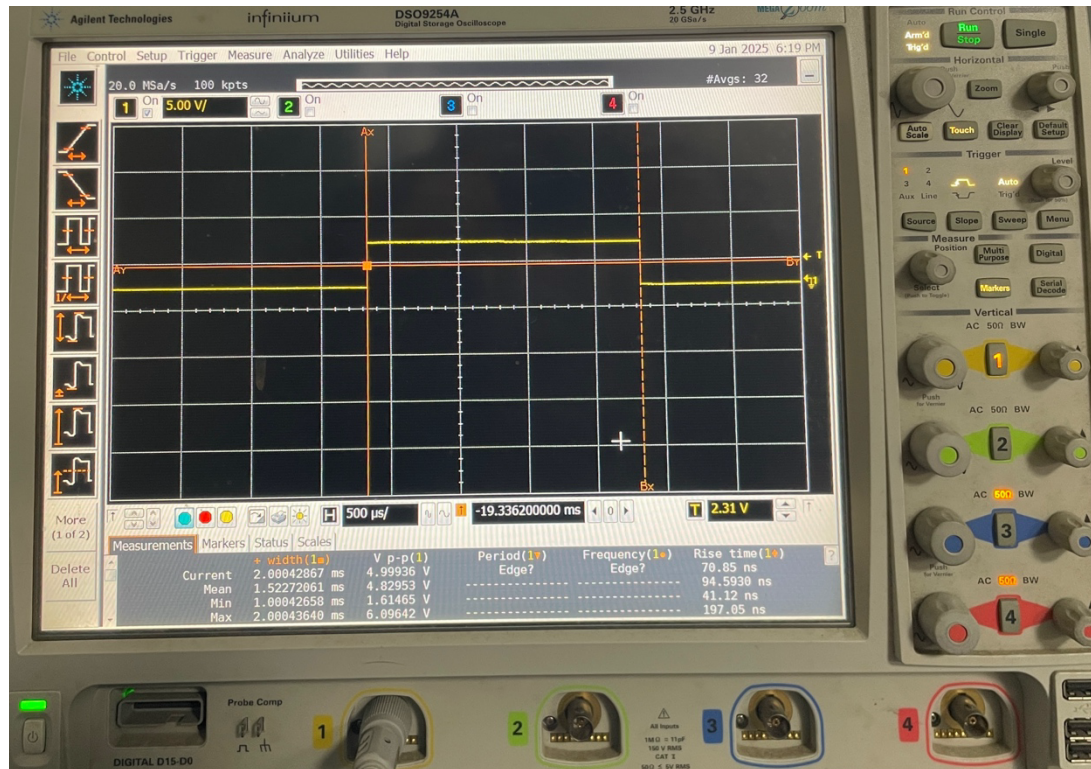


Figure 55: PWM in clockwise full in a digital oscilloscope

7.5.2. Experimental Result:

No.	Supply (in V)	Zero RPM Value		Clockwise			Counter-Clockwise		
		I (mA)	O (RPM)	Current (In V)	Current (In mA)	RPM (In RPM)	Current (In V)	Current (In mA)	RPM (In RPM)
1	6V	52	48	5.28	198	3610	5.27	204	3588
2	7V	67	62	6.97	230	4250	6.98	232	4195
3	7.5V	74	68	7.39	236	4870	7.39	239	4870
4	8V	67	63	7.95	236	4870	7.91	236	7860
5	9V	67	63	8.93	242	5505	8.89	255	5499
6	10V	67	63	9.99	258	6155	9.92	262	6151
7	11V	68	61	10.96	266	6740	10.91	277	6747
8	12V	68	65	11.96	271	7402	11.91	273	7408
9	12.5V	69	65	12.95	283	8039	12.96	293	8036

Table 19: Table to Study the RPM difference with the voltage variation.

The result includes the PWM range of the bidirectional motor. Due to the increase in voltage the maximum RPM range increases. But due to increasing voltage above 15.2V the ESC burns out. The maximum PWM is clockwise potentiometer, mid PWM (as shown in figure 56) when the PWM is zero, minimum PWM is when we turn the potentiometer to anti-clockwise.

7.6. Three Motor Testing Experiment :

7.6.1 Experimental Setup:

In the experimental setup used in this study, a Brushless DC (BLDC) motor is interfaced with an Electronic Speed Controller (ESC) to allow for precise control of motor operation. By stepping down the voltage from a regulated power source, a buck converter powers the ESC and keeps the voltage levels supplied to the motor and ESC within safe and ideal operating ranges. A digital oscilloscope is used to monitor and analyse the Pulse Width Modulation (PWM) signals used in the control process. These PWM signals can be seen at the output stages that power the motor phases or at the ESC input, which receives control signals from a microcontroller or signal generator. In order to validate system performance and optimize control strategies in BLDC motor applications, this configuration makes it possible to thoroughly assess motor control dynamics, signal integrity, and power delivery characteristics.

Three separate BLDC motors, each connected to a separate potentiometer for speed control, were used in the same process to guarantee the consistency, repeatability, and dependability of the experimental findings. This method guarantees that the conclusions reached are not restricted to a single motor setup and enables a wider validation of the control strategy across various motor characteristics.

7.6.2 Experimental Result:

The Same result as produced with single motor. And so we can proceed with the other electronic Circuit design and further functionality test.

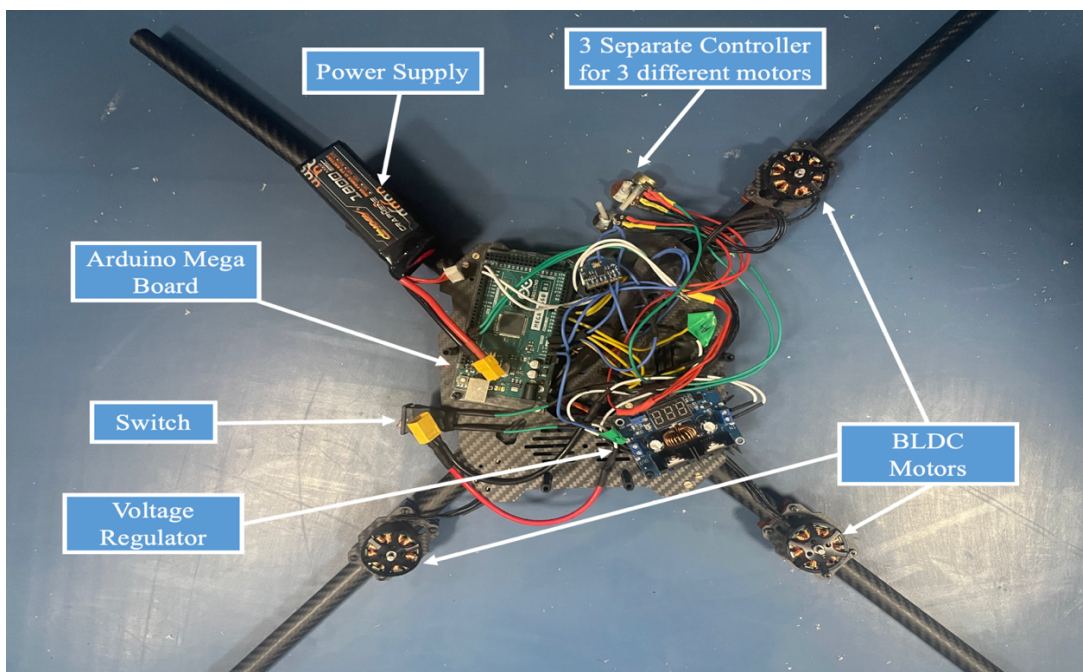


Figure 56: Experimental Setup with 3 motors

Chapter 8: Design and Design Analysis of SHOURYA

8.1 SHOURYA's Design

The SHOURYA or the Satellite Hardware

Operational Unit for Real-time Yield and Analysis is

a ADCS system to test the attitude of a cube sat, it

also provide a real time . By removing direct contact

between surfaces and supporting a load with a thin

layer of air, SHOURYA reduces wear and friction to

almost zero. It offer incredibly smooth, accurate, and

low-resistance motion in contrast to conventional

bearings that depend on rolling elements or

lubrication. Because they can maintain stability,

accuracy, and repeatability under extremely tight tolerances, they are frequently utilized

in high-precision applications like scientific instrumentation, semiconductor

manufacturing, aerospace and space Industry. This picture below show the proposed

design and the final model, and I will show in the upcoming chapter that how would we achieve the final product or the model.



Figure 57: The SHOURYA

8.2 Types of Air-Bearing

There are various kinds of air bearings, and each one's working principles make it

appropriate for a particular application. Aerostatic bearings enable incredibly accurate

and stable operation, especially at low speeds, by forming a thin air film between

surfaces using an external source of pressurized air. Aerodynamic bearings, on the other

hand, are perfect for high-speed applications because they create the supporting air film

by the relative motion of the surfaces themselves, negating the need for an external air

supply. In order to maximize performance, hybrid air bearings combine the two ideas by

using an external air supply at low speeds and switching to self-generating air films at

higher speeds. Another significant kind is the porous surface air bearing, which

provides smooth motion and reduced air consumption by uniformly distributing air

through a porous material such as graphite or ceramics. Lastly, orifice air bearings, a

conventional and popular design in precision machinery, regulate airflow through tiny,

precisely crafted holes on the bearing surface. Specific requirements like load capacity,

speed, accuracy, and stability are taken into consideration when choosing an air bearing

types. Here I have used Aerostatic and orifice technology all together. Like on application based it is aerostatic but construction wise it is orifice air bearing.

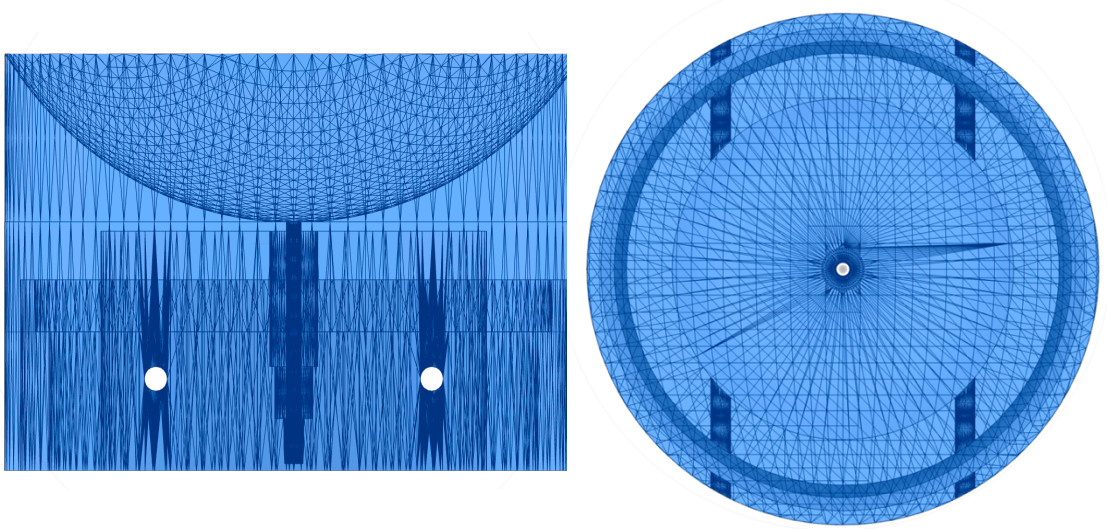


Figure 58: Left, we have side view to see the orifice and the two other hole for support screw. In the right we have top view to see the actual orifice.

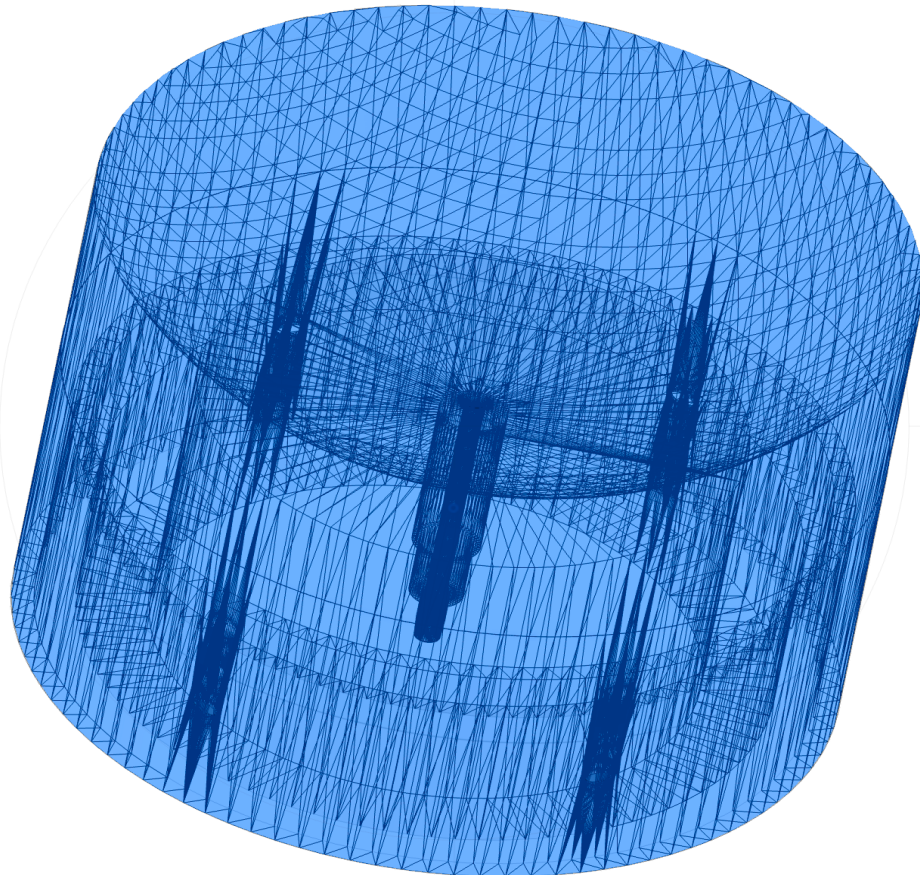


Figure 59: The Isometric View for proper view.

8.3 Designs

All the designs in this project are unique and have been developed completely from scratch. Initially, the designs were conceptualized using the traditional method of pen and paper, allowing for freehand creativity and iterative sketching. Following the initial sketches, the designs were refined and finalized based on the resources and materials available, ensuring that each concept was both practical and achievable within the given constraints.

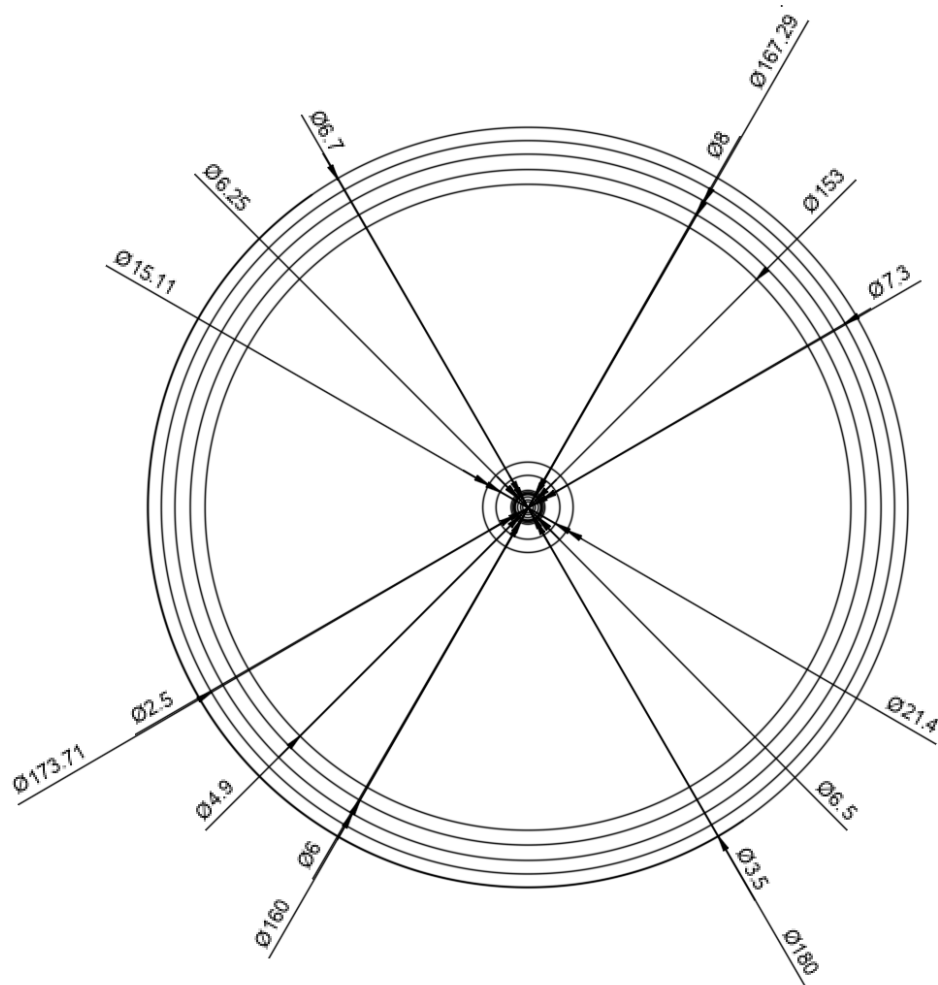


Figure 60: Top view of the Hemispherical bottom of the top section (unit in mm)

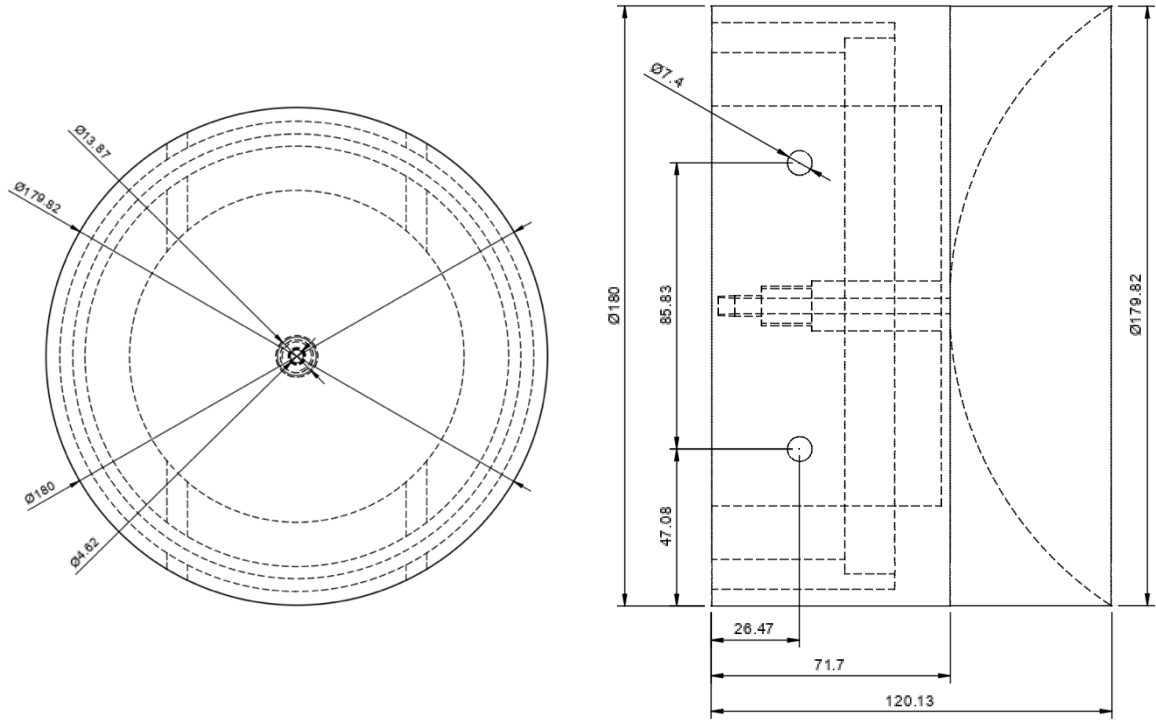


Figure 61: Detail 2D drawing of the head of the lower section. Left side is the top view and right side is the side View(unit in mm).

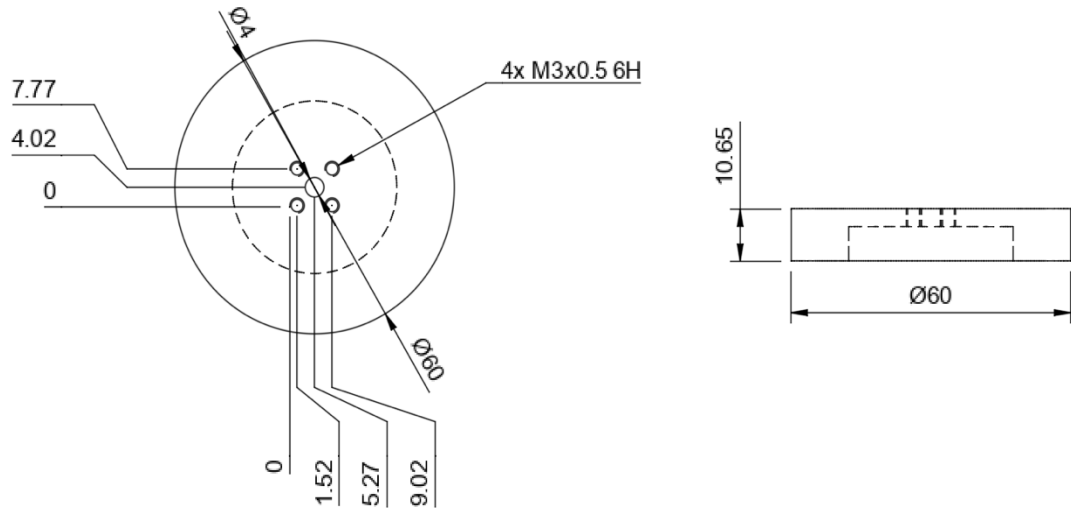


Figure 62: Detail 2D drawing of the momentum wheel. Left side is the top view and right side is the side view(unit in mm).

8.4 3D Design

The 3D designs of the momentum wheel, the upper hemispherical structure, and the lower base head were developed using Fusion 360 to specifically meet the system requirements while also adhering to the necessary design criteria. Each component was carefully modelled to ensure structural integrity, functionality, and compatibility with the overall system. The use of Fusion 360 enabled precise dimensional control, efficient design iteration, and seamless integration of all parts, ensuring that the final assembly not only fulfilled operational needs but also maintained high standards of manufacturability and performance. So I have used the Fusion 360 platform to simulate and design. Different manufacturing process are being used which will be discussed later in this chapter.

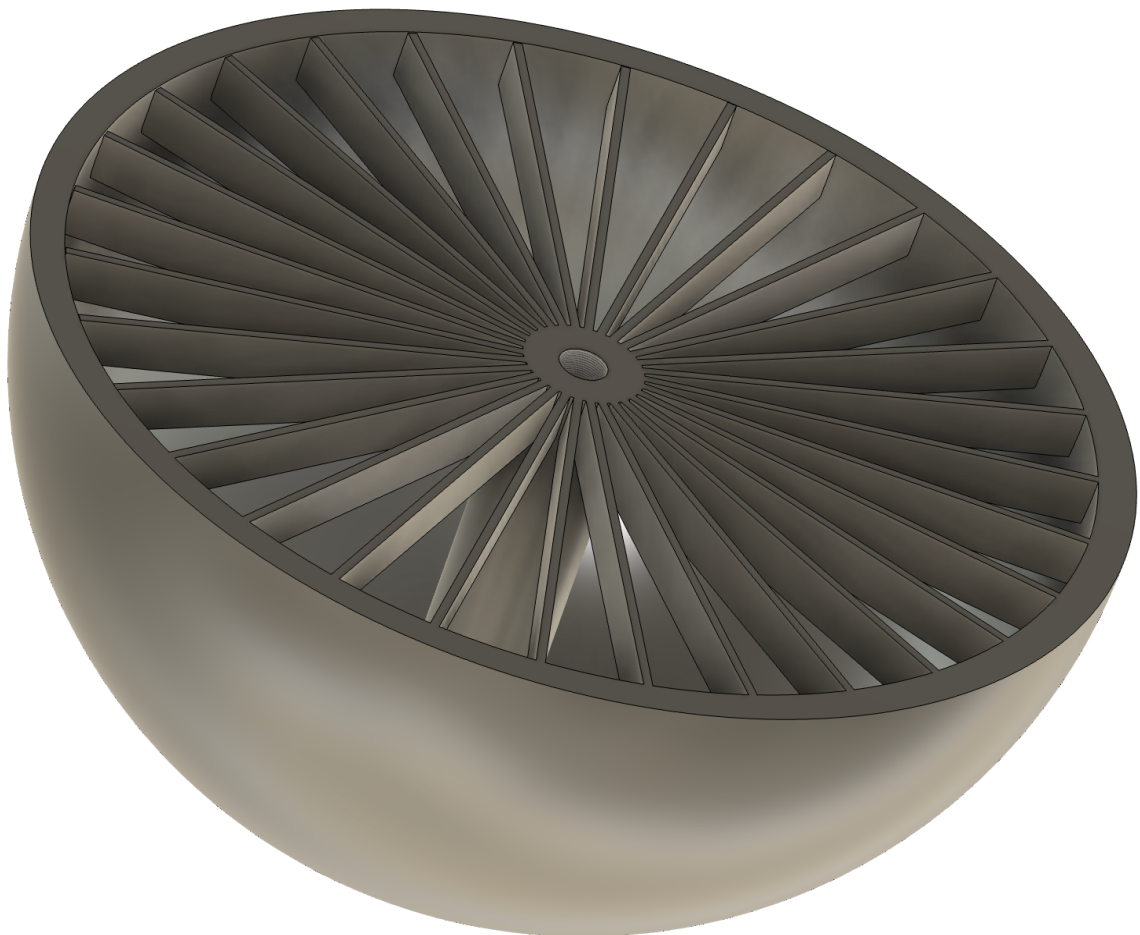


Figure 63: Isometric view of the Hemispherical bottom

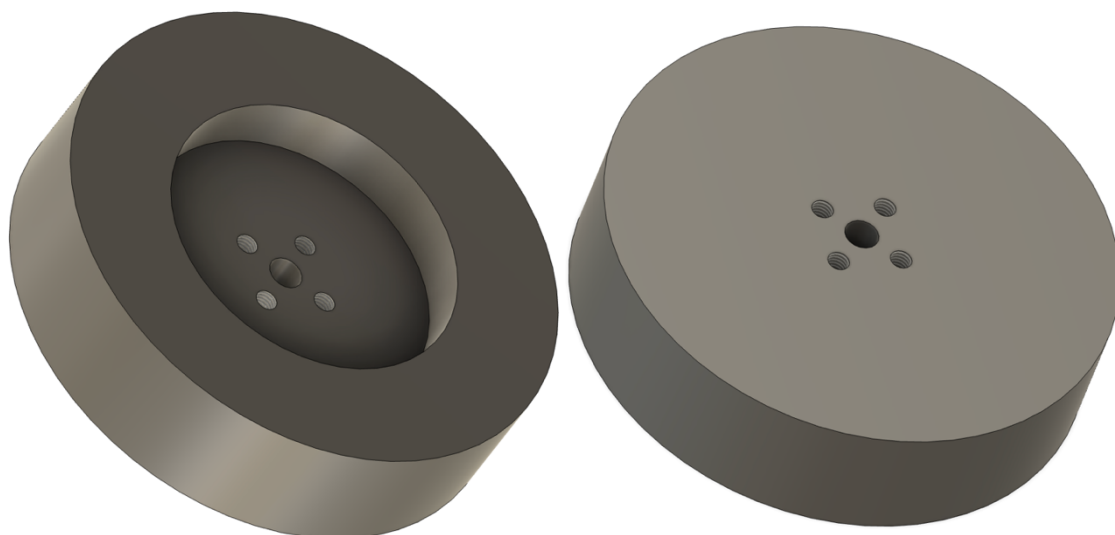


Figure 64: Isometric view of the momentum wheel

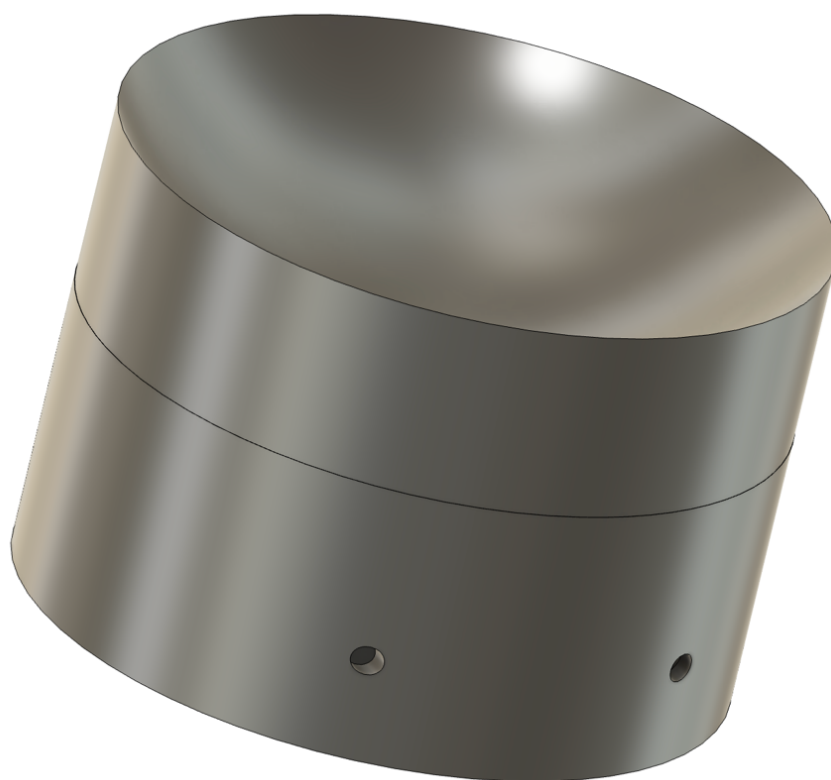


Figure 65: Isometric view of the top side of the head of the lower base.

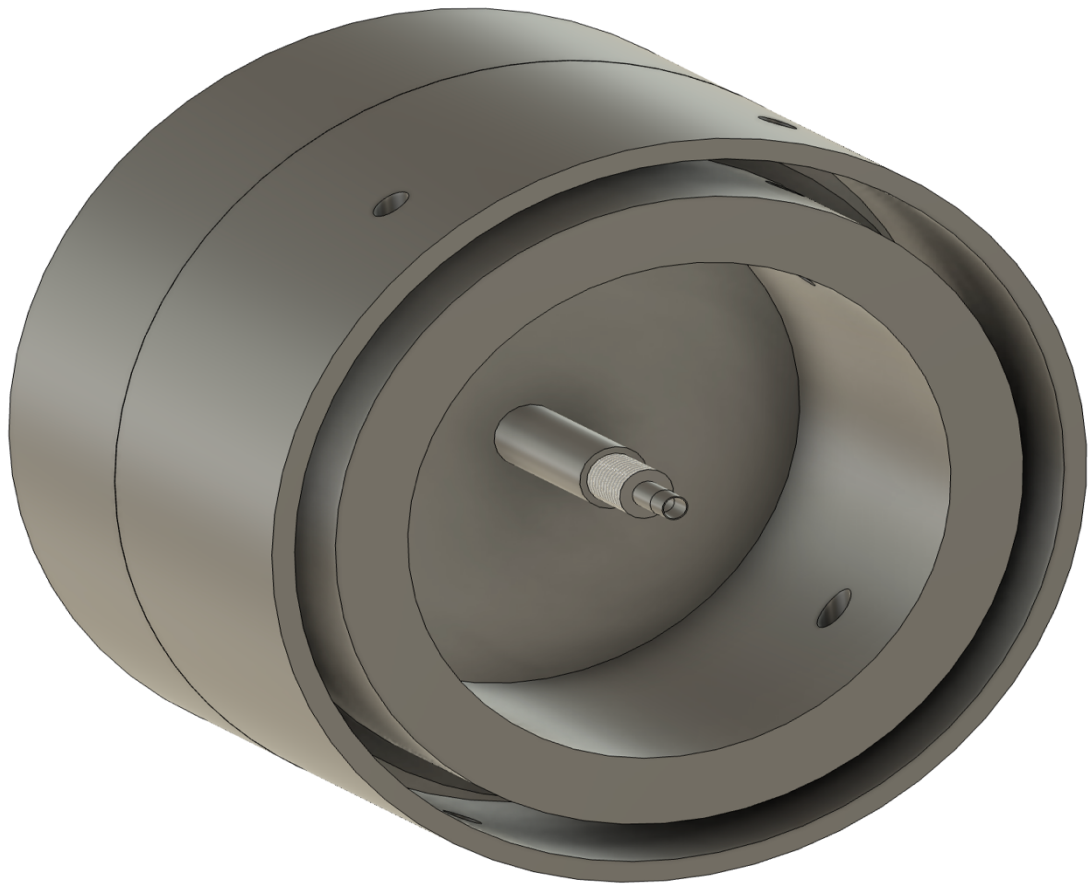


Figure 66: Isometric view of the bottom side of the head of the lower base.

8.5 Design Analysis

All the designs, including the momentum wheel, the upper hemispherical structure, and the lower base head, were created to specifically meet the system requirements while also satisfying the necessary design criteria. Careful attention was given to both functionality and structural integrity during the development process. Additionally, simulation techniques were employed to pre-analyse the design states, allowing for the prediction and evaluation of performance under various conditions. This approach ensured that the designs were optimized effectively to meet both operational demands and system performance expectations. The analysis also save the cost to a greater extent. So, the below picture (Figure 67) shows the cost reduction after adding innovation and rigorous analysis.

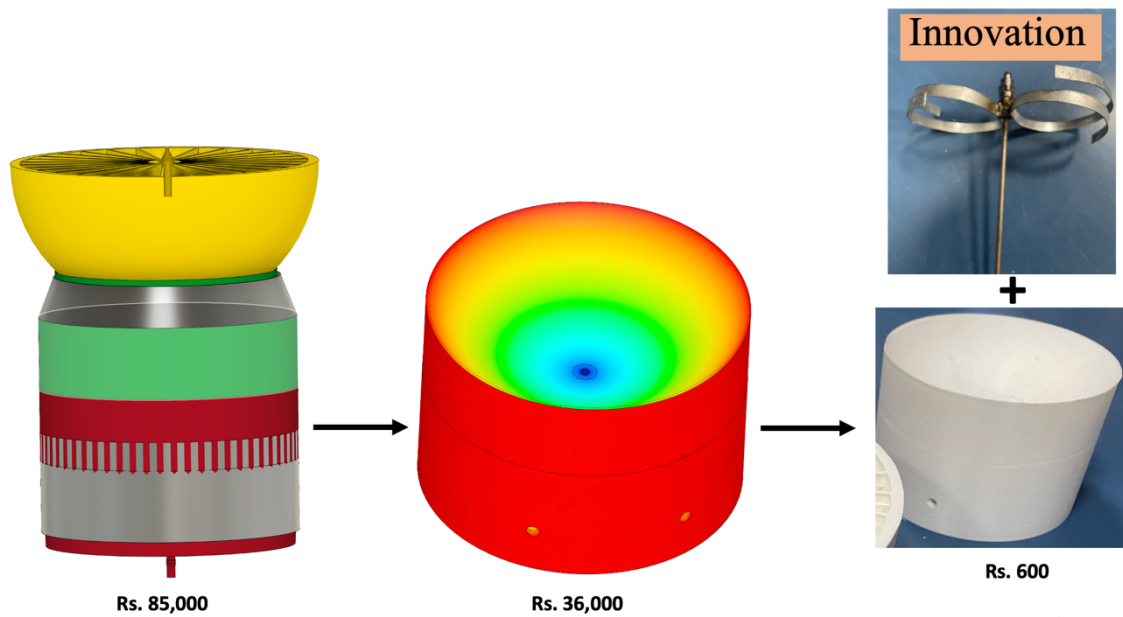


Figure 67: Cost reduction due to Analysis and innovation

8.5.1 Structural Analysis

Structural analysis is a crucial pre-manufacturing step that determines whether the designed structure will be feasible and capable of withstanding expected loads and stresses. This analysis helps in identifying potential weaknesses or failure points before actual fabrication begins, ensuring that the structure can perform reliably under operational conditions. The advantages of conducting structural analysis prior to manufacturing include reducing material wastage, optimizing the design for better strength-to-weight ratios, minimizing manufacturing costs, and improving overall safety and performance. Additionally, it allows for early detection of design flaws, which can be corrected without the expense and time involved in reworking manufactured parts.

As illustrated in **Figure 68**, a previously designed structure showed red-stripe regions indicating potential failure zones under stress, highlighting the importance of iterative validation. **Figure 69** presents the top and bottom views of the final design of the lower base head, showcasing how the design evolved to meet structural integrity requirements. Further, **Figure 70** demonstrates the presence of buckling under specific load distributions due to rotational forces, which directly influenced the choice of material used in the final version to ensure sufficient rigidity and resilience under dynamic loading.

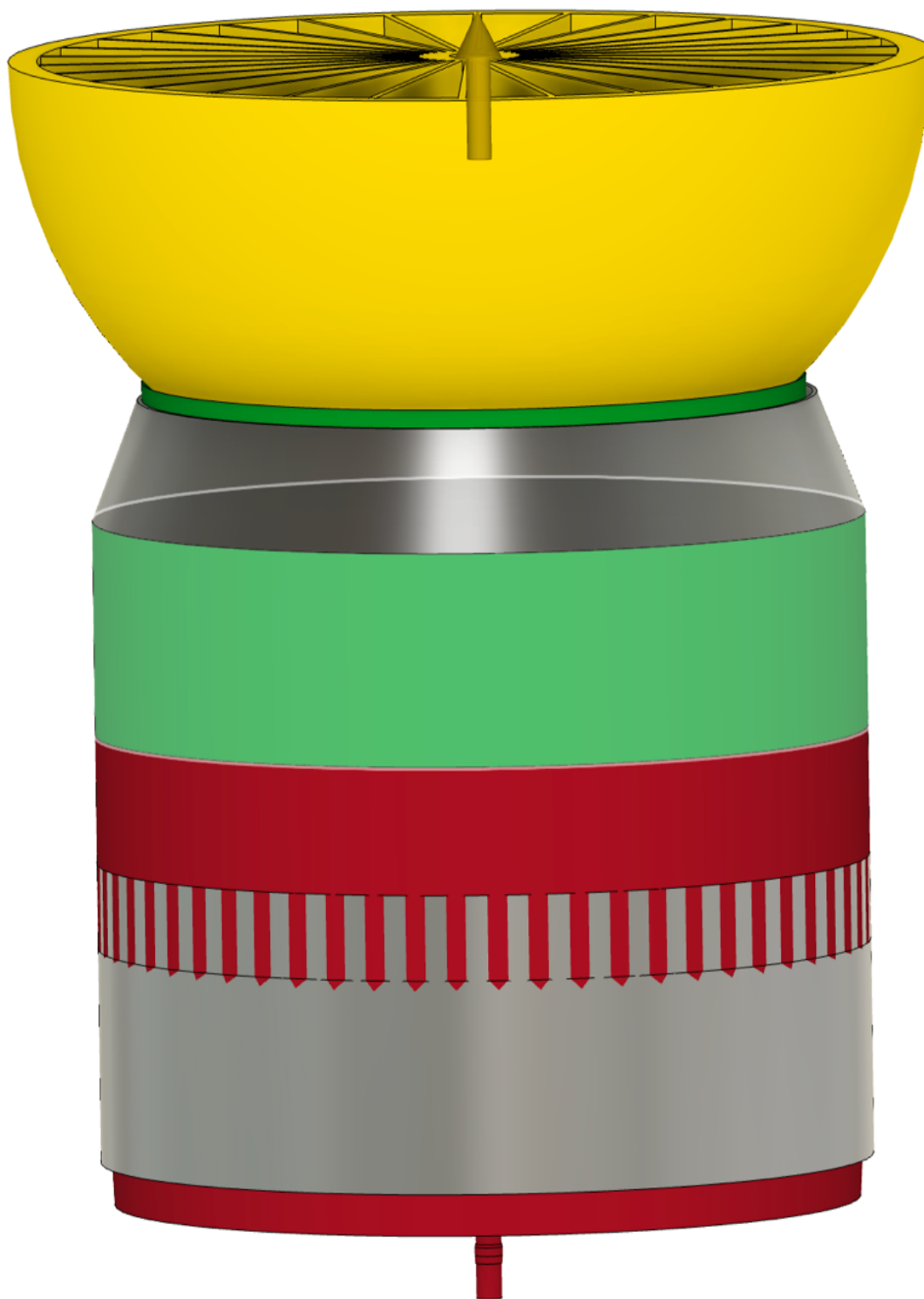


Figure 68: Previously made structure where the red stripes shows the indication of the possible failure.

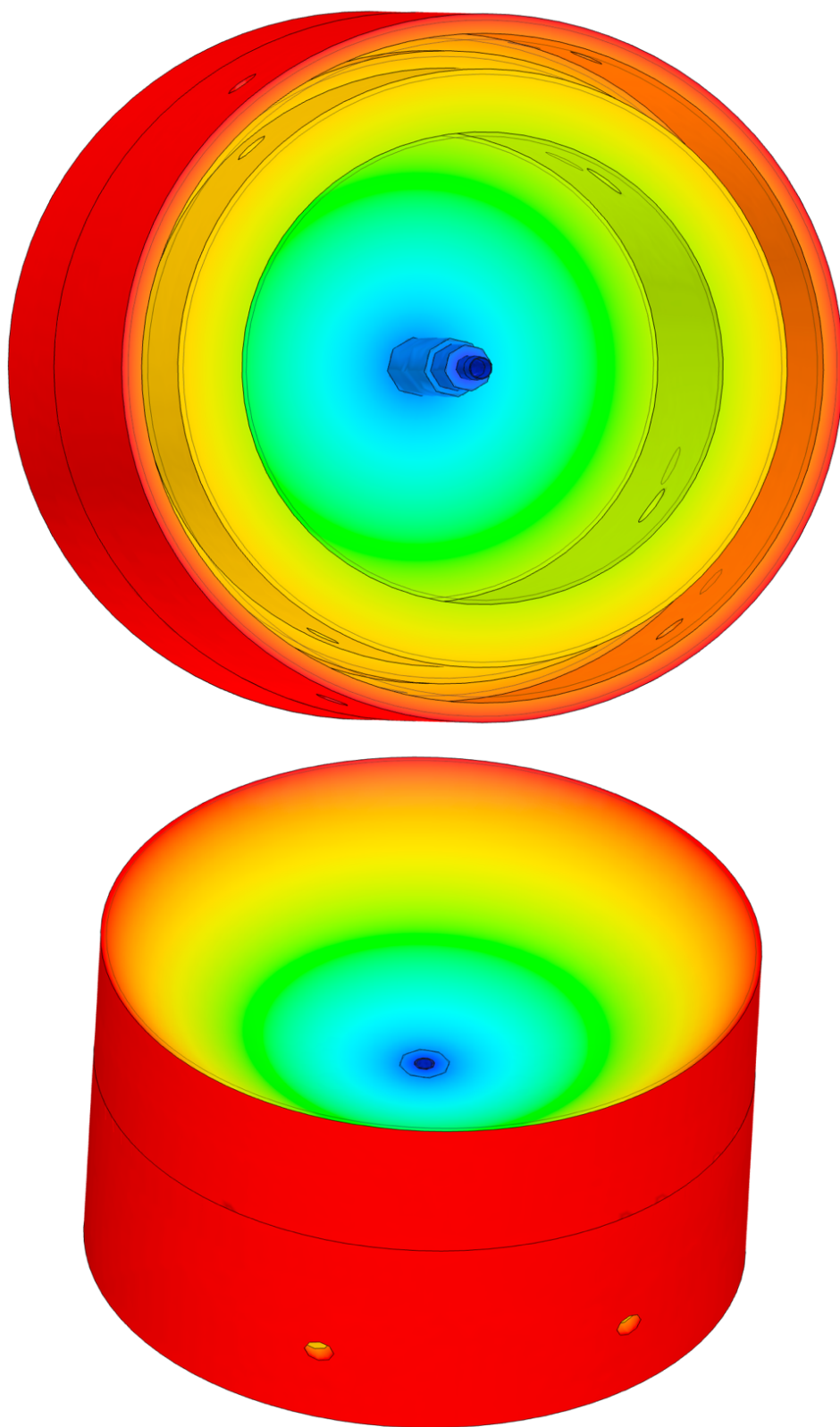


Figure 69:top-Bottom side of the final design, Bottom image: top side of the final Design of lover base head.

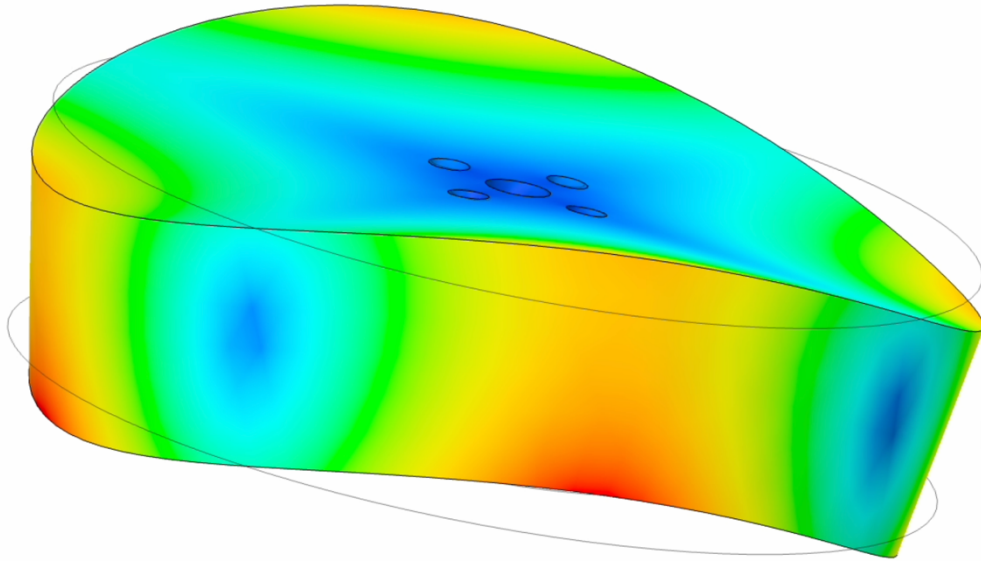


Figure 70: Buckling is shown on a particular load distribution due to rotation, so the material selection is done accordingly.

8.5.2 Acoustic analysis

Acoustic analysis is a critical pre-manufacturing evaluation that focuses on understanding how a structure responds to sound and vibrational influences. This type of analysis is essential for assessing the noise levels generated by the system and ensuring that vibrations do not compromise structural integrity or functional performance. By predicting acoustic behaviour during the early design phase, engineers can make necessary modifications to reduce unwanted noise, enhance operational stability, and improve overall user comfort. Key advantages of conducting acoustic analysis include minimizing noise pollution, prolonging the lifespan of mechanical components by mitigating vibrational stress, improving system efficiency, and complying with regulatory sound-level standards. As illustrated in **Figure 71**, acoustic analysis of a previously fabricated structure reveals critical areas prone to failure due to vibrational stress. Additionally, **Figure 72** demonstrates that when a part is manufactured as a single piece, structural stability is preserved, whereas dividing the structure into two components introduces deformities. The image also illustrates a gradual fading of vibration, indicating improved acoustic damping in optimized designs.



Figure 71: Acoustic Analysis of a previously made structure and the area of failure can be identified.

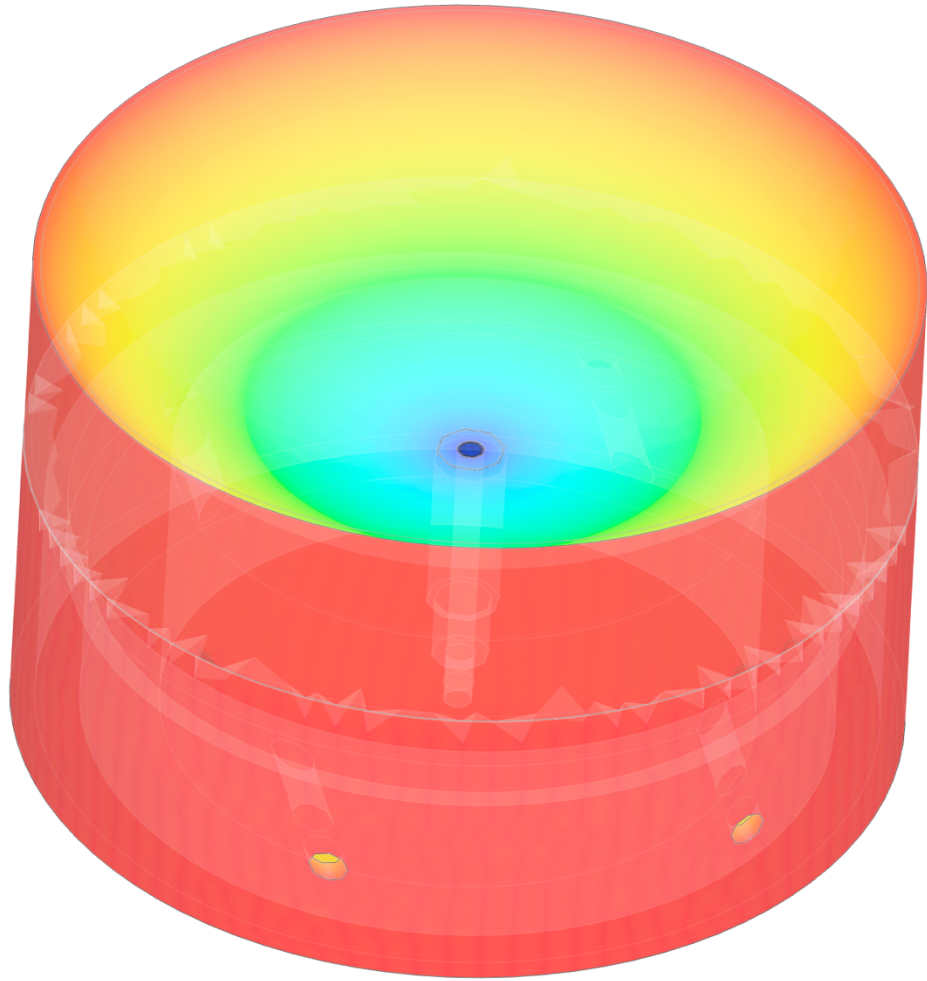


Figure 72: The gradual fading of vibration of the Upper Head.

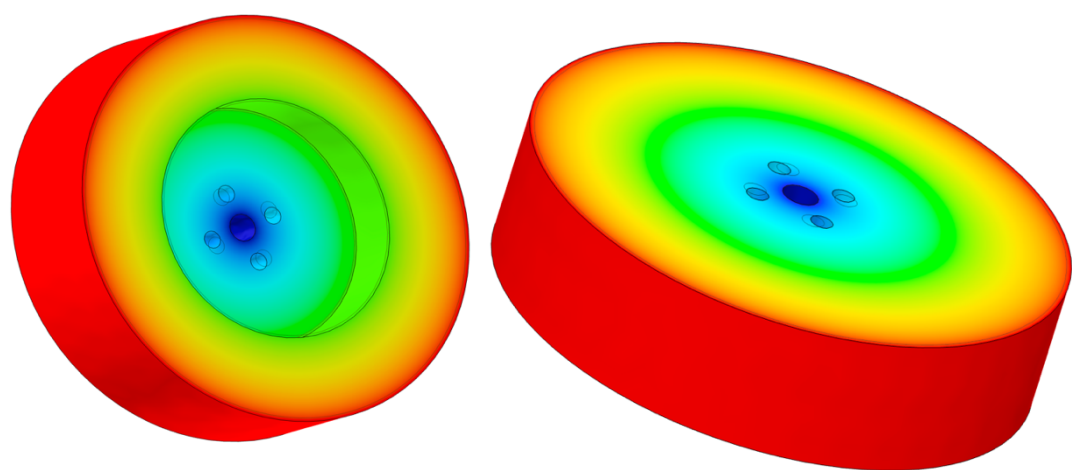


Figure 73:Shows the complete vibration distribution radially.

8.5.3 Air flow analysis

Airflow analysis provides critical insight into how air should be directed toward the head of the base structure to achieve optimal performance. This analysis is conducted to determine the most effective direction for delivering airflow in order to properly support and stabilize the upper section of the system. As shown in **Figure 74**, if the airflow is applied at an oblique angle, it may lead to instability and potential failure of the structure due to uneven force distribution. Therefore, it is essential that the air be directed perpendicularly to the surface of the hemisphere. This ensures uniform pressure distribution, enhancing both the balance and effectiveness of the air bearing system.

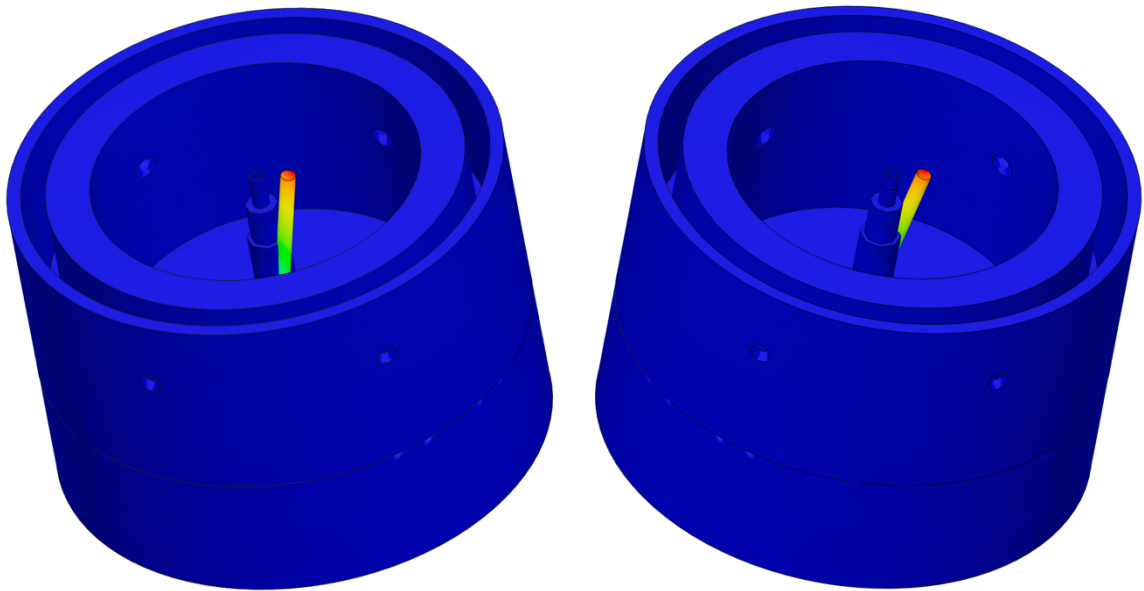


Figure 74: Air flow analysis

Chapter 9: Air bearing with Process and integration

9.1 Working

An air bearing table is a precision instrument that operates on the principle of fluid film lubrication, where a thin layer of pressurized air forms a frictionless interface between two surfaces. This simulates the near-zero friction and weightlessness conditions of outer space. By introducing compressed air between the bearing surface and a satellite mock-up, the system creates an air cushion that lifts and supports the payload, enabling free movement in one or more rotational or translational degrees of freedom. This setup effectively replicates the free-floating conditions encountered in orbit, making it ideal for testing Attitude Determination and Control Systems (ADCS), particularly in small satellites like CubeSats. The operating principle aligns with Newton's First Law of Motion, where an object remains in its state of motion unless acted upon by an external

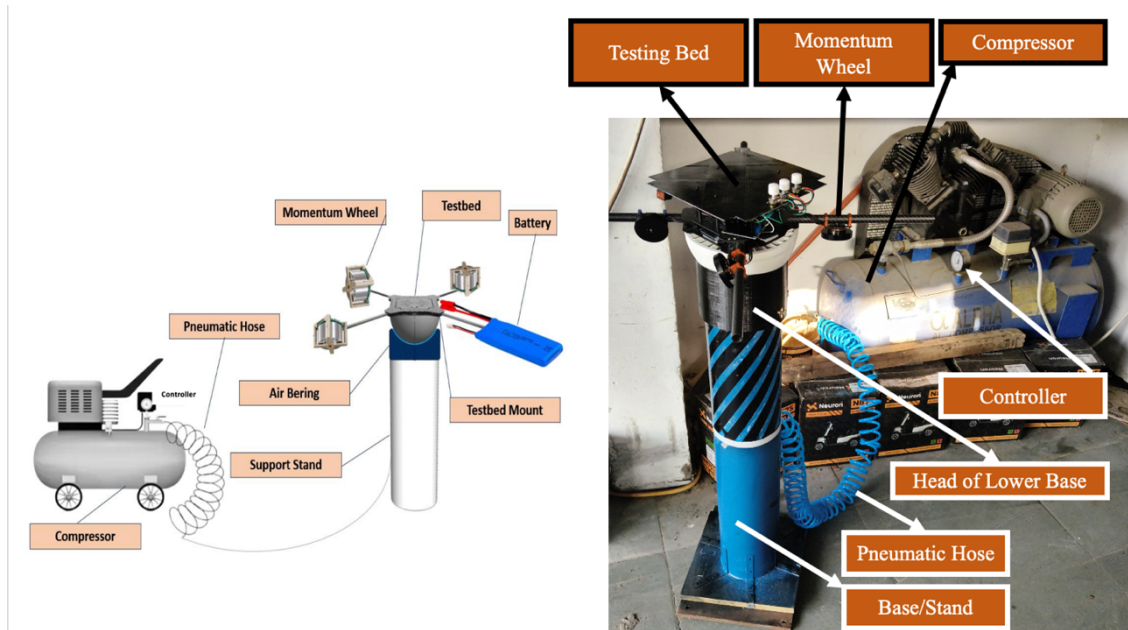


Figure 75:Image of proposed design and Actual model

force. With friction nearly eliminated, motion in the test setup results purely from internal actuators such as reaction wheels, magnetorquers, or other ADCS components. The test article, mounted on a hemispherical or planar bearing surface, can be evaluated for critical parameters like centre of gravity alignment, torque response, and disturbance rejection. Components such as Inertial Measurement Units (IMUs) and external sensors are used to track and assess the satellite's behaviour in response to simulated control inputs. This comprehensive evaluation allows engineers to refine control algorithms,

verify system balance, and enhance overall performance, ensuring mission reliability before launch.

9.2 Manufacturing Process

The complete manufacturing is a adaptive manufacturing approach, as while doing the project there was some limited resource, I was supposed to work with the resource provided so, I wanted to have this approach to get the project successfully completed. In the upcoming section I will be revisiting each and every portion of the manufacturing and analysis dine. I will also provide the design approach and design adaptive modifications which actually been used in this project.

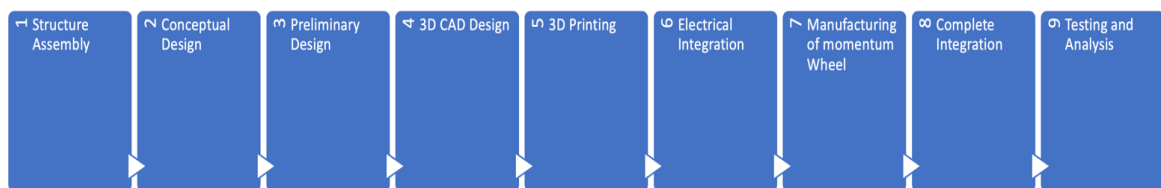


Figure 76: Complete Manufacturing Process

9.2.1 Electrical Integration

The Electrical components that are used are already been discussed earlier. In this section we will go through the connections done with the circuits used and related salient features.

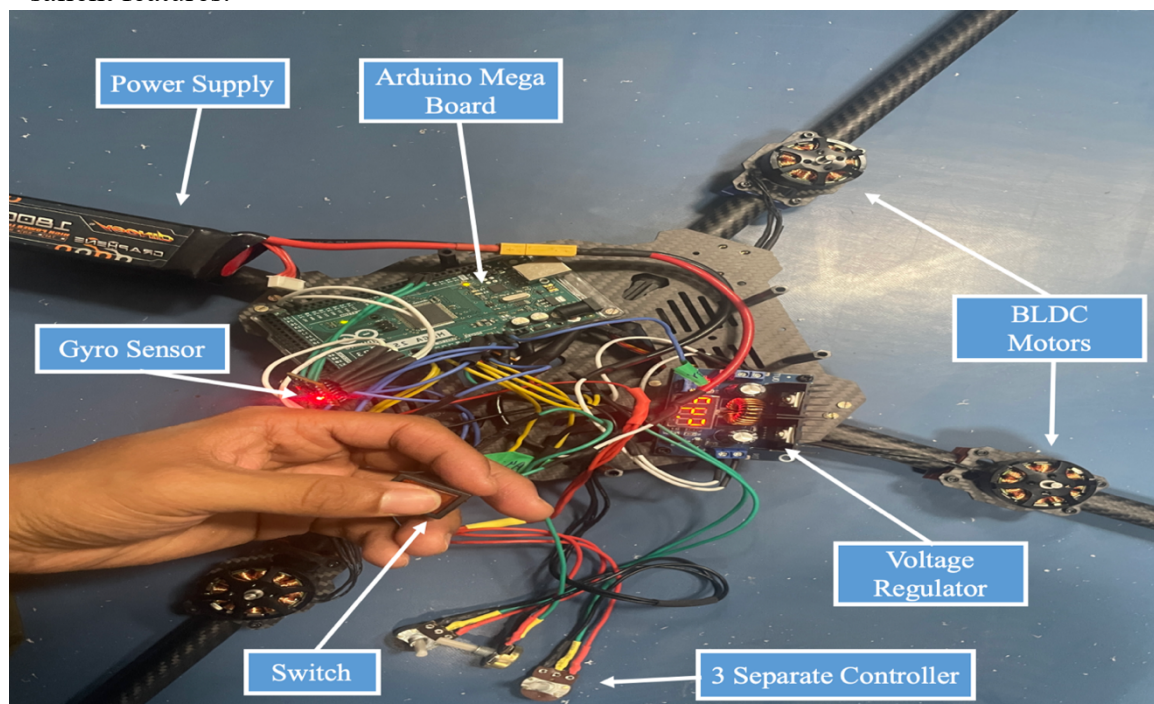


Figure 77: Complete electrical integration with proper connections

9.2.1.1 Algorithm

The designed circuit integrates an Arduino Mega microcontroller with several components to form a functional and portable motion sensing and control system. Power is supplied by a 12V rechargeable battery, which is regulated through a DC-DC buck converter. The converter steps down the voltage to a stable 9V output, which is fed to the VIN and GND pins of the Arduino Mega, ensuring safe and reliable power delivery. Three potentiometers are connected to the Arduino as analog input devices, with each wiper connected to analog pins A0, A1, and A2 respectively, while the other two terminals are connected to the 5V and GND lines. These potentiometers allow for manual input control—potentially simulating user-defined speed, orientation, or other variable parameters. An MPU6050 sensor module is included to provide real-time motion data; it connects to the Arduino via I2C communication using the SDA (pin 20) and SCL (pin 21) lines, with power supplied from the 5V pin. A push-button switch is also included, wired between digital pin 7 and ground, with a pull-down resistor to ensure accurate digital readings. This switch serves as a manual control interface, such as enabling or disabling motion capture or activating specific actions in the system. All components share a common ground to maintain electrical integrity. The integration of these elements allows the Arduino Mega to gather input from the potentiometers and MPU6050, process it, and respond accordingly, forming the basis for real-time motion analysis and control in a satellite motion simulation or similar application.

9.2.2 3D printing

The components of the satellite testbed were fabricated and assembled in large part thanks to 3D printing. Fused Deposition Modelling (FDM) technology was used to custom-design and manufacture a number of crucial structural components, including the upper dome, motor mounts, electronic integration housings, and support fixtures. Rapid prototyping, iterative improvement, and economical production of intricate geometries that would be challenging or costly to produce with traditional machining were made possible by this method. Furthermore, lightweight construction was made possible by 3D-printed parts that still



Figure 78: Lower hemispherical part being printed in 3D printing Machine.

had enough mechanical strength for testing. Easy access to internal electronics and streamlined part replacement or upgrades throughout the development cycle were also made possible by the modular design made possible by 3D printing. By leveraging 3D printing, complex component geometries could be realized with minimal material wastage, rapid design iterations became feasible, and custom parts could be tailored to specific subsystem requirements. This not only lowered production costs but also enabled faster assembly and easier customization—critical factors in research and development environments where adaptability is key.

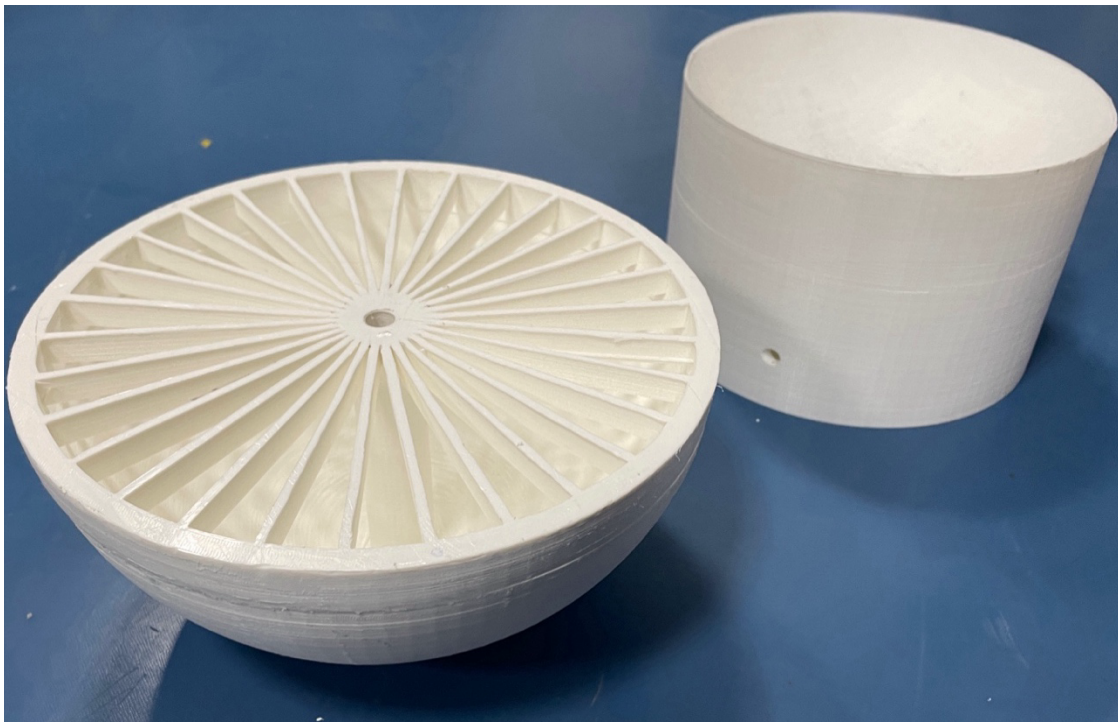


Figure 79: Complete task of (1) Lower hemispherical Part and (2) Head of the lower base.

9.2.3 Mechanical Manufacturing

The mechanical manufacturing of the momentum wheel involved a series of conventional machining operations, including turning, cutting, boring, and drilling. A detailed description of the process is provided below, in figure 81.

Initially, the raw material—a circular chunk of mild steel—was selected for its favourable machinability and strength characteristics. The material was first



Figure 80: Complete Machined Momentum Wheel.

securely mounted on a lathe machine, where turning operations were performed to achieve the required outer diameter of the momentum wheel. Following this, the material was cut to a length of approximately 17 mm, slightly greater than the final required thickness of 15 mm, to allow sufficient material for facing operations.

Facing was then carried out to precisely achieve the final thickness specification and to ensure a flat and smooth surface finish. After facing, a boring operation was performed to create an internal bore of 8 mm in diameter, providing the necessary internal clearance for the motor shaft or other fittings. Subsequently, a central drilling operation was conducted to create a 4 mm diameter hole at the centre of the wheel. In addition, four peripheral holes, each with a diameter of 3 mm, were drilled symmetrically around the centre. These holes were specifically designed to facilitate the secure attachment of the momentum wheel to the motor assembly.

Each machining step was executed with careful measurement and precision to ensure that the final component met both dimensional and functional requirements, contributing to the overall performance and reliability of the system.

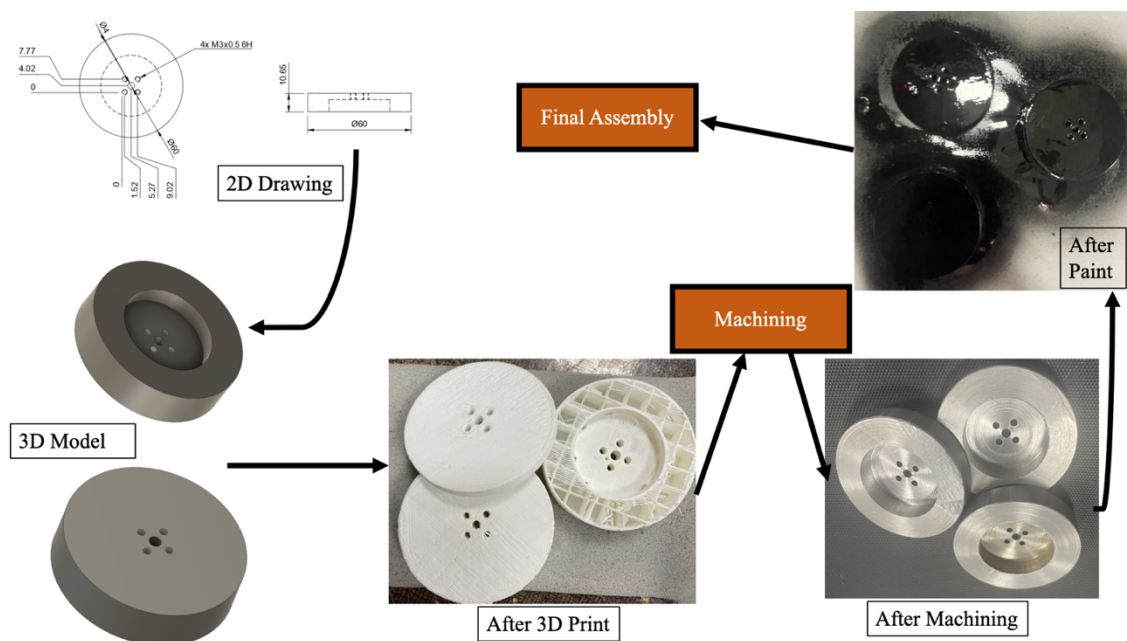


Figure 81: Complete line of production of the momentum wheel.

The final product obtained was a momentum wheel which was made in workshop and the consecutive machining was done in the sequence given the figure below.



Figure 82: Complete line of action of Machining

9.2.4 Base Stand Design and Integration

The base was specifically designed to accommodate the height constraints within the Helmholtz cage, ensuring that the overall setup remained compact and stable. To achieve this, L-brackets were employed to attach the structural elements to a wooden

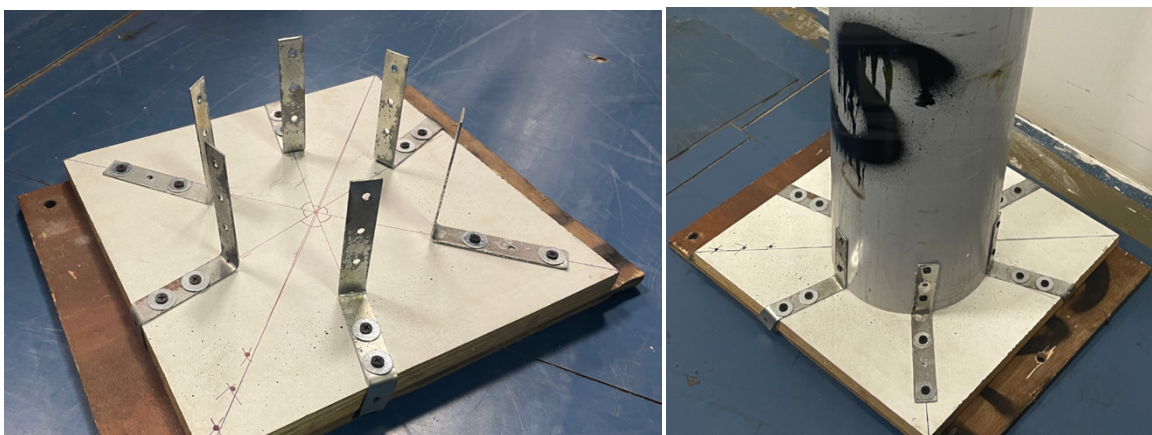


Figure 83: On left: L-bracket are placed, equally spaced. on right side: The cylindrical hollow section is placed and fixed with the L-bracket.

base. A total of six L-brackets were fixed symmetrically, each positioned at an angle of 60 degrees, providing a stable and evenly distributed support structure. High-density PVC pipes were then mounted onto the L-brackets, forming the primary vertical supports, as illustrated in the image below. Following the installation of the PVC pipes,

the custom 3D-printed parts were precisely aligned and securely fixed onto the assembly, completing the structural framework. This design approach ensured both mechanical stability and compatibility with the dimensions and operational requirements of the Helmholtz cage.

9.3 Painting

Painting is a vital part of the final fabrication stage, not merely for aesthetics but primarily for functional protection. In mechanical and aerospace applications—such as the development of satellite testbeds and air-bearing platforms—metal components are frequently exposed to environmental factors such as humidity, dust, and varying temperatures, which can accelerate corrosion and rust formation. Applying a suitable paint or surface coating creates a protective barrier that shields the substrate from oxidation and chemical degradation. Moreover, the choice of paint can also aid in thermal control, particularly in space-related components where temperature management is critical. In this project, the painted surfaces not only enhance the overall appearance of the testbed but also ensure structural longevity, reliability, and maintenance ease. Anti-static or non-reflective coatings may also be considered in sensitive sensor regions to minimize optical interference or electromagnetic disturbances.



Figure 84: Stand being printed in blue and black

9.4 Innovative Approach

Several design approaches have been adopted to reduce the overall cost while simultaneously enhancing the functionality and usability of the air bearing system. One key modification involves the optimization of the air transfer channel leading to the orifice opening at the base head. This redesign ensures efficient and stable air delivery, thereby improving the system's levitation performance and reliability. In addition, carbon fibre has been strategically incorporated into the structure to improve both strength and weight efficiency. A carbon fibre holder for the momentum wheel has been introduced to reduce mass while maintaining mechanical durability. Similarly, the carbon fibre base plate in the upper dome section, which houses the electrical integration block, has been

implemented to ensure structural rigidity and to support proper electrical component placement. These material and design optimizations not only contribute to better dynamic balance and vibration resistance but also enhance the overall performance and scalability of the air bearing platform for future satellite testing applications.

The airflow channel, as shown in figure 87, is another innovation that will provide the easy, effective and low-cost connectivity to the compressor. This is easy to fit in the upper head of the base and also to the compressor. It also provide an adjustable features in the base.

Finally the octopus connector, as shown in figure 85, allow us to connect the esc parallelly to get the required voltage and Current.

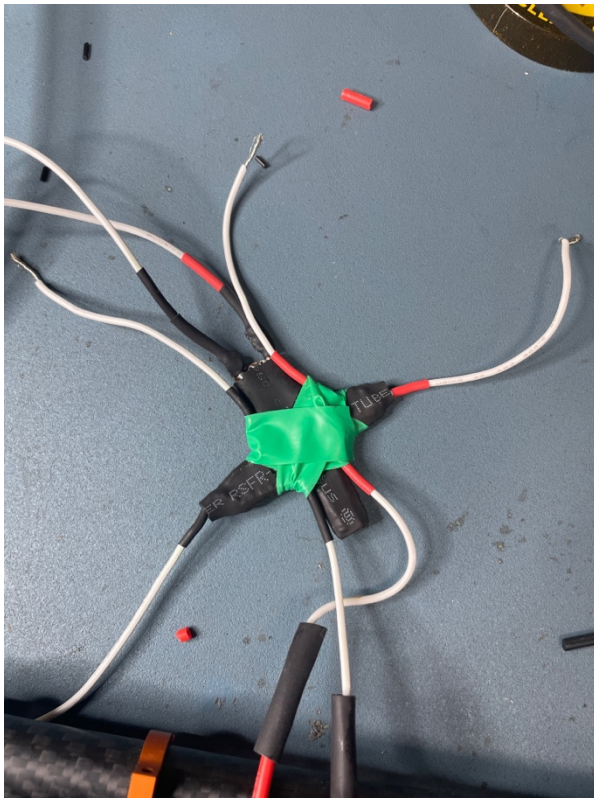


Figure 85: Octopus connector for connection ESC.



Figure 86: Air delivery channel

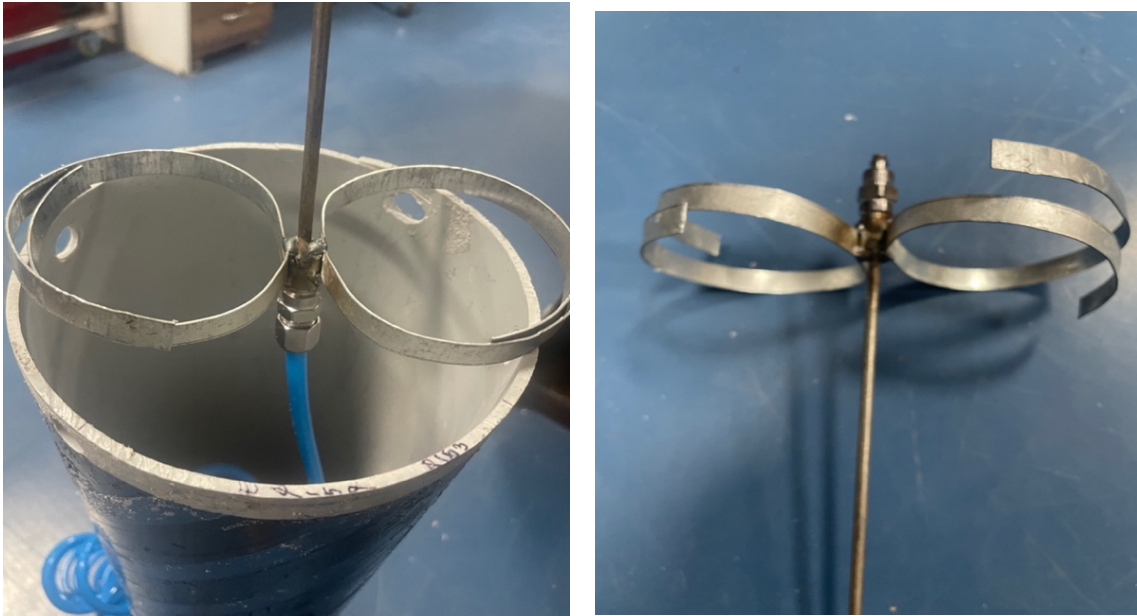


Figure 87: Air delivery channel being connected to the air pipe channel.

9.5 Challenges

Without challenges, no project feels truly rewarding—and this project was no exception. One of the primary challenges lay in the design phase, where creating each part with precise dimensions and maintaining uniform clearances for proper fitting demanded a high level of accuracy and attention to detail. The iterative nature of the design process, along with the need to constantly cross-reference component dimensions, added to the complexity.

The next significant challenge was 3D printing. Although additive manufacturing offers design flexibility, the process required constant monitoring to ensure print quality and avoid failures, especially for components with intricate geometries. Precision remained a top priority throughout the printing process.

Machining the momentum wheel posed another set of difficulties. After the three workpieces were extracted from the main raw mild steel stock, they underwent multiple machining operations. Achieving tight tolerances during turning, boring, and drilling was essential for ensuring dynamic balance and performance.

Another major challenge was the manufacturing of the base stand. Initially, the bottom head was planned to be made entirely of mild steel. However, due to its complex shape and the limitations of available manufacturing resources, this approach proved impractical. This prompted a redesign. A creative and cost-effective solution was devised: to deliver compressed air through a mild steel pipe while fabricating the remaining structure using PLA via 3D printing. This not only simplified the manufacturing process but also significantly reduced the overall production cost while maintaining the required functionality.

Chapter 10: Working Analysis

10.1 Complete Integration

All the subsystems — including the electrical components, machined mechanical parts, and aerodynamic structures — were carefully integrated to form a complete air bearing system. After the successful integration of these subsystems, the entire system underwent multiple rounds of testing and analysis. These tests were essential to ensure proper weight distribution, achieve balance, and precisely align the centre of pressure (CoP) with the centre of gravity (CoG) of the assembled headstock. Correct alignment was critical for maintaining stability and achieving accurate dynamic performance. Following the mechanical validation, an Inertial Measurement Unit (IMU) sensor was strategically placed above the testing bed. The IMU provided crucial feedback on the system's Attitude Determination and Control System (ADCS) parameters, enabling the evaluation and implementation of 3-axis control for the entire air bearing setup. This comprehensive testing and sensor integration ensured that the system met its design objectives and performed reliably under operational conditions.

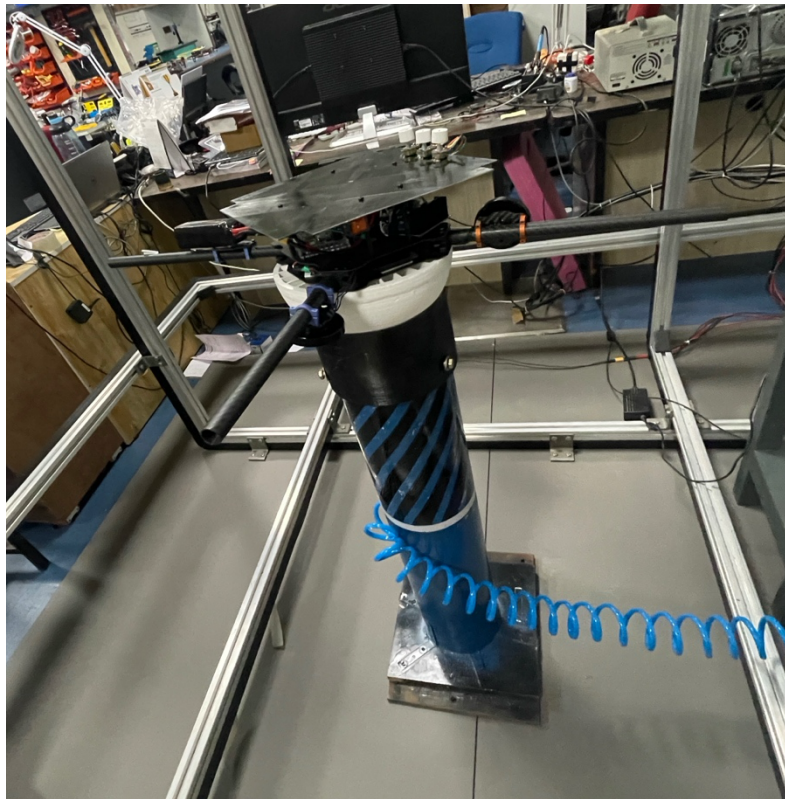


Figure 88: Exactly at the centre of Helmholtz Cage.

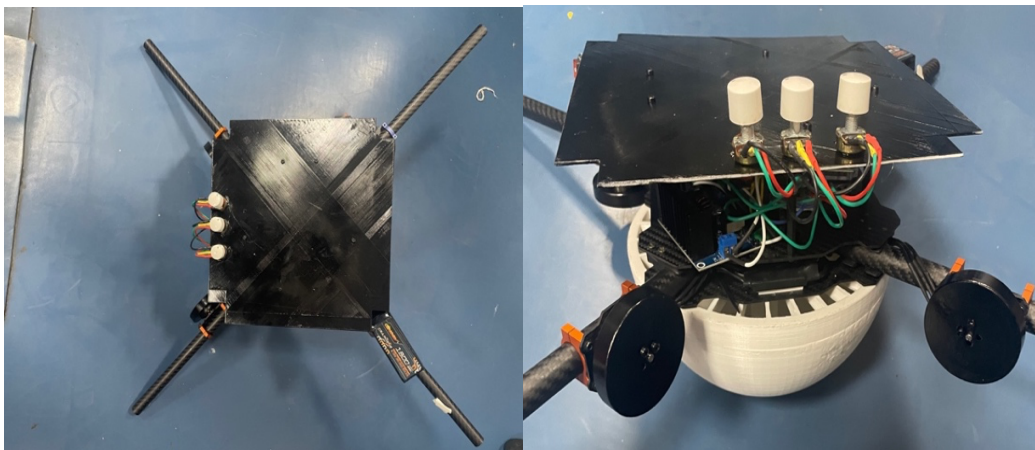


Figure 89: Top view and Side view of the upper part of the system.

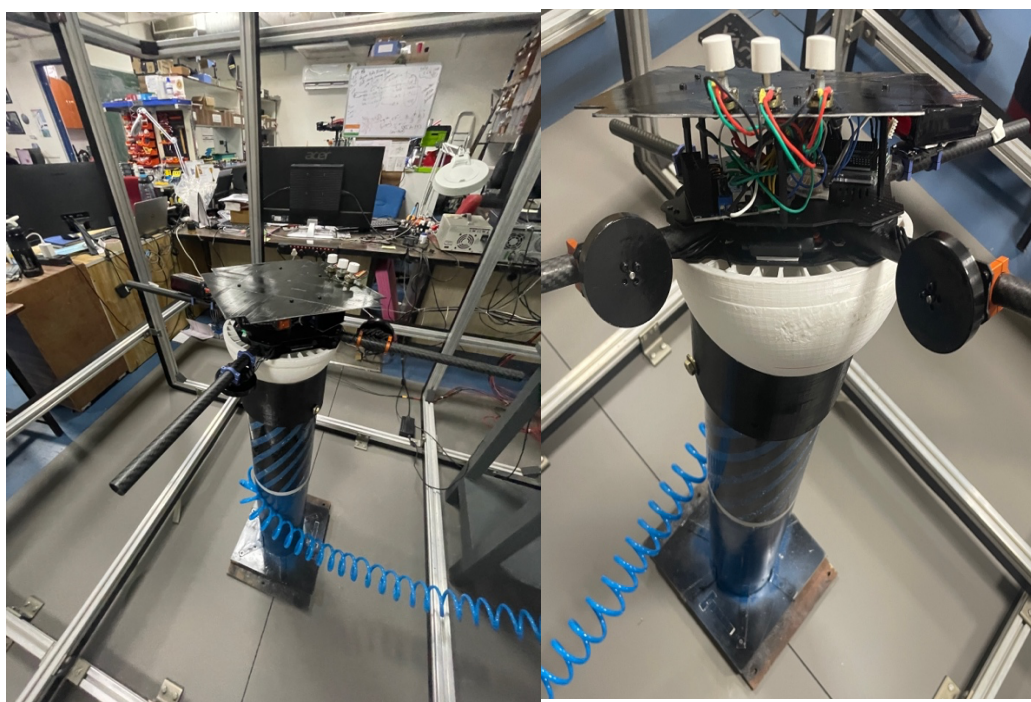


Figure 90: Complete Structure inside the Helmholtz Cage.

10.2 Operational Guidelines and Control Setup

To initiate the electrical subsystem of the air bearing-based ADCS testbed, a dedicated power switch is provided below the satellite's working platform. This switch energizes the onboard microcontroller and associated electronic components, triggering the execution of the embedded control program.

The testbed features three individual control knobs, as shown in the figure 91, each corresponding to one of the satellite's three rotational axes—pitch, roll, and yaw. These knobs allow for independent adjustment and simulation of rotational motion in each direction, facilitating comprehensive ADCS testing and calibration.

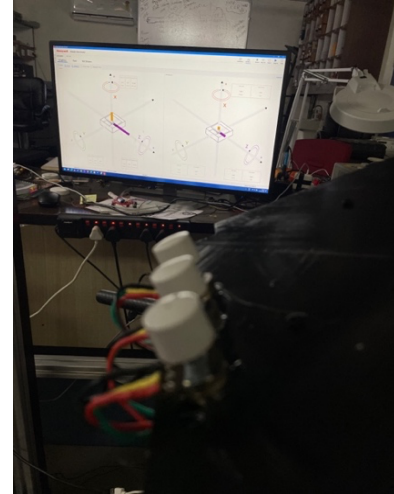


Figure 91: Direct computer feed from the sensor.

Important operational safety instructions must be followed during use. It is crucial to ensure that all three control knobs are set to their neutral (zero) position before powering the system ON or OFF as shown in figure 89. This prevents abrupt voltage changes or unexpected motion, which could damage sensitive components or destabilize the test setup.

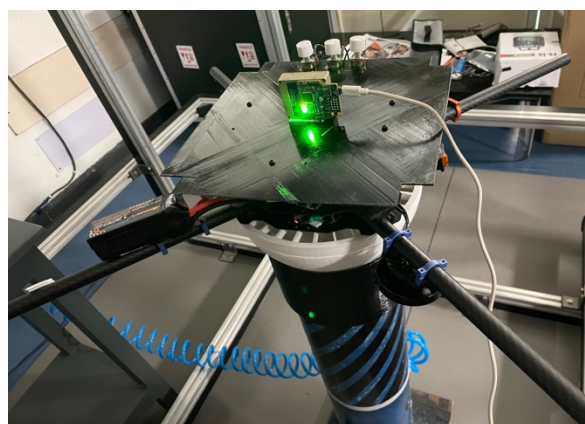
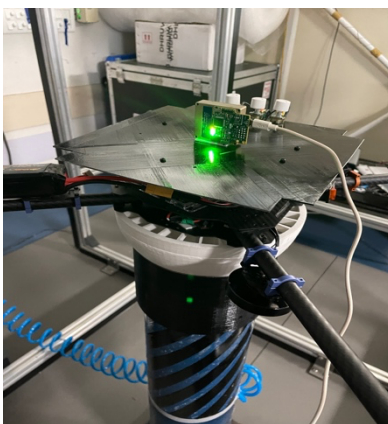


Figure 92: IMU mount above the testing bed.

Additionally, the system is designed to operate safely within a voltage range below 15.2 volts. Exceeding this limit poses a significant risk of Electronic Speed Controller (ESC) failure or permanent damage, and must be strictly avoided during operation.

10.3 Working Analysis

The whole Satellite bed is now ready for further analysis and this is done by keeping inside Helmholtz cage.

The following are the results of the different angle manoeuvre inside the Helmholtz cage:

10.3.1 IMU Showing changes in all the direction

The IMU sensor control is analysed by the change in the velocity, acceleration, angular velocity and change in angle where the visualization is shown in figure 92, figure 93 and figure 94.

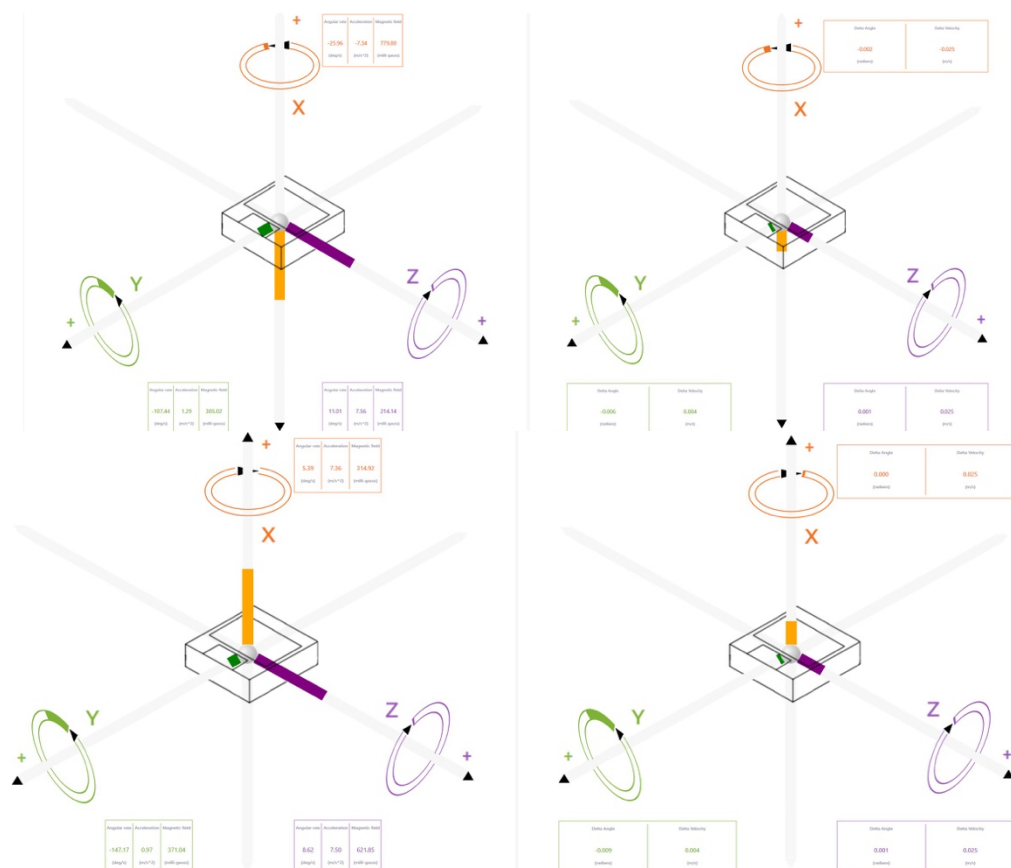


Figure 93: Visualization along the X-Axis

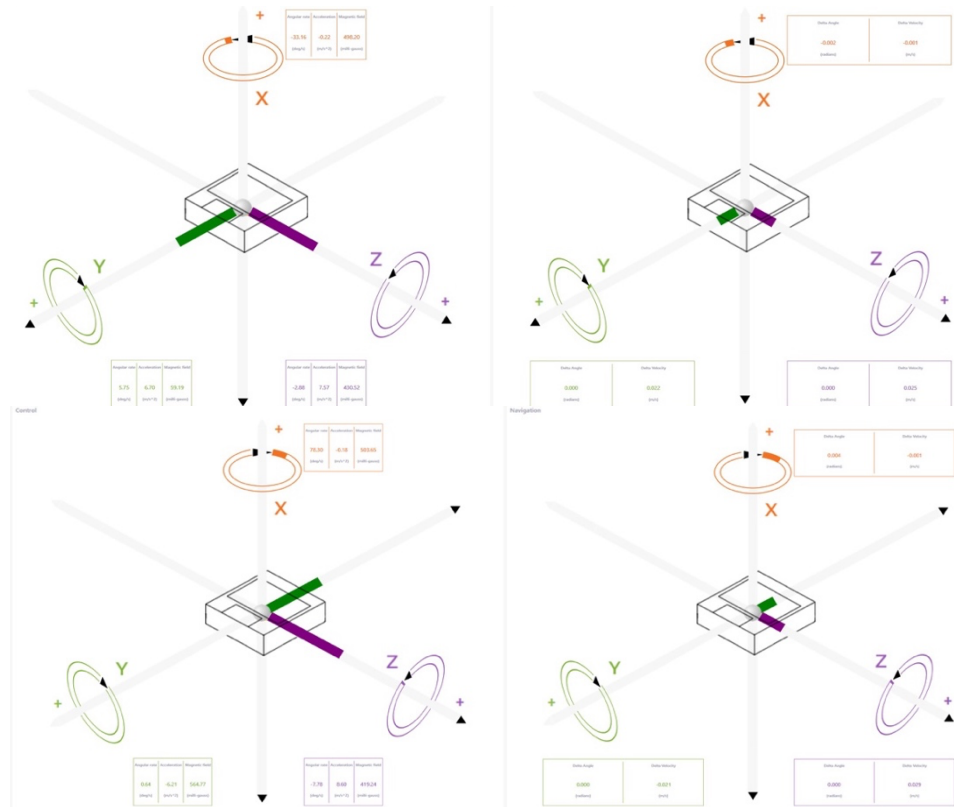


Figure 94: Visualization along the Y-Axis

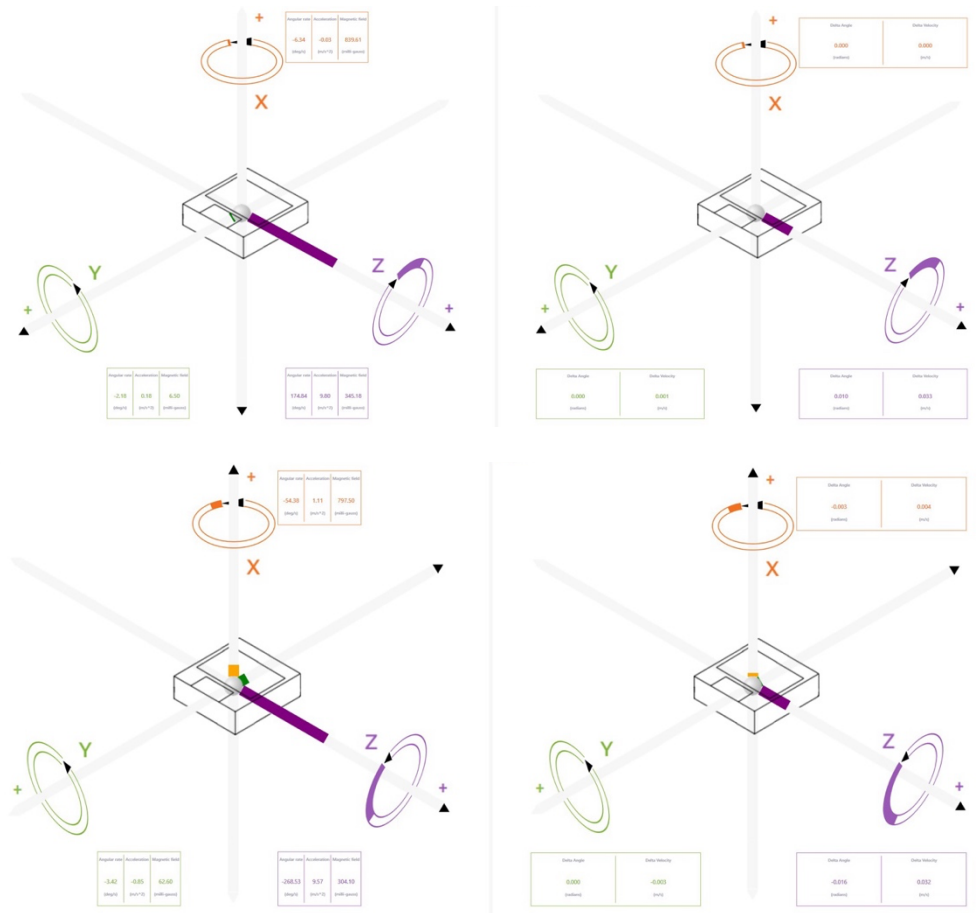


Figure 95: Visualization along the Z-Axis

10.3.2 Random Movement

A random test was done by moving the upper part and the following data was recorder.

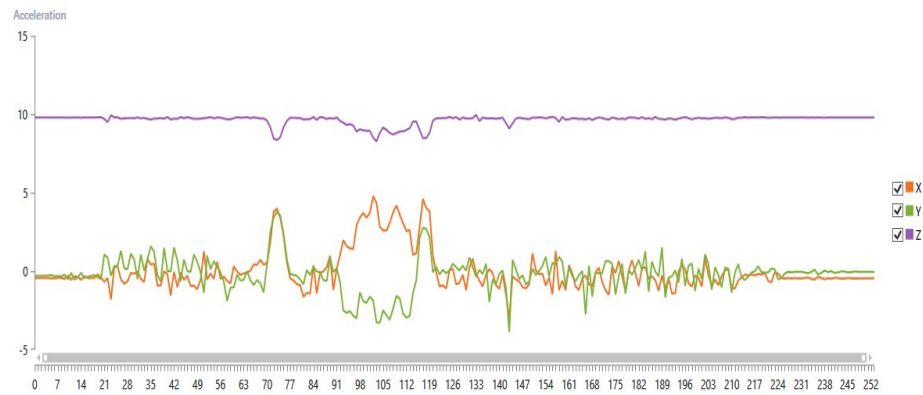


Figure 96: The acceleration in all 3 direction.

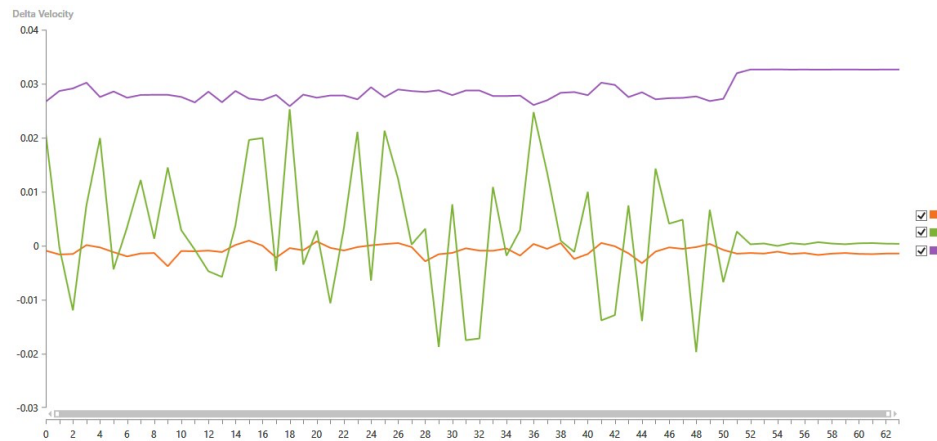


Figure 97: The delta velocity value in all the direction with x axis as the time step.

10.3.3 Fast and Slow Manoeuvring

The following curve is generated by fast and slow manoeuvring in the testing bed. The reading is taken directly from the H-Guide interface if the IMU Sensor's interface.

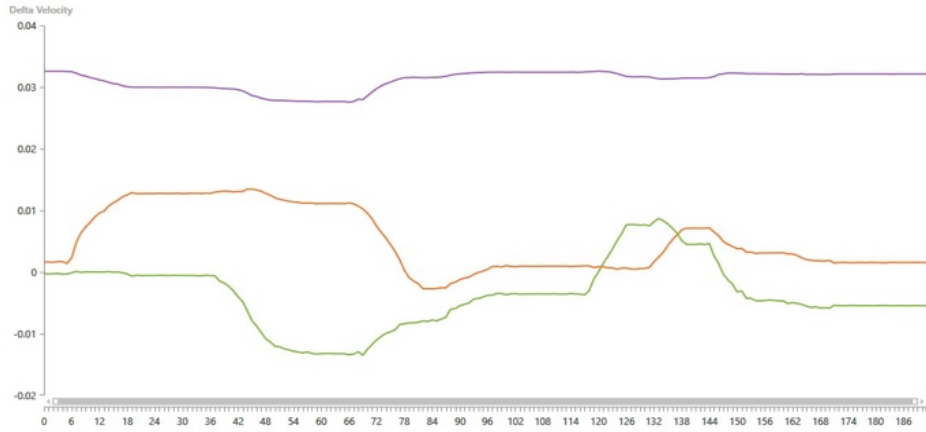


Figure 98:Delta velocity in slow manoeuvring in all three axis with x axis as the time step.

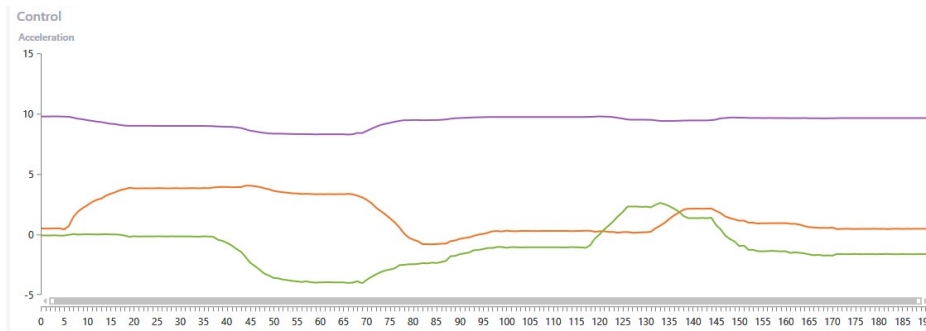


Figure 99:Acceleration in slow manoeuvring in all three axis with x axis as the time step.

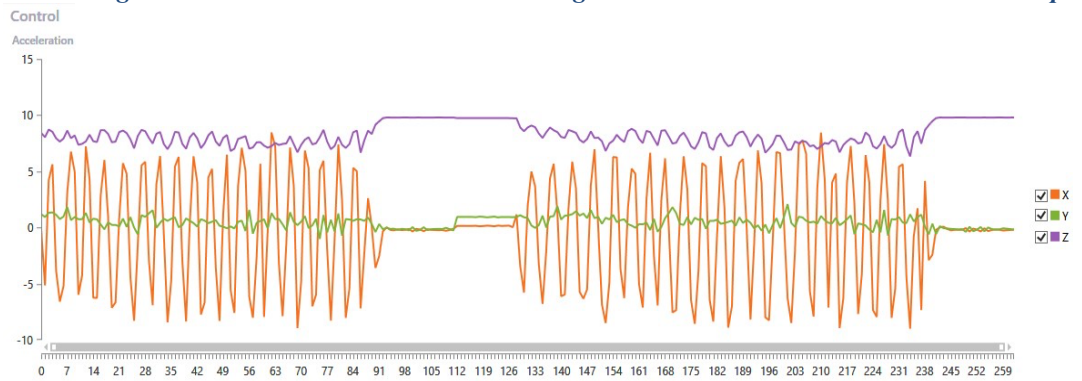


Figure 100:Acceleration in fast manoeuvring at all three axis with x axis as the time step

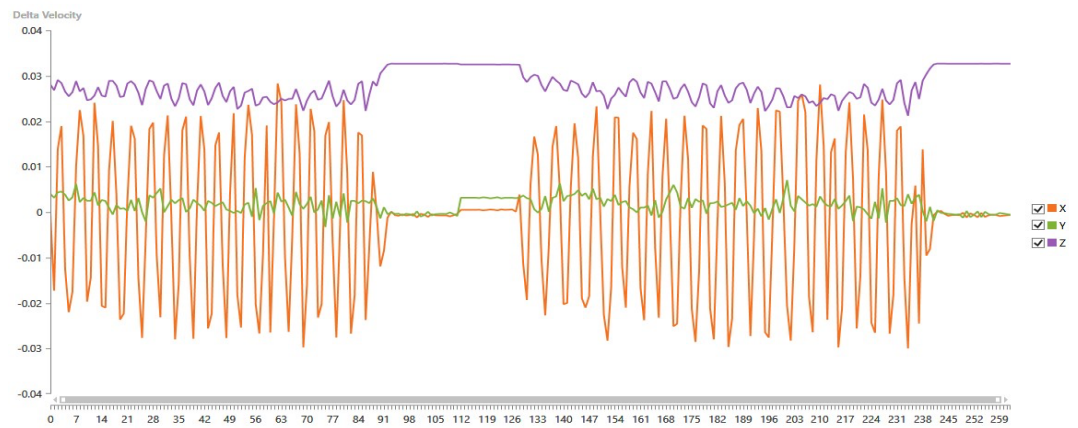


Figure 101:Delta velocity in fast manoeuvring at all three axis with x axis as the time step.

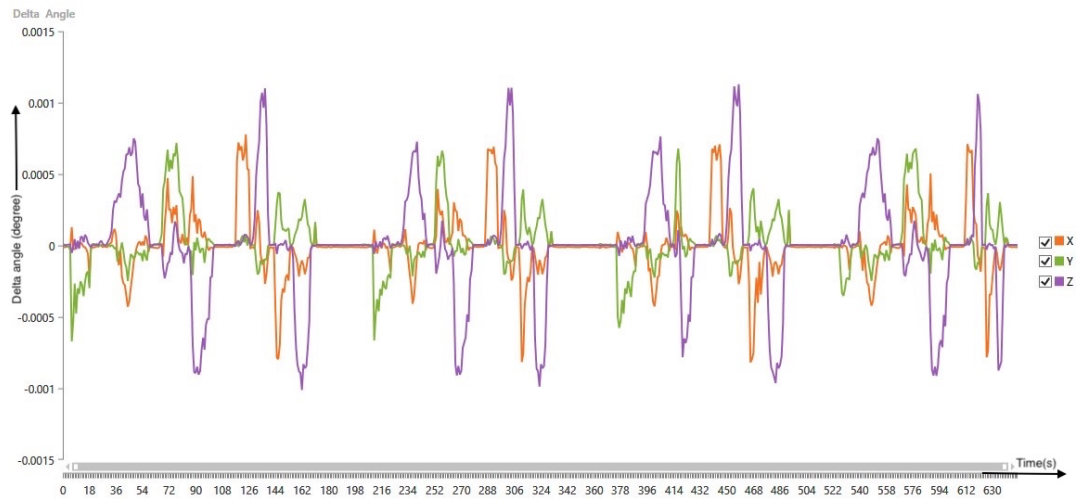


Figure 102:Delta angle in automated algorithm

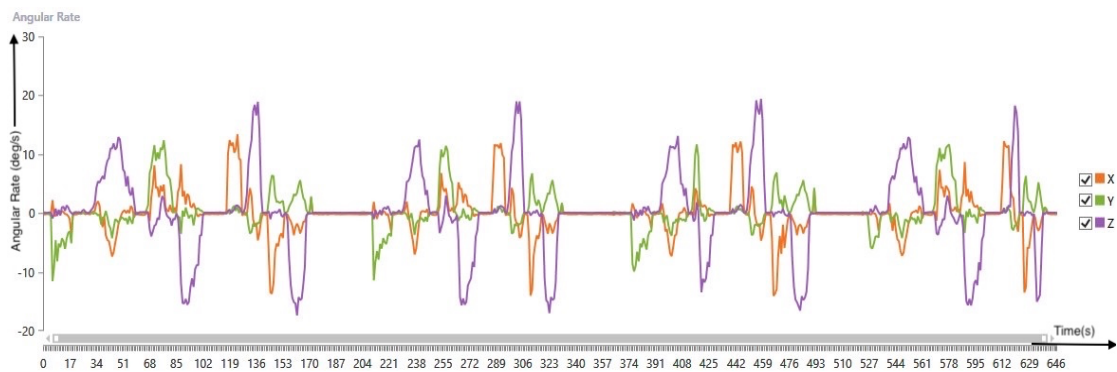


Figure 103:Angular rate in automated algorithm

10.3.4 Limitations

All instruments or system comes with some limitations, similarly SHOURYA also has some limitations as well. Although the SHOURYA is fully functional it will surely have some limitations beyond which it won't be effective. If the compressed air of 140 psi is given it can only lift weight of not more that 2.45 kg. And for 300 psi it can lift up to 3.20 kg excluding the existing base weight of the testing platform. And also we can only maneuverer up to ± 60 degree in all three axis.

Chapter 11: Conclusion and Future Scope

This thesis presented the design, simulation, and manufacturing of an Attitude Determination and Control System (ADCS) test platform for small-scale satellite systems, with a primary focus on utilizing an air bearing table to replicate microgravity-like conditions. The system was developed from scratch, with all mechanical components such as the momentum wheel, upper hemispherical dome, and base head designed in-house, fabricated using a combination of traditional machining and additive manufacturing techniques with pure mathematical and rigorous simulations.

The project successfully integrated multiple subsystems—electrical, mechanical, and aerodynamic—into a unified setup capable of simulating 3-axis satellite orientation. The use of an Electronic Speed Controller (ESC) to drive Brushless DC (BLDC) motors, paired with a microcontroller and potentiometer-based interface, allowed for precise control of satellite orientation. An Inertial Measurement Unit (IMU) mounted on the headstock provided real-time data for verifying control algorithms and orientation behaviour.

Several technical challenges were encountered, including precise design for fitting tolerances, monitoring 3D printing processes for structural parts, and achieving tight tolerances in momentum wheel machining. Design iteration and innovation, such as replacing complex metal structures with hybrid PLA and carbon fibre elements, played a critical role in overcoming these limitations. This not only reduced overall cost and fabrication time but also improved design flexibility.

The integration of 3D printing (additive manufacturing) enabled the rapid prototyping of custom parts, allowing the testbed to be easily modified or upgraded as required. This adaptability was instrumental in supporting a low-cost, yet robust and functionally accurate ADCS platform. The testbed demonstrates the viability of using air bearings and lightweight construction to emulate the dynamics of satellite attitude control in a controlled environment.

Through simulation and experimental validation, key performance aspects such as torque response, stability, and 3-axis control were successfully demonstrated. The

system effectively mimicked the frictionless conditions of space using the principle of fluid film lubrication through a cushion of pressurized air beneath the hemispherical base. This allowed for real-world testing of control strategies and component integration before real deployment in space-based applications.

Technically and functionally, the development and integration of a miniature Attitude Determination and Control System (ADCS) tested on an air bearing platform has shown promise. The project journey provided a full development cycle experience, encompassing conceptual design, simulation, prototyping, and final testing. Every subsystem was designed from the ground up, evaluated for viability (using structural and acoustic analysis), and optimized for effective real-world performance. These subsystems included mechanical (momentum wheel, base stand), electrical (ESC, IMU, sensors), and control (PWM signals, software logic).

The momentum wheel was successfully fabricated using conventional machining methods, creative structural alterations were made using carbon fibre and 3D-printed parts to lower costs and complexity, and air bearing systems were used to replicate microgravity-like conditions.

To guarantee correct balance, centre of mass alignment, and low vibrational disturbances, the integration of these components was done with great care. The Inertial Measurement Unit's (IMU) real-time feedback verified the system's expected behaviour and the efficacy of the control strategies put in place.

The are enormous scope of the air-bearing table, not only limited to the following Area:

Sl. No.	Future Area	Description	Potential Impact
1	Advanced Control Algorithms	Implementation of PID, Kalman Filter, MPC, fuzzy logic, etc.	Increases precision, robustness, and response quality.
2	Hybrid Actuation Systems	Inclusion of reaction wheels, magnetorquers, and CMGs	Simulates real satellite dynamics more accurately.
3	Enhanced Air Bearing Platform	Full 3-axis rotation, higher load capacity, magnetic levitation	Allows comprehensive dynamic testing and greater realism.

4	Real-Time Telemetry & Communication	Wireless modules for live data transfer and remote control	Improves usability and monitoring during tests.
5	Autonomous Calibration	Automated IMU bias adjustment, self-balancing, and gain tuning	Enhances accuracy and reduces manual effort.
6	Environmental Simulation & Disturbance	Simulate thermal, magnetic, and dynamic disturbances	Prepares system for real space-like conditions.
7	Scalability for CubeSat/Nanosat Systems	Adapting system for small satellite form factors	Useful for academia and low-budget mission prototyping.
8	Integration of AI and ML	Predictive diagnostics, reinforcement learning for control tuning	Enables intelligent, adaptive, and autonomous behaviour.

Table 20: Table for future aspect of my project.

The next immediate work that could be done by automation and testing different modes of Attitude control and this will mark the beginning of new chapter of the advancement of Attitude Determination and Control System.

APPENDIX-A

Software and Simulation Tools Used

This appendix provides a comprehensive overview of the software environments and tools utilized throughout the research, design, simulation, testing, and integration phases of the Attitude Determination and Control System (ADCS) for a mini-satellite in Low Earth Orbit (LEO). Each tool played a vital role in achieving specific technical objectives, from 3D design and simulation to sensor calibration and control implementation.

A.1 MATLAB & Simulink

Purpose: MATLAB and Simulink served as the primary environments for theoretical modelling, system simulation, and control algorithm design.

Key Features and Use Cases:

Aerospace Toolbox:

Simulated satellite attitude dynamics, calculated orbital elements, and provided a framework for validating control behaviour under LEO constraints.

Simulink Models:

Developed time-domain block diagrams of the ADCS using IMU sensor inputs.

Modelled and tuned attitude control loops including Kalman Filter-based bias correction.

Implemented real-time simulations of gyro bias estimation under different sampling rates (e.g., 10 Hz vs 40 Hz).

Visualized error convergence and heading deviation over time.

Geomagnetic Modelling:

Used IGRF and WMM models to simulate the Earth's magnetic field as a function of satellite position.

Plotted theoretical vs experimental magnetic field readings in X, Y, and Z directions.

Conducted altitude-based magnetic field comparison to validate magnetometer performance.

Data Visualization:

Created 2D and 3D plots of orbital paths, magnetic vectors, and error histograms.

Generated histograms and heat maps for error propagation analysis.

Official Download Link:

 <https://www.mathworks.com/downloads/>

A.2 Fusion 360

Purpose: Fusion 360 was used for 3D mechanical design, part assembly, basic simulations, and digital fabrication preparation of the air-bearing testbed and associated components.

Applications in the Project:**3D CAD Modelling:**

Designed the hemispherical air-bearing housing, momentum wheels, motor mounts, and base support brackets.

Verified alignment between air pipes, ESCs, and motor shafts within the assembly.

Assembly and Motion Studies:

Simulated rotational clearances and alignment for moving parts.

Verified space constraints before integration with the Helmholtz cage.

Fabrication-Ready Exports:

Converted 3D designs into STL files for 3D printing.

Generated STEP files for CNC machining.

Simulation Tools:

Basic stress analysis for momentum wheel under rotational loads.

Used airflow visualization in duct paths to ensure even distribution within the air-bearing structure.

Renderings and Visualization:

Created photorealistic renderings of the experimental setup for documentation.

Used exploded views to show inner mechanisms of the testbed.

Official Download Link:

 <https://www.autodesk.com/products/fusion-360/download>

A.3 Python Programming

Purpose: Python was extensively used for experimental data analysis, algorithm prototyping, sensor calibration, and custom plotting.

Modules and Implementation:**Data Analysis & Calibration:**

Analysed raw IMU data to detect noise, drift, and biases.

Applied low-pass filters and smoothing algorithms to time-series data.

Performed error modelling between theoretical and measured geomagnetic values.

Libraries Used:

NumPy/SciPy: Signal processing, numerical filtering, and polynomial fitting.

Pandas: Managed large datasets from CSV logs for experimental sessions.

Matplotlib/Seaborn: Generated line graphs, histograms, scatter plots for delta velocity, heading drift, and bias convergence.

SymPy: Symbolic computation for validating theoretical models.

Algorithm Testing:

Developed a simplified attitude estimation algorithm using TRIAD logic.

Simulated magnetic heading extraction using calibrated IMU data.

Modelled data fusion approaches combining magnetometer and gyroscope outputs.

Official Download Link (Python 3.x):

 <https://www.python.org/downloads/>

Package Installer (Pip):

 <https://pip.pypa.io/en/stable/installation/>

A.4 H-Guide Interface Software (for HG1120 IMU)

Purpose: Served as the main software platform for real-time interaction with the Honeywell HG1120 IMU, which was a core sensing device in the ADCS experiment.

Functional Capabilities:

Live Data Monitoring:

Tracked acceleration, angular velocity, and magnetic field strength in real-time along X, Y, and Z axes, and displayed dynamic vector changes during fast and slow manoeuvres.

Calibration and Alignment:

Provided tools to calibrate sensor offsets and correct for hard and soft iron errors.

Allowed heading estimation via internal Kalman filtering when enabled.

Logging and Export:

Logged time-stamped data into .CSV format for later analysis and synchronized data logging with experimental rotation on the air-bearing platform.


Integration in Experiments:

Used during turntable testing and 3-motor testing to validate sensor responsiveness.

Helped detect inconsistencies in magnetometer output due to electronic interference.

Download Source:

This software is proprietary and provided by **Honeywell upon purchase** of the HG1120 IMU. Request via Honeywell Support or official distributor.

 <https://aerospace.honeywell.com/en/products/sensors/inertial-measurement-units/hguide-hg1120>

A.5 Arduino IDE and Embedded C

Purpose: Enabled firmware development for control of actuators and integration of sensors in the momentum wheel system and experimental testbed.

Key Applications:

Motor Control:

Implemented PWM-based speed control for BLDC and brushed DC motors using L298N and ESC drivers.

Allowed direction reversal and speed ramp-up tests.

Sensor Integration:

Interfaced hall sensors for RPM measurement.

Monitored voltage and current using analog sensors for power optimization.

Closed-Loop Test Code:

Placeholder logic for closed-loop RPM control using IMU feedback and developed state switching based on sensor thresholds (e.g., $\text{RPM} > X \rightarrow \text{trigger maneuverer}$).

Testing Modes:

Used serial interface to send real-time commands and log motor behaviour.

Created safety cut-off logic to prevent overcurrent conditions.

Official Download Link:

 <https://www.arduino.cc/en/software>

A.6 Data Visualization and Post-Processing Tools

Tools Used:

MATLAB: For scientific plots, magnetic field analysis, Kalman filter output visualization.

Python (Matplotlib/Seaborn): For experimental result presentation, statistical comparison.

Fusion 360 Render: For technical visuals and part illustration in documentation.

Visualization Outputs:

Magnetic field intensity vs. orientation and altitude.

Delta velocity and acceleration profiles during manoeuvres.

APPENDIX-B

Future Work Considerations

This thesis establishes a foundational ADCS design and prototype demonstration. However, for real-world space applications, further advancements are necessary. The following sections detail future work directions along with references to similar research from leading institutions.

B.1 Extension to Full 3-Axis Momentum Wheel System

The current system demonstrates single-axis control. Full three-dimensional control requires a 3-axis momentum wheel assembly.

Similar Work:

- Stanford's **Quake Sat** CubeSat mission successfully demonstrated 3-axis attitude control using compact momentum wheels for ELF/VLF signal detection [44].
- University of Surrey's **Remove DEBRIS** satellite deployed a 3-axis control system for debris capture and net deployment experiments [45].
- University of Michigan's **CADRE CubeSat** showcased precision pointing capabilities using 3-axis reaction wheels designed for autonomous planetary terrain exploration [46].

B.2 Advanced Control Algorithms: PID & Model Predictive Control (MPC)

For enhanced performance, adaptive PID tuning and predictive control algorithms like MPC should be explored.

Similar Work:

- MIT's **SPHERES project** tested MPC algorithms for satellite formation flying and precision manoeuvres aboard the ISS [47].
- University of Tokyo's **Hodoyoshi-3** satellite implemented MPC for agile Earth observation and attitude control [48].

- Georgia Tech's **RECON Sat** developed hybrid PID-MPC control systems to maintain precision pointing under dynamic conditions [49].

B.3 Integration with CubeSat OBCs and Telemetry Systems

Future iterations must ensure seamless integration with onboard computers (OBCs) and telemetry systems for autonomous operations.

Similar Work:

- EPFL's **Swiss Cube** achieved integrated ADCS-OBC operations with telemetry feedback for CubeSat missions [50].
- Cal Poly's **CubeSat Program** developed modular ADCS interfaces with standardized communication protocols [51].
- India's **Stud Sat** project demonstrated telemetry and ADCS integration on a student-built picosatellite platform [52].

B.4 Environmental Testing: Vacuum, Thermal, Vibration, and Near-Space

Laboratory testing must be complemented with environmental validation to replicate space-like conditions.

Similar Work:

- University of Toronto's **NEMO-HD microsatellite** underwent extensive thermal-vacuum and vibration testing to ensure system reliability [53].
- Aalto University's **Aalto-1 CubeSat** used high-altitude balloon flights for near-space ADCS testing [54].
- CU Boulder's **Min XSS CubeSat** project successfully completed TVAC and vibration qualification to meet launch and orbital operation demands [55].

B.5 Emerging ADCS Technologies: AI, Sensor Fusion, Miniaturization

Next-generation CubeSat missions demand AI-driven adaptive control, advanced sensor fusion, and hardware miniaturization.

Similar Work:

- University of Colorado Boulder's **Fission Sat Program** is investigating AI-based reinforcement learning controllers for deep-space CubeSats [56].
- Imperial College London's **ICL Sat project** is developing advanced sensor fusion techniques using star trackers and IMUs [57].
- National University of Singapore's (NUS) **Satellite Research Lab** is focusing on low-cost, miniaturized ADCS solutions for nano-satellite missions [58].

B.6 Collaborations, Standardization & Open-source Platforms

Collaborating with open-source initiatives and adopting standardized CubeSat platforms will streamline ADCS development.

Similar Work:

- The **Libre Cube Initiative** (ESA-supported) promotes open-source ADCS subsystems and interfaces for educational and research satellites [59].
- NASA's **CubeSat Launch Initiative (CSLI)** provides standardized testing and deployment pathways for university-built CubeSats [60].
- Indian Institute of Space Science and Technology's **Swayam satellite** followed ISRO's CubeSat standards and validation protocols for communication payload deployment [61].

REFERENCES

- [1] Honeywell, "HG1120 MEMS Inertial Measurement Unit," 2024. [Online]. Available: <https://aerospace.honeywell.com/us/en/products-and-services/product/hardware-and-systems/sensors/hg1120-mems-inertial-measurement-unit>
- [2] Helmholtz Cage Diagram. (2024). Retrieved from https://uccubecats.github.io/images/HelmholtzCage/block_diagram.png
- [3] World Magnetic Model (WMM), AHRS Documentation, [Online]. Available: <https://ahrs.readthedocs.io/en/latest/wmm.html>
- [4] NCEI Geomagnetic Modelling Team and British Geological Survey. 2019. World Magnetic Model 2020. NOAA National Centres for Environmental Information. doi: 10.25921/11v3-da71
- [5] MATLAB. (2024). World Magnetic Model (wrlmagn). Retrieved from <https://in.mathworks.com/help/aerotbx/ug/wrlmagn.html>
- [6] International Geomagnetic Reference Field: the 13th generation, Alken, P., Thébault, E., Beggan, C.D. et al. International Geomagnetic Reference Field: the thirteenth generation. *Earth Planets Space* 73, 49 (2021). doi: 10.1186/s40623-020-01288-x
- [7] MATLAB. (2024). International Geomagnetic Reference Field (igrfmagn). Retrieved from <https://in.mathworks.com/help/aerotbx/ug/igrfmagn.html>
- [8] P. D. Groves, *Principles of GNSS, Inertial, and Multisensor Integrated Navigation Systems*, 2nd ed. Norwood, MA: Artech House, 2013, pp. 218-221
- [9] Demoz, Gebre Egziahber. "Thesis." Scribd, 2019. Available at: <https://ar.scribd.com/document/74337987/DemozGebreEgziahberThesis01>
- [10] "Avionics and Navigation Systems." DocPlayer, 2018. Available at: <https://docplayer.net/50060679-Avionics-navigation-systems.html>

- [11] "World Magnetic Model (WMM)." AHRs Docs, 2024. Available at: <https://ahrs.readthedocs.io/en/latest/wmm.html>
- [12] Brewer, Megan R. "CubeSat Attitude Determination and Helmholtz Cage Design." AFIT Scholar, 2012.
- [13] "IGRF Magnetic Model." MathWorks, 2022. Available at: https://la.mathworks.com/help/aerotbx/ug/igrfmagm.html?s_tid=gn_loc_drop
- [14] "Temperature Controlling Device." Docshare, 2019. Available at: <http://docshare04.docshare.tips>
- [15] "How to Add H-Bridge to Driver." Small Business FASR586, 2020. Available at: <https://smallbusinessfasr586.weebly.com/how-to-add-h-bridge-to-driver.html>
- [16] "Principles of GNSS, Inertial, and Multi-Sensor Integrated Navigation Systems." Ebin Pub, 2022. Available at: <https://ebin.pub/principles-of-gnss-inertial-and-multi-sensor-integrated-navigation-systems-2nd-ed-978-1-60807-005-3.html>
- [17] "XL-4016 DC-DC Buck Converter." DNA Tech India, 2024. Available at: <https://www.dnatechindia.com/xl-4016-dc-dc-buck-convertoor-cc-cv-step-down-module.html>
- [18] "Mathematical Analysis for Space Navigation." Scribd, 2020. Available at: https://web.archive.org/web/20180828114536if_/https://wizchan.org/hob/src/1451183375364-1.pdf
- [19] Laughlin, Kail P. "Single-Vector Aiding of an IMU for CubeSat Attitude Determination." University of Minnesota, 2020.
- [20] "Development of CubeSat Antenna Systems for Ionospheric Sounding." Kirkby, Graham, 2019.
- [21] "Helmholtz Cage Design for Nanosatellites HWIL Testing." IEEE Transactions on Aerospace and Electronic Systems, 2019. Available at: <https://ieeexplore.ieee.org/document/8711590>
- [22] Chism, C.T. "Development and Characterization of a Miniature Vectorized Rubidium Magnetometer for Spaceborne Measurements of Earth's Magnetic Field." University of Colorado at Boulder, 2024.

- [23] Panyalert, Thanayuth, et al. "Characterization and Verification of the Optimal Feedback Gain of a Satellite Magnetorquer-based Attitude Control System." *Advances in Space Research*, 2024.
- [24] Tasnim, Nazia. "Machine Learning in the Classification of Computer Code." University of Lethbridge, 2020.
- [25] "Magnetometer Calibration with Small Space Coverage." Wahdan, Ahmed, Proquest, 2014.
- [26] "Small Satellite Passive Magnetic Attitude Control." Gerhardt, David T., Proquest, 2014.
- [27] "Optimizing Additive Manufacturing Parameters for Graphene-Reinforced PETG Impeller Production." Raja S, et al., *Results in Engineering*, 2024.
- [28] "Methodology for CubeSat Debris Collision Avoidance Based on Its Active ADCS System." González-Rodríguez, Desiree, et al., *Applied Sciences*, 2023.
- [29] "Characterization and Verification of the Optimal Feedback Gain of a Satellite Magnetorquer-based Attitude Control System." Panyalert, Thanayuth, et al., *Advances in Space Research*, 2024.
- [30] "Single-Vector Aiding of an IMU for CubeSat Attitude Determination." Laughlin, Kail P., University of Minnesota, 2020.
- [31] "Automatic Magnetometer Calibration with Small Space Coverage." Wahdan, Ahmed, Proquest, 2014.
- [32] "Small Satellite Passive Magnetic Attitude Control." Gerhardt, David T., Proquest, 2014.
- [33] "Development and Characterization of a Miniature Vectorized Rubidium Magnetometer for Spaceborne Measurements of Earth's Magnetic Field." Chism, C.T., University of Colorado at Boulder, 2024.
- [34] K. Huang, "Design and Implementation of a Hardware-In-The-Loop ADCS Simulator for CubeSats," 2020. [Online].
Available: <https://kevinhuang.dev/assets/pdf/ADCS.pdf>

- [35] A. Inumoh, M. Horri, and H. Yahya, "Development of a 3-axis Satellite Attitude Control System Testbed," Coventry University, UK. [Online]. Available: <https://pure.coventry.ac.uk/ws/portalfiles/portal/10717228/Horri.pdf>
- [36] "Air bearing," Wikipedia. [Online]. Available: https://en.wikipedia.org/wiki/Air_bearing
- [37] D. A. Vallado, *Fundamentals of Astrodynamics and Applications*, 4th ed. Hawthorne, CA: Microcosm Press, 2013.
- [38] D. Schaub and J. L. Junkins, *Analytical Mechanics of Space Systems*, 4th ed. AIAA Education Series, 2020.
- [39] J. D. Crassidis and J. L. Junkins, *Optimal Estimation of Dynamic Systems*, 2nd ed. CRC Press, 2011.
- [40] R. J. Sedwick and D. W. Miller, "Development of a Planar Air Bearing Microgravity Testbed," *AIAA Guidance, Navigation, and Control Conference*, 1998.
- [41] J. R. Wertz, *Spacecraft Attitude Determination and Control*, Springer, 1978.
- [42] L. Davis, M. McKinley, and P. Ostrander, "Development of a Low-Cost Air-Bearing Testbed for Spacecraft ADCS Verification," in *Proceedings of the IEEE Aerospace Conference*, Big Sky, MT, 2014.
- [43] T. Do, A. Yousefian, and M. Moghaddam, "Design and Implementation of a Low-Cost Hardware-in-the-Loop Simulator for Small Satellite ADCS," *Acta Astronautica*, vol. 185, pp. 309–318, 2021.
- [44] J. P. Mueller et al., "The QuakeSat Mission: A CubeSat to Monitor ELF/VLF Emissions," Proc. 17th AIAA/USU Conference on Small Satellites, 2003.
- [45] G. Aglietti et al., "The RemoveDEBRIS Satellite Mission: First Results," *Acta Astronautica*, vol. 168, pp. 293–302, 2020.
- [46] J. D. Cutler et al., "The CADRE CubeSat: Autonomous 3D Mobility in Planetary Terrain," AIAA Space 2016 Conference and Exposition, 2016.

- [47] J. Kim et al., “SPHERES: A Testbed for Long Duration Satellite Formation Flying in Microgravity Conditions,” AIAA Guidance, Navigation and Control Conference, 2003.
- [48] H. Funase et al., “Hodoyoshi-3 Project: Advanced Remote Sensing with Microsatellite Bus Demonstrator,” Proc. 31st ISTS, 2017.
- [49] M. E. Drews et al., “RECONSat: A CubeSat Platform for RF Communications and Control Experiments,” IEEE Aerospace Conference, 2017.
- [50] SwissCube Team, “SwissCube - A Swiss Pico-Satellite for Space Research and Education,” *Acta Astronautica*, vol. 67, pp. 1188–1196, 2010.
- [51] J. Puig-Suari, C. Turner, and W. Ahlgren, “Development of the Standard CubeSat Deployer and a CubeSat Class PicoSatellite,” IEEE Aerospace Conference Proceedings, 2001.
- [52] A. Upadhyaya et al., “STUDSAT - A Student Nano-Satellite for Imaging Applications,” Proc. 61st International Astronautical Congress, 2010.
- [53] C. Nokes et al., “Environmental Testing of the NEMO-HD Microsatellite,” Small Satellite Conference, 2019.
- [54] A. Kestilä et al., “Aalto-1: A CubeSat Mission to Demonstrate Finnish Space Technology,” *Geoscientific Instrumentation, Methods and Data Systems*, vol. 2, pp. 121–130, 2013.
- [55] C. E. Chamberlin et al., “The Miniature X-ray Solar Spectrometer (MinXSS) CubeSat Mission,” *Journal of Spacecraft and Rockets*, vol. 55, pp. 993–1007, 2018.
- [56] J. Obermark et al., “FissionSat: Autonomous CubeSat Swarms with Machine Learning for Deep Space Navigation,” International Astronautical Congress, 2022.
- [57] D. G. Somerville et al., “ICLSat: A Low-Cost Modular CubeSat Platform for Education and Research,” *Acta Astronautica*, vol. 178, pp. 618–627, 2021.

[58] C. H. Tong, L. Lin, and C. Guan, “Low-Cost ADCS for CubeSat Missions,” *IEEE Transactions on Aerospace and Electronic Systems*, vol. 55, pp. 1234–1245, 2019.

[59] LibreCube Initiative, “LibreCube: Open Source CubeSat Systems,” Available: <https://librecube.net>, [Accessed: May 2025].

[60] NASA CubeSat Launch Initiative (CSLI), “Overview,” Available: https://www.nasa.gov/directorates/heo/home/CubeSats_initiative.html, [Accessed: May 2025].

[61] P. K. Pal et al., “Swayam: India's First Student-Built Communication CubeSat,” *Current Science*, vol. 113, pp. 483–490, 2017.